UNIVERSITÀ DEGLI STUDI DI TRIESTE

SEDE AMMINISTRATIVA: UNIVERSITÀ DEGLI STUDI DI TRIESTE

XVII CICLO DEL DOTTORATO DI RICERCA IN
FISICA

Open charm in proton-lead collisions with ALICE

Dottorando:
Raffaele Grosso 174 CS

Coordinatore del Collegio dei Docenti:
Chiar.mo Prof. Gaetano Senatore

Tutore:
Chiar.mo Prof. Rinaldo Rui

Gennaio 2005

Contents

Introduction

Heavy Ion Physics has been strongly boosted starting at the end of the Nineties with the analysis performed by different experiments at the Super Proton Synchrotron (SPS) at CERN, and continuing with the most recent observations at the Relativistic Heavy Ion Collider (RHIC) at Brookhaven, thanks to experimental evidences which find a coherent explanation only as effects of the formation of a new state of matter, called Quark Gluon Plasma (QGP) and characterized by the activation of the partonic degrees of freedom, ordinarily hidden by the confinement of partons inside the hadrons they build up.

A new collider is now under construction in the CERN area: the Large Hadron Collider (LHC). It will study a numerous set of collision systems and give access to energy densities much higher than those recently obtained by RHIC, several hundreds of times the nuclear density of ordinary nuclear matter. From this exploration into new areas of the phase diagram of nuclear matter, at unprecedented temperatures and densities, one expects to deepen the present knowledge on the dynamics internal to nucleons, on how they are modified by what is outside the nucleons, on the extent up to which some assumptions as the factorization of the interactions between partons in short-scale and long-scale terms can be valid. This knowledge will be the base to fulfill a big expectation for the start of the activity at the LHC: the possibility to confirm and study the characteristics of the QGP.

The possible probes of the QGP are quite indirect, up to now, and result from the comparison of many observables; among them heavy quarks (charm and beauty) play a primary role. It's their heavy mass which makes them particular suitable probes of the early stage of the system formed after the collisions, through the study of their production cross sections and their kinematical distributions (e.g. their momentum in the plane transverse to the beam axis). At LHC energies heavy quarks will reach production cross sections which will allow to use them as effective tools for the study of the medium they traverse. Furthermore observables already available will considerably extend their range of applicability.

The observations in the lead-lead collision system, the one where the creation of the QGP is expected, need to be flanked by proton-proton and proton-nucleus runs in order to be correctly understood; this collision systems will also allow for dedicated physics studies.

The present thesis work is part of the heavy quark physics program at ALICE, the experiment at the LHC dedicated to heavy ion collisions, being aimed at estimating the sensitivity and precision of the ALICE detector and software for reconstructing charm kinematical distributions and at applying these estimate for evaluating ALICE's capability to detect multipartonic events. Namely the present study is based on a feasibility study of the exclusive reconstruction of the hadronic decay $D^0 \to \kappa^-\pi^+$ of the charm meson D^0 in the proton-lead collision system at ALICE.

Chapters 1 and 2 introduce the theoretical background of this study: actual observations considered as QGP evidences are presented in Chapter 1 along with a brief introduction to the novelty aspects related to the LHC collider. Among them charm physics aspects, relevant for this study, are presented in some more detail in Chapter 2.

The experimental background, namely the ALICE detector and the simulation and reconstruction environment AliRoot, is presented in Chapter 3.

The activities performed for this thesis are the following:

- the installation of a farm of PCs dedicated to the activity of simulation, reconstruction and analysis presented in Chapter 5; test of software and hardware choices for the optimization of the farm performances an the support of the AliRoot software. This issues are presented in Chapter 4.

- the exclusive reconstruction of the $D^0 \to \kappa^-\pi^+$ hadronic decay in proton-lead collisions through kinematical cuts and their optimization w.r.t. an appropriate binning in transverse momentum. Chapter 5 presents the choices and the results pertaining the simulation of events, primary vertex and track reconstruction and the strategy for the selection of the signal D^0s out of the combinatorial background. The results obtained are presented in terms of statistical error and compared with an estimate of the systematic error.

- the application of the aforementioned results to derive a first estimate of the capability of ALICE of detecting double parton events by means of the D^0 hadronic decay channel.

Introduzione

La fisica degli ioni pesanti ha ricevuto un forte impulso a partire dalla fine degli anni Novanta, con le prime analisi degli esperimenti al Super Proton Synchroton (SPS) al CERN, fino alle più recenti osservazioni al Relativistic Heavy Ion Collider (RHIC) a Brookhaven, con l'acquisizione di evidenze sperimentali che possono essere coerentemente interpretate solo come prove dell'esistenza di una nuova fase della materia nucleare, chiamata plasma di quark e gluoni (QGP), caratterizzata dall'attivazione dei gradi di libertà partonici normalmente nascosti a causa del confinamento dei partoni all'interno dei nucleoni che essi costituiscono.

Fra un paio d'anni è prevista l'accensione del fascio al collisionatore *Large Hadron Collider'* (LHC), attualmente in costruzione nel comprensorio del CERN, che permetterà di studiare un'ampia gamma di sistemi di collisione a densità d'energia molto superiori rispetto a quelle finora esplorate e recentemente ottenute al RHIC, dell'ordine di centinaia di volte rispetto alla densità nucleare in condizioni ordinarie. Da queste proiezioni in intervalli di temperatura e densità di materia nucleare ancora inesplorati ci si aspetta di allargare le nostre conoscenze sulle dinamiche interne ai nucleoni, su come esse siano modificate all'interno del nucleo, su quali siano i limiti di validità di alcuni assunti teorici quali la possibilità di fattorizzare le probabilità di interazione fra i costituenti primi della materia nucleare (i partoni) in termini di interazioni a piccole e grandi distanze (parte perturbativa e non-perturbativa). Gli attesi chiarimenti riguardanti queste questioni aperte sono la base per la realizzazione di una grande aspettativa legata all'entrata in funzione del collisionatore LHC: la possibilità di fornire informazioni e conferme sulle caratteristiche del plasma di quark e gluoni, caratterizzata dai gradi di libertà partonici.

I modi per vedere il plasma di quark e gluoni sono, ad ora, molto indiretti e seguono dal confronto di molte osservabili; fra di esse di importanza primaria sono i quark pesanti (charm e beauty), di cui si studia in particolare la frequenza con cui vengono prodotti (attraverso le sezioni d'urto) e le distribuzioni cinematiche (ad esempio del loro momento nel piano perpendicolare

al fascio di collisione). È proprio la grande massa dei quark pesanti a renderli delle sonde particolarmente interessanti per studiare le caratteristiche del mezzo deconfinato che viene a formarsi a seguito di collisioni ione-ione; e le grandi energie che LHC raggiungerà in tali collisioni permetteranno di ottenere elevate produzioni di quark pesanti rendendo possibile il loro utilizzo per nuovi studi sulle proprietà del mezzo; inoltre osservabili già ora disponibili estenderanno i loro intervalli di applicabilità.

Le osservazioni sperimentali nel sistema di collisione piombo-poimbo, quello in cui ci si aspetta la creazione del plasma di quark e gluoni, hanno bisogno di essere affiancate da un programma di collisioni protone-protone e protone-piombo per poter essere comprese correttamente; questi sistemi di collisione permetteranno inoltre studi di fisica dedicati.

Il lavoro svolto nella presente tesi rientra nello studio della fisica del charm ad ALICE, l'esperimento di LHC dedicato alle collisioni di ioni pesanti, ed è finalizzato a stimare la precisione e l'efficienza con cui ALICE sarà in grado di rivelare il charm e le sue caratteristiche cinematiche e ad utilizzare tale stima per una valutazione della capacità di ALICE di rivelare eventi multipartonici. Esso è infatti incentrato sullo studio di fattibilità della ricostruzione del decadimento adronico $D^0 \to \kappa^- \pi^+$ del mesone con charm D^0 nel sistema di collisione protone-piombo all'interno del rivelatore ALICE.

I capitoli 1 e 2 introducono il contesto teorico di questo lavoro: le attuali osservazioni interpretate come evidenze sperimentali della formazione del plasma di quark e gluoni sono presentate nel primo capitolo assieme ai principali aspetti di novità legati al collisionatore LHC. Fra questi la fisica del charm sarà di particolare rilievo ad ALICE; essa è approfondita nel secondo capitolo.

Il contesto sperimentale, vale a dire il rivelatore ALICE e il suo ambiente di simulazione e ricostruzione `AliRoot`, è presentato nel capitolo 3.

Le attività svolte specificamente per questa tesi sono:

- l'installazione di una farm dedicata utilizzata per le simulazioni e gli studi presentati nel capitolo 5 e per il test di soluzioni software e hardware per l'ottimizzazione del supporto del framework di simulazione AliRoot. Questi test sono presentati nel capitolo 4.

- la ricostruzione esclusiva del decadimento adronico $D^0 \to \kappa^- \pi^+$ in collisioni protone-piombo per mezzo di opportuni tagli cinematici e della loro ottimizzazione in funzione degli intervalli di momento trasverso. Il capitolo 5 presenta le scelte legate alla simulazione degli eventi, le efficienze e risoluzioni di ricostruzione delle tracce e del vertice primario, la strategia seguita per la ricostruzione delle D^0; infine i risultati ottenuti

sono presentati in termini di errore statistico relativo e confrontati con una stima degli errori sistematici.

- applicazione dei risultati ottenuti per valutare la capacità di ALICE di rivelare eventi partonici doppi per mezzo del decadimento adronico della D^0.

Chapter 1

Heavy ion physics at the LHC

Ultra-relativistic heavy ion physics investigates the behaviour of matter at the presently shortest accessible time and space scales and at extreme conditions: densities and temperatures much higher than those of ordinary nuclear matter. The newly accessible energy ranges available at the colliding beam facilities are of particular interest because of the strong belief that these collision energies will be high enough to overcome the repulsive forces between nucleons, thus allowing to demonstrate and probe the existence of a different phase of nuclear matter. In this phase (the so called *quark gluon plasma* (QGP) or deconfined matter) the hadrons' constituents, the partons, are no longer confined inside hadrons, but form a plasma of quarks and gluons. The aim of heavy ion experiments is then to find the critical conditions beyond which nuclear matter experiences this phase transition and to study the properties of the newly formed nuclear phase, trying to understand how macroscopic properties and collective behaviour arise from microscopic laws of elementary particle physics.

Furthermore HI experiments are expected to be crucial for their fringe implications on astrophysical (1) and cosmological (2) issues; in fact:

1. a deconfined phase may also occur naturally in supernovae, gamma-ray bursts and neutron stars and some parameters which can be extracted from HI data can be compared to values inferred from astrophysical observations [1] (e.g. compressibility of nuclear matter compared to extrapolation from neutron star masses);

2. the bulk of deconfined matter at extreme conditions produced after collisions in present HI experiments, although limited in space and short-living, should reproduce the state of matter as it was during the first microseconds after the Big Bang in its evolution toward nuclear

matter in normal conditions, from which models of the early universe and of its evolution are strongly dependent.

The transition to a deconfined phase will occur when the energy density of matter is of the order of that of matter inside a proton (i.e. $\sim$1 GeV/fm^3). Nuclear matter can be brought to energy densities exceeding the critical value by either increasing the baryonic density or the temperature of the system; this is achieved by colliding heavy ions, such as gold or lead, at ultra-relativistic velocities. The collision energy and the atomic number of the colliding nuclei allow to control the density and temperature of the resulting strongly interacting medium.

Since there is no fundamental theory of QGP, heavy ion experiments are expected to prove its formation from a collection of observables. A rich experimental program has been carried out in the last two decades both by heavy ion fixed target experiments, at the AGS (Brookhaven) and SPS (CERN), and by colliding-beam experiments at SPS and RHIC (Brookhaven). The Large Hadron Collider (LHC) is the next-generation heavy ion collider under construction at CERN and will attain a center of mass energy per nucleon pair almost thirty times larger than the corresponding energy at RHIC; in this section it will be briefly explained why this should allow to get a much clearer picture of the deconfined QCD matter summarizing the state of the art from SPS and RHIC experiments and describing the novelty of the LHC physics.

1.1 QGP phenomenology

The finite size of hadrons (of the order of 1 fm) led to suggest the existence of a critical temperature and density for nuclear matter. If somehow we can press hadrons together at reciprocal distances below their size or if we are able to get a hadronic system with very high temperature, hadrons will start to superimpose and lose their identity.

The first suggestion of a critical temperature [2] came also from the qualitative analysis of the spectrum of hadronic states, characterized by a level density:

$$w(E) \propto \exp \beta_C E$$

i.e. an exponentially growing number of resonances; the temperature $T_C = 1/K\beta_C$ was proposed as a limiting temperature. Later it was suggested that this could be a critical temperature for a phase transition [3]; this belief developed from the picture of hadrons as bags subject to internal and external pressure (MIT bag model [4]) and from the expectation of a phase transition

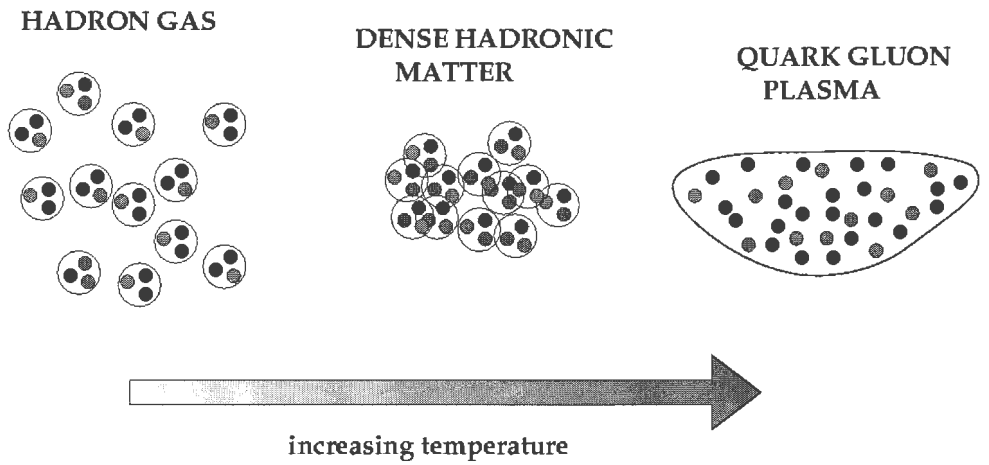

which restored the chiral symmetry, broken in ordinary nuclear matter. Lattice QCD has finally not only predicted a phase transition but also computed the value of the transition temperature in the limit of infinite spatial volume, vanishing lattice spacing and vanishing baryon content: the resulting values lie around 175 MeV, which corresponds to an energy density of the order of 1 GeV/fm^3, one order of magnitude greater then that of ordinary nuclear matter.

1.1.1 The QCD phase diagram

The possible known states of QCD matter are usually represented in a phase diagram with the temperature[1] T on the y-axis and the baryon chemical potential[2] μ_B on the x-axis.

Phase transitions are in general associated to long-distance effects; in the case of a system described by QCD, this means to increase the strength of the interaction and thus to go outside the range where perturbative QCD is applicable. This non-perturbative QCD regime can only be studied by means of some phenomenological model or by lattice QCD, which is still the only theory which allows to study high temperature QCD from first principles without any intermediate effective theory. One important limit of lattice

[1] In nuclear physics the MeV is used as a convenient energy unit because it is roughly the energy scale of nuclear processes. An average energy of 1 MeV corresponds to a temperature of $1.2 \times 10^{10} K$. As in classical thermodynamics, the temperature is a measure of the average velocity (thus kinetic energy) carried by each degree of freedom.

[2] The baryochemical potential μ_B is the variation of energy due to an increase in the net number of baryons N_B (baryons - antibaryons): $\mu_B = \frac{\partial E}{\partial N_B}$. Increasing with the baryon density ρ_B, it is an alternative way of expressing the baryon content of a system.

QCD at present is that it assumes a null baryon content ($\mu_B = 0$); thus, at $\mu_B \neq 0$, we have to rely on interpolations between low-energy effective theories modeling low-density hadronic matter and perturbative QCD describing high-density QGP. Recent numerical lattice QCD calculations ([5] and [6]) have overcome the limit of null baryon density extending the simulations at finite baryon density up to 0.5-0.8 GeV, suggesting that the hadron gas phase and the QGP phase are separated by a rapid crossover at low μ_B, while above the tri-critical point (at $\mu_B \approx 700$ MeV, $T \approx 160$ MeV) the two phases are separated by a first-order phase transition.

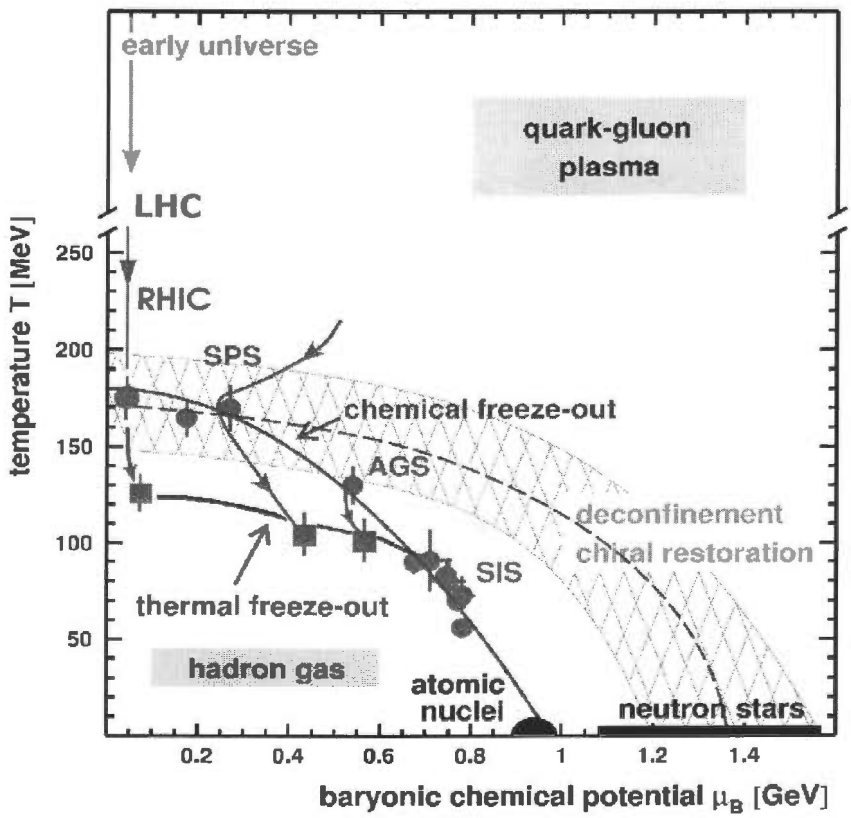

Figure 1.1: *QCD phase diagram. The dashed line represents the separation between hadron gas and QGP phases with a conservative uncertainty (cross-hatched region). Arrowed red lines represent the trajectories of thermalized matter at different collision energies (rearranged from [7]).*

The phase diagram for strongly interacting matter (fig. 1.1) [3] is based on fundamental thermodynamic ideas and lattice QCD results displaying the

[3] When looking at QCD phase diagrams or at the evolution of some bulk thermody-

existence of different phases as a function of the temperature of the system T and of the chemical potential μ_B, a variable which measures the baryon density. The existence and the values of the critical temperature T_c and of the critical density have been at first based on a simple phenomenological model of non-perturbative QCD, the "bag model" [4] ([4]), and later confirmed and made more precise by lattice QCD calculations.

Ordinary (liquid) nuclear matter is present at low temperatures and its baryon densities is $\rho_0 \simeq 0.17$ fm^{-3}, or equivalently its baryochemical potential is $\mu_B \simeq 940$ MeV, the proton mass. Increasing the energy density, by heating the system (vertical direction) or by compressing it (horizontal direction), leads to a gaseous phase of hadronic light resonances. Further increasing the energy density will allow to access the QGP region where hadrons dissolve into a soup of their constituents, the partons. The interaction between partons is known from QCD to vanish logarithmically with increasing temperature; it is then expected that the bulk thermodynamic variables of the deconfined phase asymptotically reproduce those of an ideal quark-gluon gas.

The system produced after an ultra-relativistic[5] collision in a hadron collider is a high-temperature, low-baryon density system and should resemble the path followed by primordial Universe matter starting from a few microseconds after the Big Bang; in contrast, partons are believed to form a

namical variable, it is important to remember that we can only establish the hot and dense conditions needed for nuclear phase transitions during heavy ion collisions, but it is experimentally impossible to prepare the system at a given pressure, temperature and density and we do not have any direct way of measuring the state variables (temperature, pressure, density) which instead are determined from observables such as the abundance of isotopes, the population of excited nuclear states, the shapes of the energy spectra from nuclear collision remnants, the production of particles such as pions. Therefore those diagrams cannot be filled at present whit experimental points; they are the result of lattice QCD computations which need to be extrapolated at finite baryon densities.

[4]In this model a hadron is just a bag containing the quarks floating in an "empty vacuum" while outside the bag there is a "true vacuum", the non-perturbative vacuum filled by $q\bar{q}$ pairs, which generates a pressure B on the bag directed inward. B, referred to as *bag pressure*, is a phenomenological quantity accounting for non-perturbative effects. The phase transition occurs when the internal pressure reaches and exceeds the external pressure (given by the pressure of a pion gas), plus the bag pressure B.

[5]HI physics energy domains are usually divided in:

- intermediate energy HI reactions (10÷100 MeV per nucleon, or AMeV; nuclear matter around its normal density ρ_0 and in the multi-fragmentation region);
- relativistic energy HI reactions (100 AMeV ÷ 10 AGeV);
- ultra-relativistic HI reactions (above 10 AGeV).

high-density QGP phase in the formation of neutron stars where hadrons are packed together at very high densities by the gravitational collapse while temperature remains close to zero.

The energy density (as pressure and entropy) is roughly proportional to the number of degrees of freedom; The evolution of the *normalized energy density* ϵ/T^4 w.r.t. temperature T as evaluated by lattice QCD is shown in figure 1.2 in the case of two, three and "two plus one" activated quark flavours. The meaning of the two solid curves and the bridging dots is the following: the energy density, as the other bulk thermodynamic variables, depends on

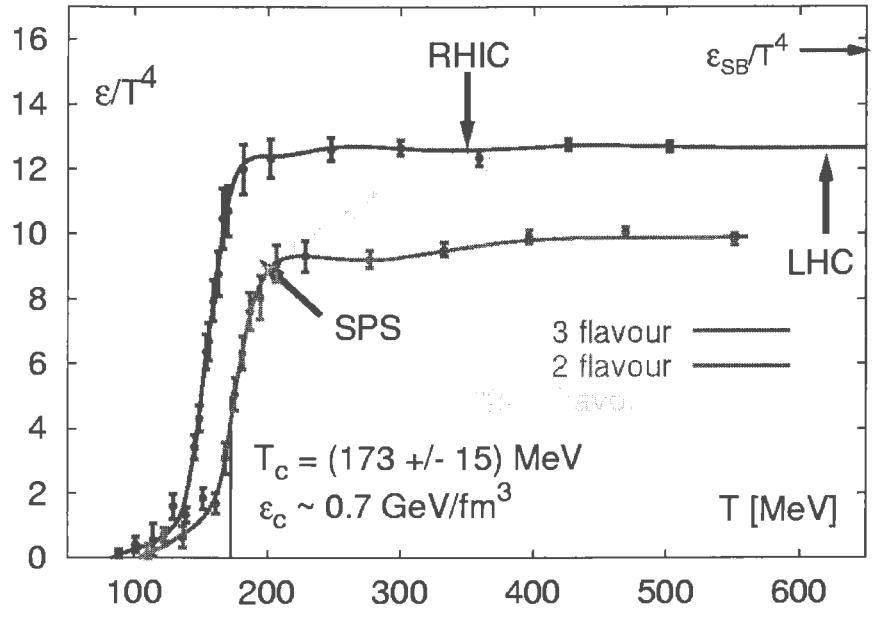

Figure 1.2: *Energy density in the case of 2, 3 and 2+1 flavours.*

the number of degrees of freedom n_{DOF} and thus on the number of hadrons and of quark flavours which enter in the thermodynamics of the system. At low temperatures the degrees of freedom come from hadrons; since they are weighted by the Boltzmann factor $\exp[\frac{-m_h}{T}]$, the only hadrons entering the thermodynamics are pions ($m_\pi \simeq 140$ MeV) while the contribution from all other hadrons (all heavier than 500 MeV) is negligible. Thus at low temperatures the degrees of freedom are three, those of the pion isospin triplet (π^+, π^0, π^-). At high temperatures, instead, since the formation of a free quark-gluon gas is expected, the relevant degrees of freedom are those

from colour and quark dynamics [6]. This is summarized by equation 1.1:

$$\frac{\epsilon}{T^4} = n_{DOF}\frac{\pi^2}{30} = \begin{cases} (n_f^2 - 1)\frac{\pi^2}{30} & T \to 0 \\ (16 + \frac{21}{2}n_f)\frac{\pi^2}{30} & T \to \infty \end{cases} \tag{1.1}$$

The predicted value for the transition temperature obtained for $\mu_b = 0$ is $T_c = 173 \pm 15$ MeV; this value decreases with increasing baryon density.

Looking at the two solid curves we see also that the asymptotic behaviour depends on the number of flavours involved; the strange quark s, the next lighter quark after u and d with its mass of the order of the transition temperature ($m_s \simeq$ 100-150 MeV), is believed to gradually enter the thermodynamics of the system and thus the curve for 2+1 quark flavours is likely to better describe the evolution of the energy density. It is important to note that the energy density approaches its asymptotic value (and the system is in a perturbative regime) only for temperatures around twice the critical temperature T_c.

1.1.2 Bjorken's picture of the collision

The space-time evolution of the system expected during and after the collision of two heavy ions colliding at ultra-relativistic velocities is a complex event in which the available energy allows to turn on degrees of freedom hidden in normal nuclear matter, which then turn off while the system expands and cools down. This evolution is usually described qualitatively by means of the Bjorken scenario ([8],[9]) relating the longitudinal size of the system z with the laboratory time t as in fig. 1.3.

At $t < 0$ the two nuclei, let's call them projectile and target, approach with a velocity close to c along the two diagonal lines in the graph; at $t = 0$ the two nuclei collide. At 1 energies nuclei are strongly Lorentz contracted, thus the longitudinal coordinate of the component nucleons is approximately the same. Each nucleon of the two colliding nuclei undergoes many nucleon-nucleon collisions with the opposite arriving nucleons losing approximately one unit of rapidity at each collision. The heavier the nuclei, the higher the average number of collisions per nucleon; if the target (projectile) nucleus is thick enough, projectile (target) nucleons are likely to be stopped almost to zero rapidity, making almost all of their initial energy available in a small

[6] If a rapid rise of entropy was predicted before QCD, the saturation of the number of degrees of freedom at n_{QCD} is a unique prediction of QCD. For the gluons $n^g_{DOF} = n_g \cdot n_p = 8 \cdot 2$, where n_g is the number of gluons and n_p the number of polarizations; for the quarks $n^q_{DOF} = 7/8 \cdot 2 \cdot n_f \cdot n_c \cdot n_s = \frac{21}{2}n_f$, where n_f is the number of flavours, n_c is the number of colours and n_s is the number of spins; the factor 7/8 normalizes Bose-Einstein statistics, the factor 2 counts quark and antiquark states.

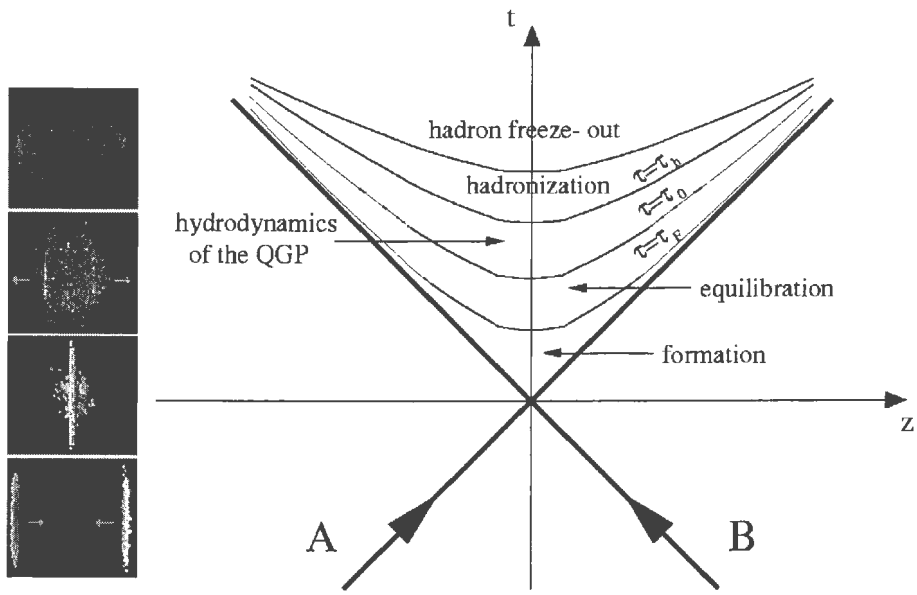

Figure 1.3: *Left: a picture of the heavy ion collision in four stages: i)the two colliding nuclei, relativistically contracted, approach each other ii)first instants of collision: hard interactions iii)new produced particles interact at hard and soft scales iv)final state particles freeze out while moving outwards. Right: The Bjorken picture for the space-time evolution of the collision.*

region around the interaction point. In the *formation stage* this energy produces a system of particles, mainly quarks and gluons at collider energies, probably not straight in thermal equilibrium (pre-equilibrium phase) into a volume of some tens of fm^3, according to Bjorken's picture. During the *equilibration stage* interactions among partons will drive the system to a thermalized QGP phase if the initial conditions allow the system to thermalize before the energy density drops below its critical value. The time τ_0 at which thermalization has completed and a plasma is produced is an unknown quantity, estimated by Bjorken to be of order 1 fm/c.

The rescattering of partons from different nucleon-nucleon collisions can lead to a state of local thermal equilibrium, by redistributing the energy lost by the beams into the statistically most probable configuration; this rescattering processes generate a thermodynamic pressure acting against the outside vacuum which causes the reaction zone to expand collectively; the hydrodynamic expansion of the thermalized QGP system is associated to

a decrease in temperature while simultaneously the surface of the system, where the temperature has already gone below T_c, evaporates into a hadron gas (*hadronization stage*). After $\tau \simeq 20$ fm/c evaporation is expected to be completed and the resulting hadron gas, now occupying some $10^4 - 10^5$ fm^3 around the interaction point, should have reached its final chemical composition (*freeze-out stage*) continuing its cooling and expansion toward the detectors.

The energy and baryon density at the formation stage (usually referred to as *initial conditions*) are not directly observable but can be reconstructed from the resulting particle distributions, as firstly shown by Bjorken in [8]. For example the initial energy density ϵ_0 is the ratio between the amount of energy released in the relevant volume $\mathcal{V}$ of the collision region and the volume itself, which can be estimated as the product between the overlapping area $\mathcal{A}$ in the collision of the two nuclei and the maximum longitudinal distance traveled by the newly produced particles Δz; the energy released into this volume can be related to the hadron multiplicity at central rapidity[7] $\left(\frac{dN_h}{dy}\right)_{y=0}$ thanks to the equations A.1 relating the rapidity with the energy and the longitudinal distance z. This estimate uses also the fact that, after one has fixed the proper time $\tau = \tau_0$, small rapidities are associated to particles close to the origin z=0[8]. Bjorken' s estimate for the initial energy density ϵ_0 is finally:

$$\epsilon = \left(\frac{dN_h}{dy}\right)_{y=0} \times \frac{m_T}{\mathcal{A}\tau_0} \tag{1.2}$$

where m_T is the transverse mass [8] and expresses the average energy particles carry in the transverse plane (the plane perpendicular to the beam axis).

1.2 Present QGP signatures

HI collider facilities as RHIC or LHC take the challenge of probing the existence and the properties of a small shortly lived QGP system which is impossible to be observed directly. Its properties instead require to be traced back from many different observables, not derivable from a unique QGP theory, many of which related to or strongly affected by the final state[9]. Among

[7] The meaning of this variable is given in appendix A

[8] See appendix A; for a complete derivation of this estimate see for example [10]

[9] As to which are the observables necessary and sufficient to identify the formation of a QGP state there is quite an ongoing debate. Recently a combination of three kind of observables has been proposed as unambiguously probing the formation of a deconfined medium ([11])

these observables, those describing the system as a whole, as its geometry and spatial evolution or initial conditions, are classified as *global observables*; those expected to show appreciable differences whether a QGP has formed or not are usually called *QGP signatures*. Signatures of a deconfined medium are briefly discussed in the following in the context of the SPS and RHIC activity.

1.2.1 QGP signatures at SPS

CERN-SPS programme started in 1986 with fixed target experiments firing heavy ion targets (Au and Pb) with light ion beams (O, S and Si). In 1994 the SPS experiments turned to head-on collisions at an energy per nucleon pair $\sqrt{s_{NN}} = 17$ GeV. While lattice QCD calculations predict a value for the energy density at phase transition $\epsilon_c \sim 1$ GeV, the SPS reached values around 3.5 GeV in Pb-Pb central collisions. Two effects, predicted to appear in a deconfined medium in the eighties, were observed in Pb-Pb collisions at the SPS, and were claimed as QGP experimental signatures:

1. strangeness enhancement: increased production of strange and multi-strange baryons (w.r.t. values extrapolated from p-p data);

2. charmonium suppression: decrease in the production of the lowest $c\bar{c}$ state, the J/Ψ meson (w.r.t. values extrapolated from p-p data).

We are briefly describing them in the following of this section.

Strangeness enhancement: The enhancement of strangeness was predicted to be a QGP signature for the first time by J. Rafelski and B. Müller in 1982 ([12]). There are two effects that can favour strangeness production in a QGP system:

- *Partial restoration of the chiral symmetry*: in a deconfined medium quarks loose their *constituent mass*, due to confining effects of strong interaction, and retain only their *bare mass*; this leads to a decrease of the mass of the strange quark from ~500 MeV to ~150 MeV and will lower the threshold for $s\bar{s}$ pairs production from twice the constituent- to twice the bare-mass of the s quark, thus allowing $s\bar{s}$ quark pairs to be copiously produced via gluon-gluon fusion.

- *Pauli blocking of light quark production*: if the system is a baryon-rich system (i.e. there are much more quarks then antiquarks), as is the case for SPS, the high concentration of up and down quarks (which are

fermions) might cause the lowest free level for a light quark to have an energy comparable to that of $s\bar{s}$ production and thus the creation of $u\bar{u}$ and $d\bar{d}$ pairs might be blocked due to the Pauli principle in favour of the creation of $s\bar{s}$ pairs, in spite of their larger mass.

A strangeness enhancement is expected also in a strongly interacting hadronic medium, when no deconfinement has occurred, due to hadronic interactions such as $\pi + \pi \rightarrow K + \bar{K}$ or $\pi + N \rightarrow \Lambda + K$, where the abundance of strange quarks gradually grows in a chain of rescattering processes; but in this case multi-strange baryons (*hyperons*) are not likely to be produced, while in the case of QGP formation we expect the enhancement to increase with the strangeness content (i.e. to get increasingly enhanced yields for the following hyperons: $\Lambda(uds), \Sigma^-(dss)$ and $\Omega^-(sss)$). This effect has been observed by the NA49 and NA57 experiments at SPS (see left panel in figure 1.4).

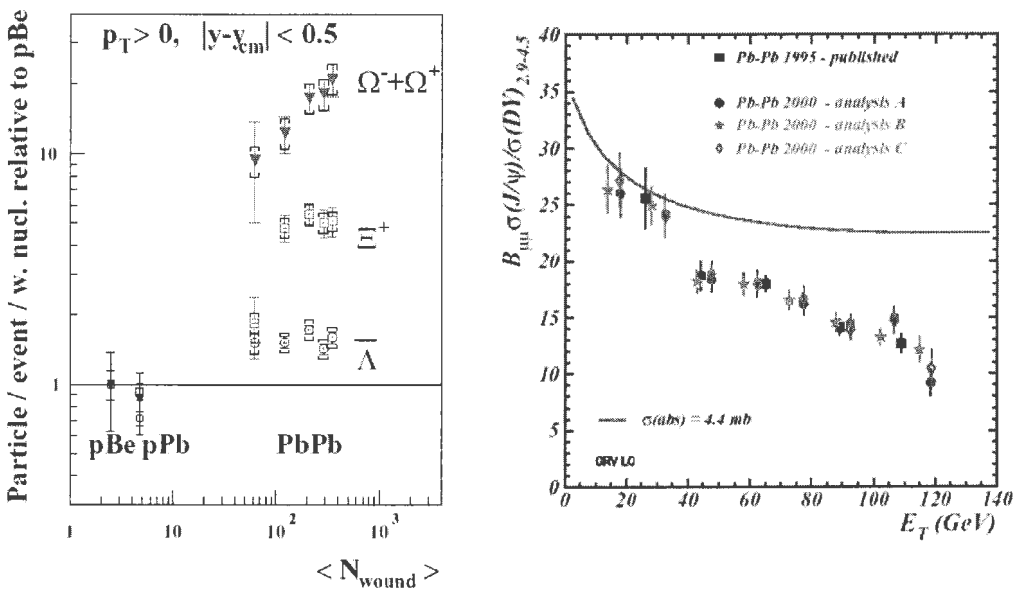

Figure 1.4: *Left: Hyperon yields per wounded nucleon per unit of rapidity at central rapidity in Pb-Pb relative to p-Be as a function of the number of wounded nucleons from NA57 experiment [13]. Right: Centrality dependence (expressed through the transverse energy E_T) of the J/Ψ production measured in the $\mu^+\mu^-$ channel in Pb-Pb collisions at 158 GeV/c by the NA50 experiment [14]; the solid line shows the predicted suppression due to nuclear absorption.*

J/Ψ suppression: The charmonium suppression was suggested as a QGP signature for the first time by T.Matsui and H.Satz in 1986 ([15]). *Charmonium*, $c\bar{c}$, and *bottonium*, $b\bar{b}$, are particular cases of bound systems formed by a (heavy quark)-(heavy antiquark) pair $Q\bar{Q}$[10], i.e. of *quarkonia* states. Quarks are produced in pairs, so c quarks are produced in $c\bar{c}$ pairs, because of flavour conservation. The produced c and $\bar{c}$ quarks travel different directories and hadronize (e.g. forming D-mesons). Only in rare cases the color interaction bounds them in a $c\bar{c}$ state, such as the J/Ψ hadron, before they separate. In the deconfined state it is expected that color interaction is screened for distances exceeding the *Debye length*, as are electromagnetic interactions in an electromagnetic plasma. This effect prevents the formation of hadrons whose radius is bigger then the Debye length. According to its dependence on the temperature T, charmonium can form only before the system cools down below a threshold temperature causing the suppression of the production of the charmonia states. This also indicates that quarkonia yields are related to the early parton-parton collision stage, while later stages cannot affect them. Nevertheless there is a normal J/Ψ suppression, already present in proton-nucleus and light ion-ion collisions, due to absorption of J/Ψ particles by the medium in which they are produced. The SPS experiment NA50, dedicated to J/Ψ studies, took into account the absorption of J/Ψ by the medium, plotting the normalized yields divided by the product AB of the atomic masses of the colliding ions; this showed a linear pattern in a log-log plot well fitting the yields of all collision systems but Pb-Pb, which showed the bigger anomalous suppression the higher the collision centrality (see right panel in figure 1.4).

1.2.2 RHIC: access to hard observables

The Relativistic Heavy Ion Collider (RHIC) at Brookhaven National Laboratories (BNL) has just concluded its fourth year run and has collected a vast database on p-p, d-Au and Au-Au collisions at $\sqrt{s_{NN}}$=20-200 GeV through its four experiments (BRAHMS, PHENIX, PHOBOS and STAR). With a factor $\sim$10 increase in the center-of-mass energy per nucleon pair with respect to the SPS, the energy density of the resulting fireball was predicted to be well above the deconfinement threshold value. The most important consequence of the increased collision energy with respect to the SPS is that it has allowed to turn on new interesting observables, in particular those related to the products of *hard scattering*, i.e. parton scattering with large momentum

[10]The convention uses the lower case letter q to indicate a generic light quark (u, d or s) and the upper case letter Q to indicate a generic heavy quark (c, b or t)

transfer, which is the primary source of hadrons with high transverse momentum (p_T>2 GeV): at RHIC perturbative QCD jet production rates are large enough to result in measurable yields up to $p_T \simeq 10$ GeV.
In an ultra-relativistic HI collision, hard scattering occurs before the deconfined phase is expected to form and thus the resulting hard hadrons, born before and decayed after QGP, are expected to probe the QGP medium. At RHIC in particular two of this probing effects were proposed as possible QGP signatures ([16], [17] and [18]):

in-medium parton energy loss Predicted for the first time by J.D.Bjorken in 1982 ([19]), this effect consists in the hadrons loosing energy while propagating in the hot and dense medium do to gluon bremsstrahlung ([20]), resulting in the suppression of hard jets (*jet quenching*) and, as a final measurable result, in depleted yields of high-p_T hadrons. This effect is not peculiar of hadrons traversing a deconfined medium, but in this case it is expected to be much larger because the emerging hard hadron interacts with (more and) much harder gluons than in the confined medium case.
The deviation of nucleus-nucleus (A-A) p_T-spectra from factorized perturbative QCD expectations is customarily expressed by means of the *nuclear modification factor* R_{AA}[11], which allows to focus on deviations of A-A yields from an incoherent superposition of nucleon-nucleon collisions, corresponding to R_{AA} deviating from unity. In the soft regime (p_T<1 GeV) the suppression of R_{AA} is related to parton shadowing. While ISR and SPS observed its enhancement at intermediate p_T [12], the most interesting result at RHIC is the

[11]The *nuclear modification factor* R_{AA} is defined as the ratio between the yields of charged hadrons in A-A collisions and in p-p collisions (scaled to the same energy) and divided by the estimated number of binary nucleon-nucleon collisions (given by the number of A-A collisions times the average number of inelastic nucleon-nucleon (NN) collisions per event $\langle N_{binary} \rangle$):

$$R_{AA}(p_T) = \frac{1}{N_{evt}\langle N_{binary}\rangle/\sigma_{inel}^{NN}} \frac{d^2N^{AA}/dp_T d\eta}{d^2\sigma^{NN}/dp_T d\eta}$$

Recalling that the nuclear overlap function is proportional to the number of nucleon-nucleon collisions according to $T_{AB}(b) = N_{coll}(b)/\sigma_{inel}^{NN}$, the nuclear modification factor (per event) is also written as:

$$R_{AA}(p_T) = \frac{d^2N^{AA}/dp_T d\eta}{\langle T_{AB}(b)\rangle \cdot d^2\sigma^{pp}/dp_T d\eta}$$

[12]This enhancement is explained as a result of the *Cronin effect* (see e.g. [21]), i.e. as a broadening of the transverse momentum distribution of the colliding partons before they undergo hard scattering

observation of a suppression of R_{AA} in Au-Au central collisions by a factor ~4. Figure 1.5 reports the results from PHENIX (in peripheral and central Au-Au collisions), which exhibit a depletion by factor ~4 for p_T>8 GeV in central $\sqrt{s_{NN}}$=200 GeV collisions w.r.t. incoherent nucleon-nucleon production expectations. Such a breakdown of the expected incoherent parton scattering assumption could be also ascribed to initial-state effects (modifications of the parton distribution functions in the colliding nucleons, often referred to as *shadowing*, leading to gluon saturation in the small-x regime) or to the breakdown of the collinear factorization itself (i.e. of the fundamental assumption that the hard inelastic cross sections for particle production can be factorized in the product of two incoherent terms: a long-distance and a short-distance term). This two effects are usually invoked in the context of the Color Glass Condensate theory. Comparison with N-A yields, is essential to disentangle initial and final state effects. Since the suppression does not appear in d+Au, it can be indeed ascribed to in-medium energy loss.

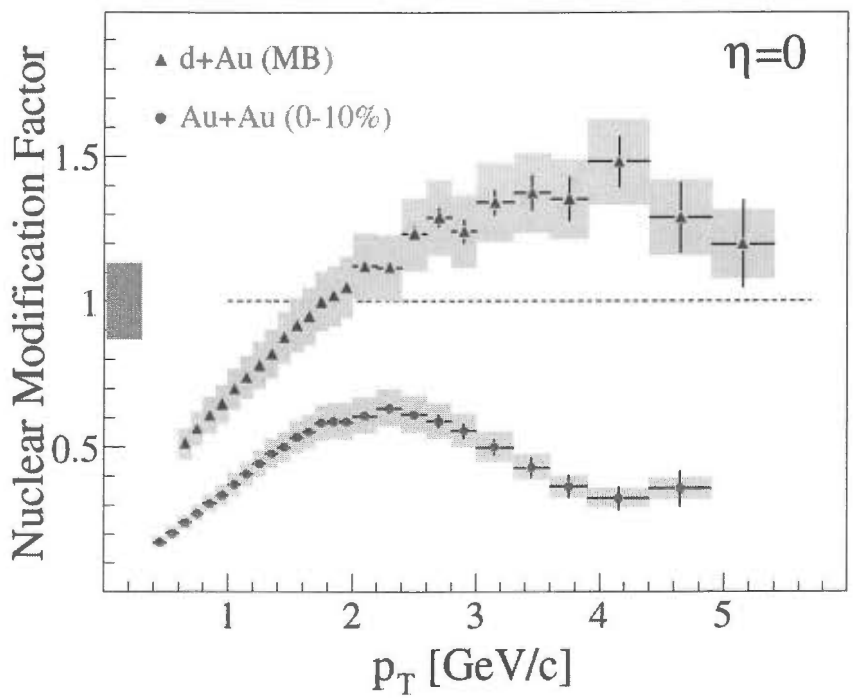

Figure 1.5: *Comparison of the nuclear modification factor $R_{AA}(p_T)$ [22] for d-Au and Au-Au minimum bias collisions at $\sqrt{s_{NN}}$=200 GeV.*

back-to-back azimuthal correlation suppression This effect is also due to hard hadrons interacting with the medium. When no deconfinement is expected, the charged particle distribution shows a peak at azimuthal angles ϕ opposite to that of a triggering high-p_T particle (i.e. for $\Delta\phi = \pm\pi$), indicating the likely occurrence of back-to-back emerging hadrons (or of their products). Figure 1.6 shows that peripheral collisions at STAR follow quite closely the p-p pattern (continuous line) while in central collisions the opposite-side peak doesn't appear any more. This is interpreted as the absorption by the dense and hot medium formed in central Au-Au collisions of one of the two jets (while the other can still emerge having to travel a shortest distance inside the medium).

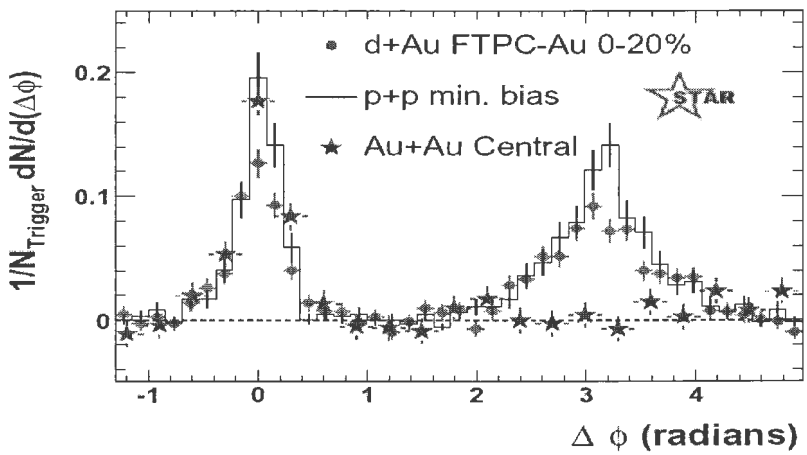

Figure 1.6: *Azimuthal correlations relative to a tagged p_T>4 GeV leading jet fragment as seen by STAR [23] for d-Au (red dots) and central Au-Au (blue stars) collisions; the black histogram is obtained for minimum bias p-p collisions. The correlations have been obtained after subtraction of correlations due to bulk elliptic flow.*

1.3 The QGP expected at the LHC

LHC start is scheduled for 2007; it will collide ion beams at center-of-mass energies about 30 times higher then those at RHIC and about 300 times higher than those at the SPS. This simple comparison allows rough quantitative predictions of the initial conditions and main parameters characterizing the system generated from LHC HI collisions. This quantitative description raise

the expectation of qualitatively new aspects of HI physics emerging at the LHC. In this section, after a concise review of the main observables at the LHC, we try to briefly describe this quantitative and qualitative novel aspects, leaving for the next chapter a through review of the physics aspects relevant for this thesis work.

1.3.1 Experimental observables

Initial conditions or medium properties are not directly observable, because of the rapid evolution and the limited spatial extent of the hot and dense matter produced after the collision. They can be traced back from the signals left into the detectors by the final state particles. Theory and HI experiments have selected the most important and promising among those signals; in this section we introduce the basic terminology related to HI observables.

Particle multiplicity

The initial energy density can be deduced from charged particle density and transverse energy density measured in the central rapidity region according to equation 1.2. For this reason the multiplicity variable enters the calculation of many other variables. From an experimental point of view, the particle multiplicity (and its distributions) is also fundamental since it determines detector performances (e.g. track resolution) and thus the accuracy of most of the measures; furthermore, at a fixed collision energy, it can be used as a measure of centrality, being directly related to the number of participant (or wounded) nucleons[13]. It is generally expressed through the charged particle multiplicity per unit of pseudorapidity $\frac{dN_{ch}}{d\eta}$ and often measured at midrapidity: $\langle\frac{dN_{ch}}{d\eta}\rangle_{|\eta|<1}$. The charged particle multiplicity derives its importance also from entering directly in Figure 1.7 shows the charged particle rapidity density as measured in p-p and Pb-Pb collisions over a broad center-of-mass energy range. Since charged particles hitting the detectors are mostly the result of final soft interactions, there is no first-principles derivation of its dependence from collision parameters; nevertheless quite a number of parame-

[13]Inclusive observables, as the transverse energy E_T, the energy collected around a small angle along the beam axis by the Zero Degree Calorimeter E_{ZDC} and the total multiplicity of charged particles N_{ch}, are used to trace back the number of participants N_{part}, i.e. the number of nucleons affected by the collision (and thus the number of spectators N_{spec}, i.e. nucleons outside the overlap of the colliding nuclei, not taking part into the collision) and the impact parameter b, i.e. the distance in the transverse plane between the flight lines of the two nuclei. The physics signals have then to be studied with respect to at least one of this variables which express the collision centrality, that is to say the overlap of the colliding nuclei.

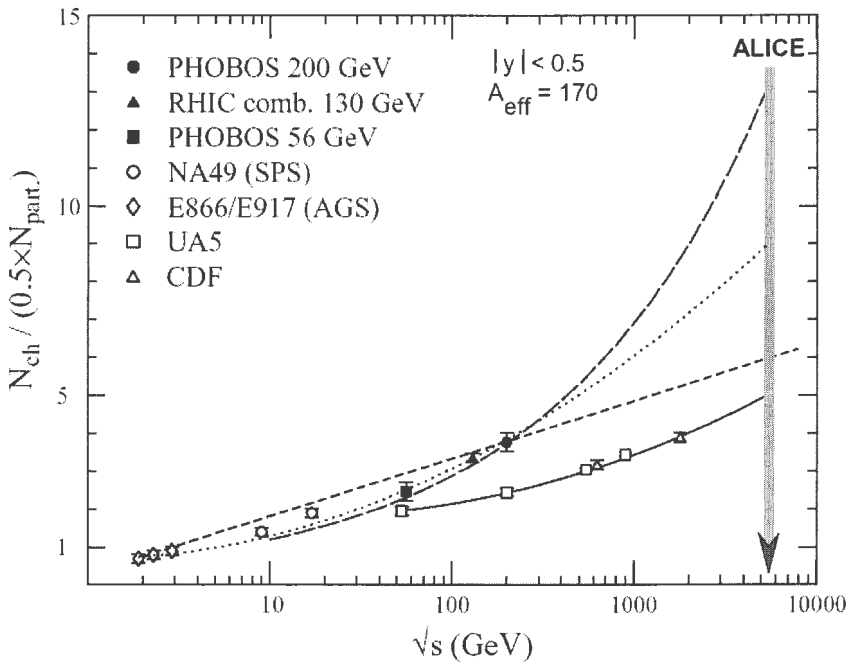

Figure 1.7: *Charged particle rapidity density per participant pair as a function of center-of-mass energy per nucleon pair at AGS, SPS and RHIC energies [24]. Lines show parameterizations of the energy dependence: logarithmic (dashed line), square logarithmic (solid and dotted lines, power low (long-dashed line). Intersections with arrowed line indicate possible extrapolations to the nominal LHC energy in Pb-Pb collisions.*

terizations of its center-of-mass energy dependence exist; RHIC experiments have measured $(dN_{ch}/d\eta)_{\eta=0}$ ≈700 at $\sqrt{s_{NN}}$=200 GeV, thus out-ruling the many models which predicted a much higher multiplicity. Present expectations for LHC Pb-Pb central collisions at $\sqrt{s_{NN}}$=5500 GeV lie in the range $(dN_{ch}/d\eta)_{\eta=0}$=2000-3500 ([25], [26]).

Soft probes

Soft probes are those more directly related to the observables of the bulk of light hadrons produced in the collision at the freeze-out stage, where soft processes[14] dominate. Analysis of this global soft-dominated observables (such

[14]Soft processes' space-time scales are of the order of the intrinsic hadronic scale Λ^{-1} ~1 fm and thus lie in the non-perturbative regime, in which the particles we see are colourless baryons and mesons. Thus soft processes in HI collisions are interactions at nucleon

as multiplicity distributions, particle abundances or transverse momentum spectra) can be sensitive to the formation of a deconfined phase and to its degree of thermalization. The most effective soft probes are here briefly mentioned, while some reference is given in the text for some in-deep discussion.

- Hadrochemical composition is a soft probe of the medium in the sense that the existence of a thermalized deconfined phase before hadronization and freeze-out should lead to a thermal spectrum of hadrons; thus a statistical-thermal analysis of the average multiplicities of various hadronic species, of their transverse momentum distributions and of baryon-to-antibaryon ratios should allow to derive thermal characteristics of the system (in particular temperature and chemical potential) at freeze-out.

- Particle correlations or *Bose-Einstein correlations* inside a chaotic medium allow *HBT interferometry*, a technique borrowed from astrophysics and applied in HEP on the momentum spectra, in particular of charged pions. This technique allows to determine the ratio between transverse flow velocity β_T and temperature T_F at freeze-out. Combined with analysis of transverse momentum spectra permits the estimation of the main freeze-out parameters.

- Strangeness enhancement has already been discussed among the QGP signatures at the SPS (see 1.2.1).

- Collective flow arises from the pressure-driven hydrodynamical expansion of the system produced by the collision; it is thus an event-by-event observable. Transverse or *radial flow* is the flow component in the transverse plane derived by inclusive p_T distributions of various particles species, of which it can determine the kinetic freeze-out time. *Elliptic flow* refers to the azimuthal anisotropy of particle multiplicities in semi-central events, arising from the almond-shaped overlap region in such events. It builds up through rescattering processes converting the larger pressure gradients along the line connecting the two nuclei's centers into larger momenta. This anisotropy is quenched by a rapid

level, as elastic proton-proton scattering or the production process $pp \to \pi + X$. Hard processes' space-time scales are instead much smaller than $\Lambda^{-1} \sim 1$ fm where, in the case of high momentum transfers, asymptotic freedom allows to apply perturbative QCD on point-like quarks and gluons; thus hard processes in heavy ion collisions are interactions at parton level, as for example $q\bar{q}$ annihilation into a heavy virtual photon generating a heavy dilepton pair (*Drell-Yan production*: $q\bar{q} \to \gamma \to (e^+e^-(\mu^+\mu^-))$ or gluon-gluon fusion resulting in heavy quark-antiquark pair ($gg \to Q\bar{Q}$).

expansion of the system; elliptic flow is thus sensitive to the degree of thermalization reached early in the collision.

Electromagnetic probes

Photons and leptonic observables are an exception in the sense that they are produced throughout the evolution of the system and interact with it only weakly 9due to their long mean free path), thus carrying information on the system status at all stages of the evolution.

- Direct photons are produced during the QGP phase mostly by quark-antiquark annihilation ($q\bar{q} \rightarrow g\gamma$) and gluon absorption by a quark with subsequent photon emission ($qg \rightarrow q\gamma$ or $\bar{q}g \rightarrow \bar{q}\gamma$). Both processes lead to energy and momentum distributions of the escaping photons similar to those of the two interacting partons; photons should then carry a wealth of information about partons forming the deconfined medium. Unfortunately their effectiveness is severely limited by the strong composite background from "prompt photons" (i.e. photons produced in primary nucleon-nucleon collisions) and hadronic decays from the final state (in particular the radiative decay of neutral pions $\pi^0 \rightarrow \gamma\gamma$), whose subtraction brings in big uncertainties.

- Thermal dileptons, l^+l^- couples, are produced in the QGP phase via quark-antiquark annihilation ($q\bar{q} \rightarrow l^+l^-$) and their production depends on (anti)quark momentum distributions inside the deconfined medium. As for photons, also for dileptons there are other contributions (from chiral phase transition following the QGP phase and from Drell-Yan pair production occurring in the pre-formation stage of the collision).

Hard probes

Deconfinement arises when all long-range effects are screened by the density of the constituents and is thus characterized by very short space-time scales. Consequently we need hard enough probes to see the medium at this short scales.

Hard Probes are high-energy probes of the Quark Gluon Plasma which are produced in the primary partonic collisions when fast moving partons are scattered through hard processes with a large transfer of energy (momentum), thus at a scale $Q \gg \Lambda_{QCD}$. Such hard probes include the production of DrellYan dileptons, massive gauge bosons, heavy quarks, prompt photons, and highp_t partons observed as jets and highp_t hadrons.

Usually hard probes are classified into hard probes and semihard probes according to their scales. The *hard probes* refer to observables with hard partonic subprocesses of energy exchange Q greater than several tens of GeV. For these hard probes, the processdependent nuclear effects (i.e., power corrections) should remain negligible. The *semihard* probes correspond to probes at moderate scales (Q from a few GeV up to 10-20 GeV) where the process-dependent nuclear effects may already be sizable in pA collisions and even larger in AA collisions.

Among hard probes, in particular hard partons in the incoming colliding nuclei taking part in hard scattering processes are well suited to probe the medium because:

- their production is unaffected by the medium;
- their production can be safely obtained by perturbative QCD calculations;
- the resulting yields and p_T distributions are expected to be significantly modified by the medium itself.

Indeed high transverse momentum partons yields are expected to be significantly reduced in the case of formation of a thermalized QGP medium *Jet quenching* and the back-to-back emerging hadron jets are expected to be deprived of the one jet which has to travel the longer distance inside the medium (*back-to-back azimuthal correlation* suppression. This two effects have already been described as QGP signatures at RHIC. A presentation of hard probes as physics observables at the LHC will be the subject of Chapter 2.

1.3.2 LHC experimental conditions

The Large Hadron Collider will accelerate beams of ions at a momentum of 7 TeV per unit of Z/A; this means that a generic ion (A,Z), i.e. with nuclear mass A and atomic number Z, will be accelerated at a momentum $p(A,Z) = \frac{Z}{A} \times 7$ TeV; the corresponding energy per nucleon pair attained in the center-of-mass frame in a (A_1,Z_1)-(A_2,Z_2) collision is:

$$\sqrt{s_{NN}} = \sqrt{(E_1+E_2)^2 - (\vec{p_1}+\vec{p_2})^2} \simeq \sqrt{4p_1p_2} = \sqrt{\frac{Z_1Z_2}{A_1A_2}} \times 14 \text{ TeV}$$

Thus, as an example, $\sqrt{s_{NN}} = 14$, 8.8 and 5.5 TeV is the c.m.s. energy per nucleon pair respectively in the case of proton-proton (p-p), proton-lead (p-Pb) and lead-lead (Pb-Pb) collisions at LHC. For asymmetric collision

systems, since the Z/A ratio for the two beams is very different, the nominal momenta for the two beams are also very different (7 TeV for protons vs. $\sim$ 3.5 TeV for ions) and the center-of-mass system of the collision moves w.r.t. the laboratory system; this corresponds to a shift in rapidity Δy for the laboratory system w.r.t. the center-of-mass system:

$$\Delta y = \frac{1}{2} \ln \frac{Z_1 A_2}{Z_2 A_1}$$

Since the ALICE experiment is asymmetric in the beam direction, both p-A and A-p runs are planned.

As explained in chapter 2, to understand the results obtained in HI collisions, other collision systems are needed: pp and p-Pb runs with reliable determination of centrality at the same collision energy as Pb-Pb interactions; a systematic study of p-A collisions, requiring a variety of collision energies and nuclei as well as a centrality scan; and an interchange of proton and nucleus beams for asymmetric detectors. In order to allow a systematic study of different collisions systems, the LHC running programme foresees ([27]):

- p-p runs at $\sqrt{s} = 14$ TeV;
- Pb-Pb physics pilot run;
- 1-2 years Pb-Pb at $\sqrt{s_{NN}} = 5.5$ TeV;
- 1 year p-Pb like collisions (mostly p-Pb at $\sqrt{s_{NN}} = 8.8$ TeV, then d-Pb or α-Pb at $\sqrt{s_{NN}} = 6.2$ TeV);
- 1-2 years Ar-Ar at $\sqrt{s_{NN}} = 6.3$ TeV;

Lead-lead collisions will provide the highest energy density and will constitute the main arena for the LHC heavy ion programme. After a first pilot run, some further couple of years is needed to reach the required statistics for low cross section observables (hard processes in particular). Proton-proton and proton-nucleus runs are needed as terms of comparison for the observables in nucleus-nucleus collisions. To study the dependence of some observables from the energy density of the system, lower mass ion systems (as argon-argon) are also important. Later on Pb-Pb runs at lower energy (to better connect with available RHIC results) and p-A runs at varying A (to map the A-dependence) are also planned.

1.3.3 LHC heavy-ion physics

The much higher energy in the collision center of mass at the LHC w.r.t. SPS and RHIC will result in very different expected values for the main global variables describing the system after the collisions: a comparison between these values at SPS, RHIC and LHC is shown in table 1.1.

Parameter	units	SPS	RHIC	LHC
$\sqrt{s_{NN}}$	GeV	17	200	5500
dN_{ch}/dy		400	650	$\simeq$ 3000
Initial temperature	MeV	200	350	>600
Energy density	GeV/fm^3	3	25	120
Freeze-out volume	fm^3	$\sim 10^3$	$\sim 10^4$	$\sim 10^5$
Life-time	fm/c	~ 1	2-4	>10

Table 1.1: *Comparison of some global variables relative to central nucleus-nucleus collisions at SPS, RHIC and LHC energies.*

The energy per nucleon pair in the center of mass at LHC is about 30 times higher then at RHIC; it is expected that this will imply a substantially higher initial energy density and a doubling of the initial temperature; since the system expands while cooling down, a higher initial temperature implies also a longer life time and freeze-out volume, which is the volume of the system before it has reached the critical temperature $T_c \simeq 170$ MeV. Thermalization is expected to occur sooner because of the higher density of gluons allowing a more efficient momentum exchange. Let's summarize the quantitative difference of the collisions' products at LHC from those at RHIC: the LHC will produce hotter, bigger and longer-lasting QGP fireballs (this scenario is sometimes referred to as *deep deconfinement*). Therefore it is believed that this system will be also characterized by clearer QGP signatures. In particular there are two main motivations to believe that the QGP at LHC will be much better described by lattice QCD:

- as previously mentioned (section 1.1.1), lattice QCD calculations need to assume a baryon-free system; the baryon content of the system resulting from the collision must be equal to the baryon number carried by the two colliding nuclei (i.e. 2A) and is expected to be mostly carried away at rapidities closed to the beam rapidities (2.9, 5.3 and 8.6 at SPS, RHIC and LHC respectively [15]). Therefore at mid-rapidities

[15] This values are obtained as $\sinh^{-1}\sqrt{s_{NN}}$ for SPS, having a fixed target, and as $\sinh^{-1}\left(\sqrt{s_{NN}}/2\right)$ for RHIC and LHC, studying head-on collisions, according to ...

LHC will be characterized by an almost null baryochemical potential;

- the results for the energy density ϵ/T^4 from lattice QCD (fig. 1.2), in particular in the case of 2+1 flavours, clearly show that non-perturbative effects, not accounted for by lattice QCD, continue to be important up to temperatures far higher than the critical value. [16] Thus, the higher the initial temperature, the smaller the gap to the asymptotic value ϵ_{SB}/T^4.

In the absence of nuclear and medium effects a generic A-B nucleus-nucleus collision could be seen as the superposition of a number of independent inelastic nucleon-nucleon collisions and thus the cross section for hard processes would scale linearly with the number of participating (or wounded) nucleons. This *binary scaling* picture fitted for example the Drell-Yan cross section in p-A collisions where $\sigma_{DY}^{pA} = A\sigma_{DY}^{pp}$; but soon new effects appeared which let this simple scaling break down. These effects are divided into:

- *initial-state effects* are the effects on the way partons in nucleons of one nucleus "see" partons in nucleons of the opposite colliding nucleus, due to the presence of other nucleons. By definition, this effects show a dependence on the size and energy of the colliding nuclei, independently of the medium formed after the collision. Examples are p_T-broadening and parton distribution functions' modifications (which will be discussed later).

- *final-state effects* are the effects hard partons experience due to the presence of the medium. Having (or not having) to traverse a medium, hard partons give eventually rise to hard hadrons yields, rapidity-, p_T-distributions modified by the medium according to its properties (gluon density, temperature, volume).

For HI experiments it is of paramount importance to disentangle initial-state and final-state effects; for this reason HI runs need to be compared not only to baseline p-p runs (giving cross sections for nucleon-nucleon interactions) but also to proton-nucleus runs to see which effects modify the binary scaling expectations also in the absence of a QGP medium and with which A-dependence. A pictorial representation of this procedure is given in Fig.1.8.

The higher energy density, larger freeze-out volume and longer life-time at the LHC raise the expectation of enhanced physics signals of the plasma phase

[16] This is not surprising if we recall that the strong coupling constant goes inversely with the temperature.

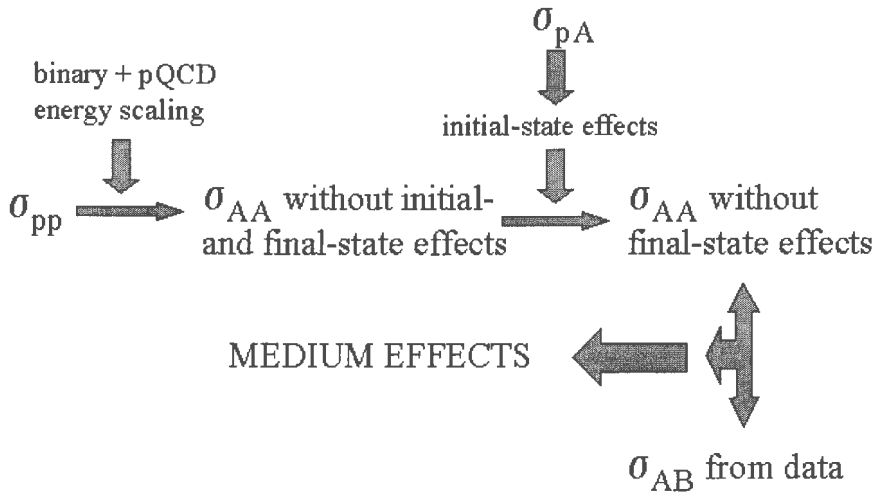

Figure 1.8: *Schema of how p-p, p-A and A-A cross sections allow to discriminate initial-state and final-state effects.*

due to the QGP phase dominating the fireball expansion. As a consequence also the collective features of the final hadronic state are expected to be strongly dominated by the QGP phase dynamics. But there are in particular two qualitatively novel aspects which will characterize the HI physics at LHC:

1. accessing new regions of phase-space where parton densities are expected to be close to saturation, the LHC will operate in a regime of strong *nuclear shadowing*, resulting in the suppression of inelastic scattering with low-momentum transfer.

2. hard processes are expected to significantly contribute to the total A-A cross section. Thus hard probes should allow a deep understanding of the deconfined medium they traverse;

We explain these aspects in the following chapter.

Chapter 2

Heavy quark physics and multi-parton scattering at the LHC

Hard and semi-hard probes, briefly introduced in Section 1.3) in the context of QGP probes at RHIC, will be particularly relevant at LHC energies; the ALICE experiment, with its physics program covering a wide set of collision systems, will allow the comparison of heavy quark yields and distributions in p-p, p-A and A-A collisions, which will be fundamental to calibrate the A-A measurements, where, in central collisions, the formation of the QGP is expected. In this chapter we treat some relevant aspects of the physics of heavy quarks at the LHC, with some emphasis on the role of their study in p-A collisions.

Heavy quarks are ideal probes of the medium because of the large virtuality Q associated to the primary partonic scatterings originating them; this has in particular two consequences:

- the heavy quark production cross sections are safely calculated in the framework of perturbative QCD (indeed $Q \gg \Lambda_{QCD}$ implies $\alpha_s \propto \frac{1}{\ln(Q^2/\Lambda^2_{QCD})} \ll 1$, and thus orders higher than the next-to-leading order (NLO) will be small enough to be neglected;

- the formation time $\Delta\tau$, which is proportional to $1/Q$, will be small enough to leave the production of $Q\bar{Q}$ pairs unaffected by the medium properties.

The range of energies available at the LHC will allow to considerably extend the knowledge on the fractional momenta distributions of partons inside hadrons (Parton Distribution Functions, PDFs); a comparison between

different collision systems will also allow to measure the modifications to this distributions due to interactions of partons with partons of nearby nucleons; this nuclear effects are responsible for the fact that the effective parton distributions of a large nucleus (nuclear Parton Distribution Functions, nPDFs) differ from a simple scaling of the PDFs inside a single nucleon. In Section 2.1 we introduce the role and present knowledge of PDFs and we give an estimation of the range of partonic fractional momenta which will be accessible at the LHC.

The interaction probability between incoming high-p_t partons to produce heavy quarks is determined by the PDFs characterizing the colliding nucleons; thus the production yields of heavy quarks will allow to trace back the PDFs. Heavy quarks as hard probes detected in p-p, p-A and A-A collision systems, since subject to the factorization theorem, will allow to disentangle the medium effects arising in central heavy ion collisions; in the semihard regime they help to understand the size of the nuclear modifications not caused by the dense medium. For both regimes their values in p-p and p-A collision systems are thus needed as references for the QGP signals in A-A collisions. In Section 2.2 we present an overview of the most important issues in heavy quark physics which will be relevant at the LHC: the channels and cross sections for the production of heavy quarks and the sensitivity of heavy quarks to nuclear and in-medium effects.

The resulting cross sections of the semihard probes in p-A collisions are also needed for the study of multiple parton scattering in nuclear matter and its corresponding dependences beyond the nuclear effects included in the nPDFs; this issue is presented in Section 2.3.

2.1 PDFs and accessible x-range

2.1.1 Parton Distribution Functions (PDFs)

The LHC will allow to probe the parton distribution functions of the nucleon and, in the case of proton-nucleus and nucleus-nucleus collisions, also their modifications in the nucleus, down to unprecedented low values of x. *Parton distribution functions* (PDFs) are the distributions, for each type of parton (q, $\bar{q}$ or g) of the Bjorken's x (x_{Bj} or simply x, see appendix.A); this means that e.g the gluon PDF $f_g(x, Q)$ gives the probability that a gluon taking part in the hard scattering carries a certain momentum fraction x (w.r.t. the nucleon to which it belongs) at the scale Q[1]. In p-p collisions, it

[1] Q^2 is also known as *virtuality*, and is given by $Q^2 \equiv -q^2$, where q is the four-momentum of the exchanged virtual photon; thus Q indicates the typical momentum transfer.

is well established that the inclusive cross sections of these hard processes can be computed through collinear factorization, i.e. using short-distance cross sections of parton-parton scatterings and well-defined universal parton distribution functions (PDFs). While the partonic sub cross sections and the scale evolution of the PDFs are calculable in perturbative QCD (pQCD), the PDFs contain non-perturbative information which must be extracted from the measured cross sections of various hard processes. Provided that leading-power collinear factorization is applicable also in A-A collisions, the cross sections of hard probes can be used as benchmark cross sections against which the signals and properties of the QGP can be extracted. Therefore, it is of extreme importance that the applicability of factorization will be tested in p-A interactions, especially at the LHC where truly hard probes (with momenta of order 100 GeV/c) will finally become available for nuclear collisions.

Our knowledge on PDFs derives mainly from deep inelastic lepton-hadron scattering (DIS) of leptons on hadrons, in particular from HERA data for the small-x region (down to x=10^{-4}). In this region PDFs show a rapid increase as predicted by perturbative QCD; it is however expected that this increase will stop at smaller x, in particular in the x-range where the gluon PDF f_g exceeds the see-quarks PDF f_{sq} by more than one order of magnitude; this is because when the density of partons inside the proton becomes too high they cannot be treated as free any more and gluon recombination effects are expected to limit any further growth of PDFs. The LHC will allow to access small-x regions, not yet explored, which heavily determine charm and beauty production cross sections; therefore, the measurement of heavy flavour production at the LHC may provide new insights on the nuclear parton densities.

2.1.2 Accessible x-range at the LHC

We want to show here how the x-range actually probed depends on the collision system (through the c.m.s. energy per nucleon pair $\sqrt{s_{NN}}$), on the detector acceptance (through the accessible rapidity range) and on the hard probe considered (through its invariant mass[2]). Thus we will be able to compare the values of x corresponding to the production of a $c\bar{c}$ pair at SPS, RHIC and LHC energies and to estimate the x-range that can be accessed with ALICE for what concerns heavy flavour production.

To see the relationship between accessible rapidity and accessible x-range, let's consider a 2→2 process where two partons inside opposite colliding ions,

[2]The invariant mass of two particles with four-momentum $(E_1, \vec{p_1})$ and $(E_2, \vec{p_2})$ is defined as the modulus of the total four-momentum: $M_{12} = \sqrt{(E_1 + E_2)^2 + (\vec{p_1} + \vec{p_2})^2}$.

(A_1,Z_1) and (A_2,Z_2), undergo a hard-scattering originating a heavy quark pair $Q\bar{Q}$ (this could be for instance the case of the leading order[3] gluon-gluon fusion process $gg \rightarrow Q\bar{Q}$, shown in Figure 2.1). The involved nucleons

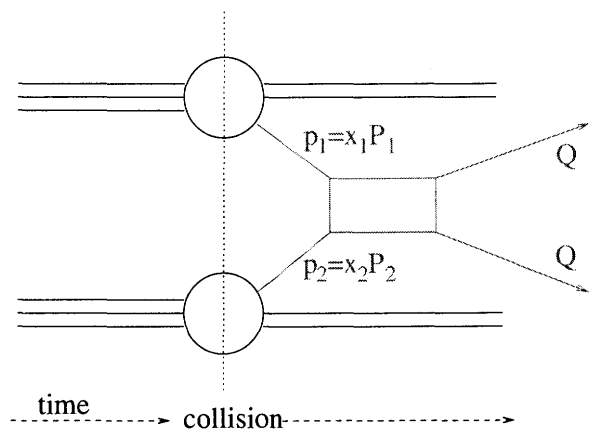

Figure 2.1: *Graphical representation of the scattering of two partons resulting in a $Q\bar{Q}$ pair production.*

inside the two colliding ions are accelerated at ultra-relativistic energies, so we can safely neglect their masses when writing their four-momenta P_1 and P_2:

$$P_1 = (1,0,0,1) \cdot \frac{Z_1}{A_1} \cdot \frac{\sqrt{s_{NN}}}{2} \qquad \text{and} \qquad P_2 = (1,0,0,-1) \cdot \frac{Z_1}{A_1} \cdot \frac{\sqrt{s_{NN}}}{2}$$

When writing the four-momenta p_1 and $p_2$of the two hard-scattering partons, we can again neglect their masses and their transverse momentum inside the nucleon, since they are much smaller than the momentum along the beam direction:

$$p_1 = (x_1,0,0,x_1) \cdot \frac{Z_1}{A_1} \cdot \frac{\sqrt{s_{NN}}}{2} \qquad \text{and} \qquad p_2 = (x_2,0,0,-x_2) \cdot \frac{Z_2}{A_2} \cdot \frac{\sqrt{s_{NN}}}{2}$$

where x_1 and x_2 are the momentum fractions carried by the partons (gluons), and $\sqrt{s_{NN}}$ is the c.m.s. energy per nucleon pair, e.g.14 TeV at the LHC for p-p collisions.

The energy in the collision c.o.m. system turns out to be just the invariant

[3]Leading order (LO) is $\mathcal{O}(\alpha_s^2)$; next-to-leading order (NLO) is $\mathcal{O}(\alpha_s^3)$.

mass of the parton-parton (and thus of the $Q\bar{Q}$) system:

$$\begin{aligned} M^2_{Q\bar{Q}} &= M^{(12)^2} = E^2_{c.o.m.} = (p_1 + p_2)^2 \\ &= \frac{s_{NN}}{4}\left(\frac{Z_1}{A_1}x_1 + \frac{Z_2}{A_2}x_2, 0, 0, \frac{Z_1}{A_1}x_1 - \frac{Z_2}{A_2}x_2\right)^2 \\ &= s_{NN}\frac{Z_1}{A_1}x_1\frac{Z_2}{A_2}x_2 \end{aligned} \tag{2.1}$$

The longitudinal rapidity of the parton-parton (and thus of the $Q\bar{Q}$) system w.r.t. the laboratory system is:

$$y_{Q\bar{Q}} = y_{(1,2)} = \frac{1}{2}\ln\left(\frac{E^{(12)} + p_z^{(12)}}{E^{(12)} - p_z^{(12)}}\right) = \frac{1}{2}\ln\left(\frac{x_1}{x_2}\cdot\frac{Z_1A_2}{Z_2A_1}\right) \tag{2.2}$$

Combining equations 2.1 and 2.2, we obtain the dependence of x_1 and x_2 on rapidity of the two newly produced quarks ($y_{Q\bar{Q}}$), given their invariant mass ($M_{Q\bar{Q}}$) and the c.o.m. energy of the colliding system:

$$x_1 = \frac{A_1}{Z_1}\cdot\frac{M_{Q\bar{Q}}}{\sqrt{s_{pp}}}e^{+y_{Q\bar{Q}}} \quad \text{and} \quad x_2 = \frac{A_2}{Z_2}\cdot\frac{M_{Q\bar{Q}}}{\sqrt{s_{pp}}}e^{-y_{Q\bar{Q}}}$$

In the particular case of p-p collisions (A_1=Z_1=A_2=Z_2=1) this simplifies to:

$$x_1 = \frac{M_{Q\bar{Q}}}{\sqrt{s_{pp}}}e^{+y_{Q\bar{Q}}} \quad \text{and} \quad x_2 = \frac{M_{Q\bar{Q}}}{\sqrt{s_{pp}}}e^{-y_{Q\bar{Q}}}$$

At central rapidities we have $x_1 \simeq x_2 \simeq \frac{M_{Q\bar{Q}}}{\sqrt{s_{pp}}}$; at fixed rapidity the lower x-limit is obtained at the threshold, where the invariant mass of the quark pair is given only by the masses of the constituent quarks ($M_{c\bar{c}} = 2m_c \simeq$2.4 GeV, $M_{b\bar{b}} = 2m_b \simeq$9 GeV). As a comparison we show in Table 2.1 the lower x-limit at central rapidities for different collision systems, and associated energy per nucleon pair, at the RHIC and LHC colliders. The x-regime relevant to charm production at the LHC ($\sim 10^{-4}$) is about 2 orders of magnitude lower than at RHIC and 3 orders of magnitude lower than at the SPS. Because of its lower mass, charm allows to probe lower x-values than beauty. The capability to measure charm and beauty particles in the forward rapidity region ($y \simeq$4) would give access to x-regimes about 2 orders of magnitude lower, down to $x \sim 10^{-6}$.

Asymmetric collisions, such as p-Pb and Pb-p, where by convention the first ion is the one going in the positive-z direction, are characterized by a

Collider System@$\sqrt{s_{NN}}$	RHIC Au-Au@200GeV	LHC p-p@14TeV	LHC Pb-Pb@5.5TeV
$c\bar{c}$	10^{-2}	$2{\cdot}10^{-4}$	$4{\cdot}10^{-4}$
$b\bar{b}$		$6{\cdot}10^{-4}$	$2{\cdot}10^{-3}$

Table 2.1: *Approximate Bjorken's x values for charm and beauty production at threshold at central rapidity for different collision systems.*

rapidity shift: from equation (2.2), using $x_1 = x_2$, we see that the centre of mass moves with a longitudinal rapidity w.r.t. the laboratory system:

$$y_{c.o.m.} = \frac{1}{2} \ln \left(\frac{Z_1 A_2}{Z_2 A_1} \right)$$

The rapidity window covered by the experiment is consequently shifted by $y_{c.o.m.}$ corresponding to +0.47 (-0.47) in the case of p-Pb (Pb-p) collisions. Therefore, running with both p-Pb and Pb-p will allow to cover the largest interval in x.

2.2 Open heavy flavour physics

Physics and experimental issues related to hadrons containing charm (beauty) are quite different whether they have zero charm (beauty) quantum number or not; hadrons of the first type are called *hidden charm (beauty)* and contain a $c\bar{c}$ ($b\bar{b}$) bound state; in the second case they are referred to as *open charm (beauty)*.

As seen in the previous section, the detection at central rapidities at the LHC of open heavy flavour and of open charm in particular, will give access on parton distributions in the proton and in the nucleus down to $x \sim 4 \times 10^{-4}$ and $x \sim 10^{-3}$ for charm and bottom respectively, where direct information is presently lacking not only in the nucleus but even in the proton. Furthermore its comparison in different collision systems could disentangle nuclear effects, i.e. modifications on the PDF due to the presence of other nucleons (nuclear parton distribution functions (nPDFs)). For this reason heavy quark production will be an important part of the LHC program, with both open heavy flavors and quarkonium studied extensively. However open heavy flavor production is a better direct test of the nuclear parton distribution than quarkonium, which is subject to other cold matter effects such as nuclear absorption.

In this section we give a brief overview of the production mechanisms of open heavy flavours and of the physical effects they allow to study, i.e.

effects on the inside of a nucleon due to the presence of other nucleons (nuclear effects) and effects due to the formation of a QGP medium (in-medium effects).

It has to be mentioned that an important task for open charm physics at the LHC is also to serve as a reference for J/Ψ measurements, which, as explained in the context of QGP probes at the SPS, are expected to be considerably affected by the formation of a deconfined phase. At the SPS energies charm quarks are mainly produced via quark-antiquark annihilation and thus the dilepton continuum produced by Drell-Yan processes ($q\bar{q} \rightarrow l^+l^-$) could be used as a normalization reference for the production of the J/Ψ. Since at the LHC heavy quarks will be mainly produced by gluon-gluon fusion another normalization reference is needed: open charm measurements can offer this normalization benchmark for charmonia production.

2.2.1 Heavy quark production at LHC

The leading order processes for the production of heavy quarks in hadron-hadron collisions are pair creation processes: gluon-gluon fusion ($gg \rightarrow Q\bar{Q}$) and quark-antiquark annihilation ($q\bar{q} \rightarrow Q\bar{Q}$; at LHC energies the first will be dominant, while the second dominates at SPS energies. At NLO other processes lead to the production of heavy quarks: they can come directly from a gluon splitting ($g \rightarrow Q\bar{Q}$) or, after being produced, they can scatter off a parton of some opposite colliding nucleon ($Qg \rightarrow Qg$ or $Qq \rightarrow Qq$) in a flavour excitation processes.

The partonic cross sections depend on the partonic center of mass energy $\hat{s}^2$ squared , on the heavy quark mass m_Q and on the factorization and renormalization scales (μ_F and μ_R). Their calculation has been performed only up to NLO, but at LHC energies the weight of smaller orders is expected to be negligible. The total hadronic cross section is obtained by convoluting the total partonic cross section with the parton distribution functions of the colliding hadrons. E.g. for p-p collisions:

$$\sigma_{pp}^{Q\bar{Q}}(s, m_Q^2) = \sum_{i,j=q,\bar{q},g} \int_{\frac{4m_Q^2}{s}}^{1} \frac{d\tau}{\tau} \delta(x_i x_j - \tau) \frac{f_i^p(x_i, Q^2)}{x_i} \frac{f_j^p(x_j, Q^2)}{x_j} \hat{\sigma}_{ij}(\tau, m_Q^2, Q^2) \tag{2.3}$$

where the sum index i runs over all massless partons, $\tau = \hat{s}/s$ and x_i and x_j are the fractional momenta of the two scattering partons. The parton densities are evaluated at the scale Q, usually chosen to be equal to the renormalization scale.

Charm production in p-A collisions has been studied quite extensively up to $\sqrt{s_{NN}} \approx 40$ GeV and in this range its energy dependence (well reproduced

by the PYTHIA model) as well as its A–dependence (which agrees with the binary scaling $\sigma_{pA}^{c\bar{c}} = A \cdot \sigma_{pp}^{c\bar{c}}$ for minimum bias events) have been understood. In A-A collision systems, instead, the knowledge on charm production, deriving from SPS and RHIC measurements, is presently affected by quite big uncertainties and not well understood.

2.2.2 Charm production cross sections

Charm production cross section at the LHC energies need to be inferred from measured values at lower energies by making use of LO or NLO order calculations and assuming some set of parton distribution functions. Different choices of the PDF set do not cause huge variations of the resulting cross-sections (of order 25%), which are more affected by the choice of the other parameters to be fixed, as the mass of the c quark m_c and the factorization and renormalization scales, μ_F and μ_R, which lead to variations even of a factor 4, as discussed in [28]. In the present thesis work, for the proton-proton charm cross section production we will use the values reported in Table 2.2 resulting from the calculations implemented in the code HVQMNR ([29])

	$\sigma_{pp}^{c\bar{c}}$[mb]		
$\sqrt{s}$	5.5 TeV	8.8 TeV	14 TeV
MRST HO	5.9	8.4	10.3
CTEQ 5M1	7.4	9.6	12.1
Average	6.6	9.0	11.2

Table 2.2: *Approximate Bjorken's x values for charm and beauty production at threshold at central rapidity for different collision systems.*

avareged over the two sets of PDFs MRST HO ([30]) and CTEQ 5M1 ([31]) as described in [32]. The extrapolation to proton-nucleus collisions using the Glauber model leads to the simple relation: $\sigma_{pA}^{hard} = A\sigma_{pp}^{hard}$. and the yield can be derived from it deviding by the total inelastic cross section (which in the case of p-Pb collisions at the LHC is estimated to be σ_{pPb}^{inel}=1.9 barn ([33])) and we have:

$$N_{pA}^{hard} = \frac{A\sigma_{pp}^{hard}}{\sigma_{pA}^{inel}} \Rightarrow N_{p-Pb}^{c\bar{c}} = \sigma_{pp}^{c\bar{c}} \cdot 0.109 mb^{-1} = 0.98$$

Accounting for the nuclear shadowing by means of the EKS98 ([34]) parameterization this value is lowered to $N_{p-Pb}^{c\bar{c}} = 0.78$, that is by a factor of about 20% ([32]).

2.2.3 Nuclear modification effects

Since heavy quarks production cross sections are obtained as in Equation 2.3 by the convolution of partonic cross sections with the PDFs of the colliding hadrons, heavy quark yields will give informations on the PDFs and in particular will be sensitive to their modifications caused by the presence of other nucleons around the nucleon directly involved in the partonic interaction (nuclear modification effects).

Nuclear shadowing

The most important nuclear effect, known as *nuclear shadowing effect*, is a suppression of the nuclear PDFs in the low-x region with respect to proton PDFs; it can be intuitively understood as a melting of the "too many" partons carrying a tiny fraction of the hadron momentum into a harder parton with fractional momentum given by the sum of the fractional momenta of the two melted partons. Measurements for this effect have been performed down to $x_{Bj} \sim 10^{-3}$ in electron-nucleon DIS and have been explained by various models (See [35] for a review of them). However their predictions outside the measured range are quite conflicting; thanks to the significant lowering of the lower bound for the accessible x_{Bj}, the LHC will offer a unique opportunity to study this effect and to at least rule out some of this models. Their predictions are expressed usually in terms of the Pb gluon distribution relative to the proton, by means of the ratio: $R_g(x, Q^2) = \frac{g_{Pb}(x,Q^2)}{g_p(x,Q^2)}$ Figure 2.2 plots the $R_g(x, Q^2)$ ratios as foreseen by different models. The shadowing effect results in a depletion of the heavy quark production cross section per binary collision in p-A and A-A collision systems, which thus can be used to quantify it.

A second nuclear modification effect, which can set itself against the nuclear shadowing, is the so called *k_t-broadening*; it consists in the enhancement in p-A and A-A collisions of the intrinsic transverse momentum k_t which as to be assigned to the partons taking part in the collision in order to reproduce experimental data. However this moderate effect is expected to affect slightly the c quark p_t-distribution, while leaving unchanged its p_t-integrated cross section.

2.2.4 In-medium modification effects

After the formation, heavy quarks traverse the medium produced by the collision, which is expected to be a deconfined medium only in central heavy ion collisions. While traversing the QGP they are expected to loose more

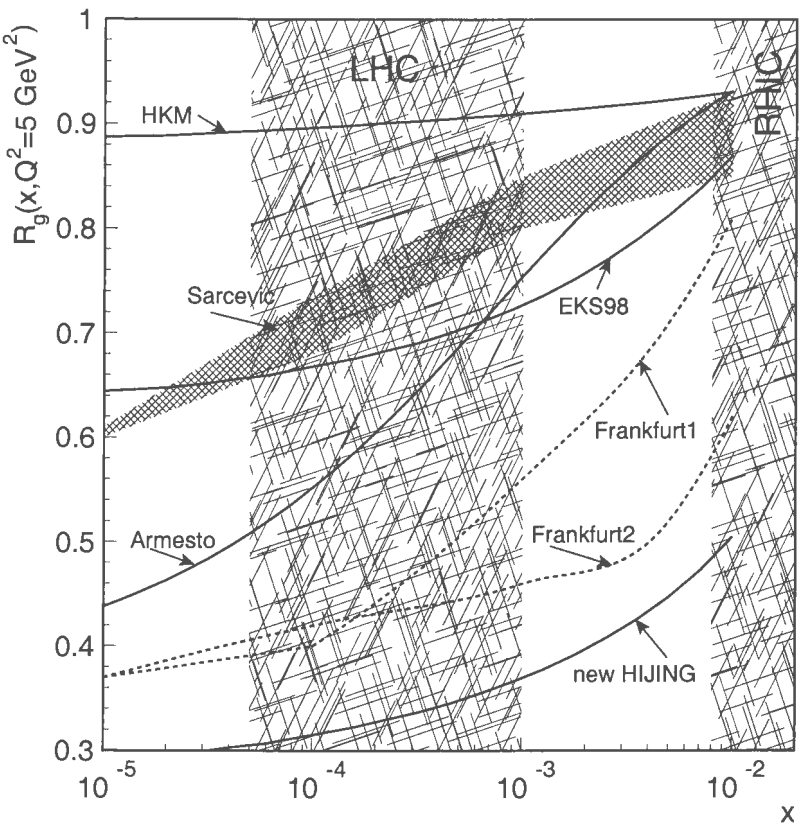

Figure 2.2: *Ratios of gluons distributions for lead w.r.t. proton according to different models at Q^2=5 GeV^2. The shaded areas correspond to RHIC and LHC accessible x-ranges.*

energy then in the case of a confined medium, in particular because they will interact with more energetic partons. The interactions with the gluons of the QGP will be of two types: elastic scattering (which first led to the prediction of this effect) and "gluon bremsstrahlung", i.e. inelastic scattering of the parton with the QGP gluons and induced gluon radiation at the expense of the parton's momentum, which will be quenched (attenuated). Since high-momentum partons are more sensitive to this medium-induced radiative energy loss, the effect will finally be observed as a depletion of heavy quark yields at high p_t. The observations from RHIC raise the expectation that the comparison of light-flavour and heavy-flavour hadrons at relatively high p_t (5 GeV $< p_t <$ 20 GeV) will allow a "tomography" of the deconfined medium produced at the LHC.

2.3 Multiple heavy quark pairs production at LHC

The energies per nucleon pair available at LHC collisions will be so high that even partonic interactions involving a very small fraction of the total energy available at hadronic level will still be safely treated by means of pQCD, because the energy exchanged at partonic level is still much higher than the hadronic scale. In other words the semi-hard regime will be accessible: in this kinematical regime the partonic momentum fraction x may be very small and, as a consequence, the partons number density may be very large. The fast increase of parton distributions at small-x gives rise to a growing flux of partons. Since each incoming hadron is an extended object, at high energies it seems reasonable to expect several parton pairs to interact in separated points in transverse space, in the same hadronic event: such an occurrence is called a *multipartonic interaction* or *multiparton scattering*. We can than represent the colliding nucleon as a beam of partons; the large flux of partons at small momentum fractions provides a sizable probability of multiparton scatterings, where different pairs of partons interact simultaneously; we thus need to take into account collision events in which more partons inside the same nucleon interact with partons belonging to one or more nucleons of the opposite colliding nucleus; the two cases when only one or more target nuclei are involved in the process are sometimes referred to as normal and anomalous multiparton scattering (see Figure 2.3 for the specific case of double-parton scattering events), the first dominating at high momenta. The probability for the occurrence of such multiparton events will depend on the many-body parton distributions, which contain much more information on the hadron structure than the single-body parton distributions usually considered in pQCD calculations (the usual PDFs). They are indeed related to the parton correlations, which are generated by the underlying strong interaction dynamics. Hence multi-parton interactions are of great interest because they are a promising tool to investigate the three-dimensional partonic structure of hadrons ([36], [37]).

The proton-nucleus collision systems [38] will offer considerable advantages for studying multiparton collisions, where the production rates are significantly enhanced due to the increased flux of incoming partons. Moreover, the rate of multi-parton processes can be varied with the nuclear targets at fixed centre-of-mass energy and with the same cuts in the produced final state.

The first measurement of double-parton collisions was performed at the Tevatron [39, 40] selecting final states with three jets and a photon. These

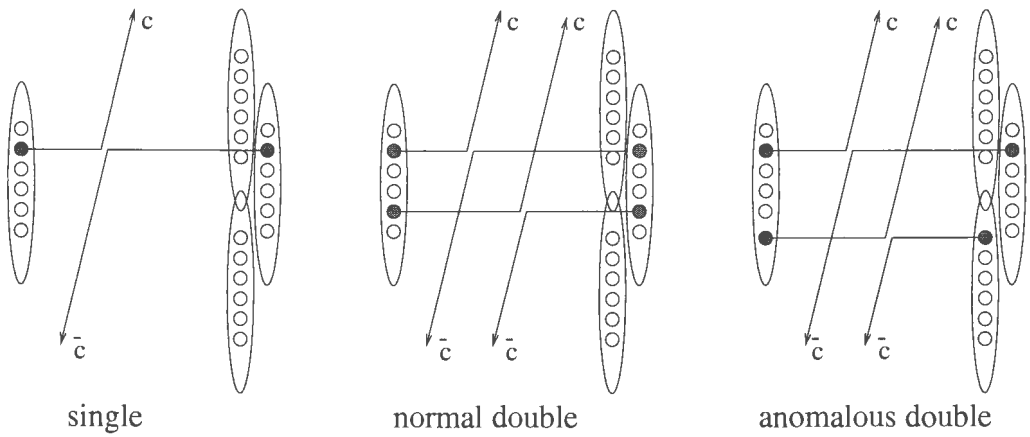

Figure 2.3: *Graphical comparison of single-, normal double- and anomalous double-parton scattering events.*

results indicate non-trivial correlations of the proton structure in transverse space [41, 42]. The structure of the proton appears to be much richer than the independent superposition of single-parton distribution functions accessible by deep-inelastic scattering.

Estimates for the LHC suggest a significant cross section for double-parton collisions into final states with four jets even in the case of charm and bottom heavy-flavour jets: inclusive cross sections of the order of 10 μb and of 1 mb have been foreseen for a double-parton collision process with respectively two $b\bar{b}$ and two $c\bar{c}$ produced [43], whereas the contribution to the same process from single-parton collisions is expected to be one order of magnitude smaller for the case of $c\bar{c}c\bar{c}$ final states, in the low transverse-momentum region. Indeed two $c\bar{c}$ pairs can be produced both by a double parton interaction $(2 \to 2)^2$ and by a single parton interaction $2 \to 4$; an example is shown in Figure 2.4. Moreover, CDF data [39, 40] point to a peculiar pattern of events where the dispersion in the number of partonic interactions is high, i.e., one observes strong fluctuations in the number of produced jets. The large values for the double-parton cross sections at LHC may allow one to identify also triple- and quadruple-parton collision processes.

2.3.1 Double-parton scattering in proton-nucleus

In this section we consider the simplest case of multiparton interaction, the double parton scattering, where two different parton pairs interact independently with a large transverse momentum exchange. Because of the two very different scales which characterize the process, the hard scales and the

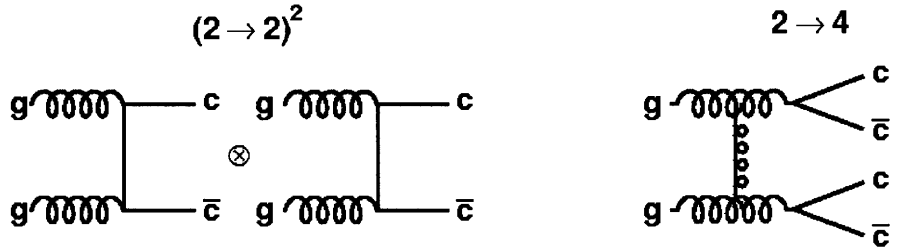

Figure 2.4: *Representation of the two possible processes originating two $c\bar{c}$ couples; two different parton pairs interacting in the same collision event $(2 \to 2)^2$ (left) and a single-parton scattering $2 \to 4$ (right).*

distance between the interactions in transverse space, one expects the double parton cross section to be factorized in a perturbative and in a non-perturbative component. Hence the two parton scatterings add incoherently in the amplitude and the double parton cross section turns out to be expressed as the probability to find the parton pairs in some kinematical configuration multiplied by the probability of the two hard interactions to occur. The two-body parton distribution depends on the parton momentum fractions and on the relative distance between the partons of the pair, and are related linearly to the two-body parton correlations in the hadron structure. The dimensionality of the two-body parton distributions introduces in the double parton collisions cross section a non perturbative scale factor: the *effective cross section*, which is a direct manifestation of the distribution of the interacting parton pairs in transverse space.

Under the simplifying assumption that non-additive corrections to the nuclear parton distributions are negligible, the inclusive double-parton scattering cross section is:

$$\sigma^{\mathrm{D}}_{\mathrm{p-A}} = \frac{\mathrm{m}}{2} \sum_{i,j} \int \Gamma_{\mathrm{p}}(x_i, x_j; r_{ij}) \hat{\sigma}(x_i, x_i') \hat{\sigma}(x_j, x_j') \Gamma_{\mathrm{A}}(x_i', x_j'; r_{ij}) \mathrm{d}x_i \mathrm{d}x_i' \mathrm{d}x_j \mathrm{d}x_j' \mathrm{d}^2 r_{ij} \tag{2.4}$$

The double-parton distributions $\Gamma(x, x'; r)$ for the proton (p) and nucleus (A) depend on the momentum fractions x, x' of the two partons, on their transverse distance r_{ij}, on the parton species i, j, and on the scales of the two interactions (this last dependence is not denoted explicitly). For (in)distinguishable parton processes m equals 1 (2); the 2 at the denominator takes into account the symmetry under i-j exchange. In p-A interactions, the two partons entering $\Gamma_{\mathrm{A}}(x, x'; r)$ originate from either the same or different nucleons in the nucleus; the corresponding cross sections are denoted by σ_1^{D} and σ_2^{D} and their

sum gives the total double-parton cross section $\sigma^{\mathrm{D}}_{\mathrm{p-A}}$. In the limit of small-$x$ parton correlations in fractional momenta are negligible and the two-body parton distribution $\Gamma_{\mathrm{p}}(x_i, x_j; r_{ij})$ can be factorized as the product of the usual single-body PDFs and a function $F(r_{ij})$ representing the parton pair density in transverse space:

$$\Gamma_{\mathrm{p}}(x_i, x_j; r_{ij}) = G(x_i)G(x_j)F(r_{ij})$$

Whit this assumption the inclusive cross section to produce two pairs of heavy quarks in p-p events can be elegantly related to the inclusive cross sections for $Q\bar{Q}$ pair production in p-p collisions [43]. The component of the nuclear double-parton distribution originating from a single nucleon differs from the double-parton scattering cross section σ_{D} in p-p only by the enhanced normalization. This normalization is given by the nuclear thickness function $T(b)$ integrated over impact parameter b,

$$\sigma^{\mathrm{D}}_1 = \sigma_{\mathrm{D}} \int \mathrm{d}^2 b T(b) = A\sigma_{\mathrm{D}} \,. \tag{2.5}$$

For the second case, where two different nucleons are involved in a double-collision process, the corresponding cross section is

$$\sigma^{\mathrm{D}}_2 = \frac{1}{2} \int G_{\mathrm{N}}(x_1, x_2)\hat{\sigma}(x_1, x_1')\hat{\sigma}(x_2, x_2')G_{\mathrm{N}}(x_1')G_{\mathrm{N}}(x_2')\mathrm{d}x_1\mathrm{d}x_1'\mathrm{d}x_2\mathrm{d}x_2' \int \mathrm{d}^2 b T^2(b) \,. \tag{2.6}$$

This equation is derived assuming factorization of the hard interactions in the double-parton scattering process and neglecting the hadron scale as compared to the nuclear scale. The nuclear parton flux, at a given transverse coordinate b, is represented by the product $T(b)G_{\mathrm{N}}(x')$, where $G_{\mathrm{N}}(x')$ is the nuclear parton distribution divided by the atomic mass number A. In Eq. (2.6) the nuclear parton flux is squared since the interaction takes place with two different target nucleons. The difference between the transverse coordinates of the two nuclear target partons, $b + r/2$ and $b - r/2$, is neglected, since the nuclear density does not change in the transverse scale $\langle r \rangle \approx R_{\mathrm{N}} \ll R_{\mathrm{A}}$. With this approximation, the integration over r in Eq. (2.4) involves only Γ_{N}, and the cross section depends on the dimensionless quantity $G_{\mathrm{N}}(x_1, x_2) = \int \mathrm{d}^2 r \Gamma_{\mathrm{N}}(x_1, x_2; r)$. In contrast to σ^{D}_1, no scale factor related to the nucleon transverse size enters the σ^{D}_2 term. The correct dimension for σ^{D}_2 is provided by the nuclear thickness function which gives the normalization to the nuclear parton flux.

Remarkably, in p-A interactions the presence of a large transverse scale, the nuclear radius, allows one to separate the longitudinal- and transverse-correlations effects in the hadron structure. The two components of $\sigma^{\mathrm{A}}_{\mathrm{D}}$,

$\sigma_1^{\rm D}$ and $\sigma_2^{\rm D}$, can be separated on account of their different dependence on the atomic mass number of the target. In the kinematical regime where non-additive contributions to the nuclear parton distributions are negligible, the A-dependence of the two terms does not change with the momentum fractions and with the virtuality scale of the partonic interactions and one has $\sigma_1^{\rm D} \sim A$ and $\sigma_2^{\rm D} \sim A^{1.5}$. Here, the nuclear surface effects lead to a faster dependence of $\int T^2(b) {\rm d}^2b$ on A than the naive expectation $\sim A^{4/3}$. The A-dependence of $\sigma_1^{\rm D}$ is the same as that of the single-scattering inclusive cross section and, in fact, characterizes all parton processes which can be treated in impulse approximation. In particular, this A-dependence allows one to disentangle contributions from $2 \to 4$ parton processes which constitute a background to the double-scattering term. The identical A-dependence of $\sigma_1^{\rm D}$ and other processes such as those producing two large-p_t partons, allow for the separation of $\sigma_1^{\rm D}$ and $\sigma_2^{\rm D}$ even in the kinematical regime in which non-additive effects to the parton distributions are important. Moreover, while non-additive effects to the nuclear parton distributions may reduce the nuclear densities and the cross section by a factor $\simeq 0.7$ at small x, the enhancement factor $A^{1.5}$ of $\sigma_2^{\rm D}$ due to interactions with different target nucleons, is a much larger effect. Hence, the $\sigma_2^{\rm D}$ term may constitute 70% of the cross section $\sigma_{\rm D}^{\rm A}$ in a collision with a heavy nucleus.

The comparison of the two terms, $\sigma_1^{\rm D}$ and $\sigma_2^{\rm D}$, will allow one to determine the average transverse distance between two partons in the hadron structure as a function of their momentum fractions x_1 and x_2. This is a check of the factorization approximation to multiple-parton collisions, which is implicitly assumed in all present considerations. p-A interactions thus provide a novel point of reference, namely the A-dependence, to gain insight into the dynamics of hadronic reaction.

Chapter 3

The ALICE experiment

ALICE is the general-purpose experiment at the LHC, optimized for the study of heavy ions; in this chapter we will describe its various aspects as a detector and as a simulation environment, with particular emphasis on the issues relevant for this thesis work.

At first (Section 3.1) the general characteristics of the detector are described and in particular the barrel subsystem, which covers the central rapidity region and performs tracking and particle identification with the resolutions needed to allow the measurement of hadronic observables. Section 3.2 will describe the means for the simulation of ALICE events (generation, transport and detector response are briefly presented) and for their reconstruction and analysis: the main issues regarding the reconstruction of the tracks (tracking) are explained and the achieved tracking performance is presented. In Section 3.3 we discuss how some beam parameters, affecting the collisions at the LHC, will be relevant for the present study. Finally (Section 4) we present the characteristics of the PC farm exclusively constructed to sustain the processing and storage needs of this simulations.

3.1 The ALICE detector

The ALICE experiment has been in particular aimed at detecting the various observables characterizing the formation of a deconfined medium after a HI collision; as described in Chapter 1, this also implies a comparison with the same observables extracted from collision systems other then nucleus-nucleus, such as proton-proton and proton-nucleus. Thus the ALICE detector, optimized for HI collisions and devoted to pp and pA runs as well, has resulted in a unique design, very different from the other experiments at the LHC, which are optimized for pp collisions ([27], chapter 3). The general layout of

the whole detector is shown in figure 3.1.

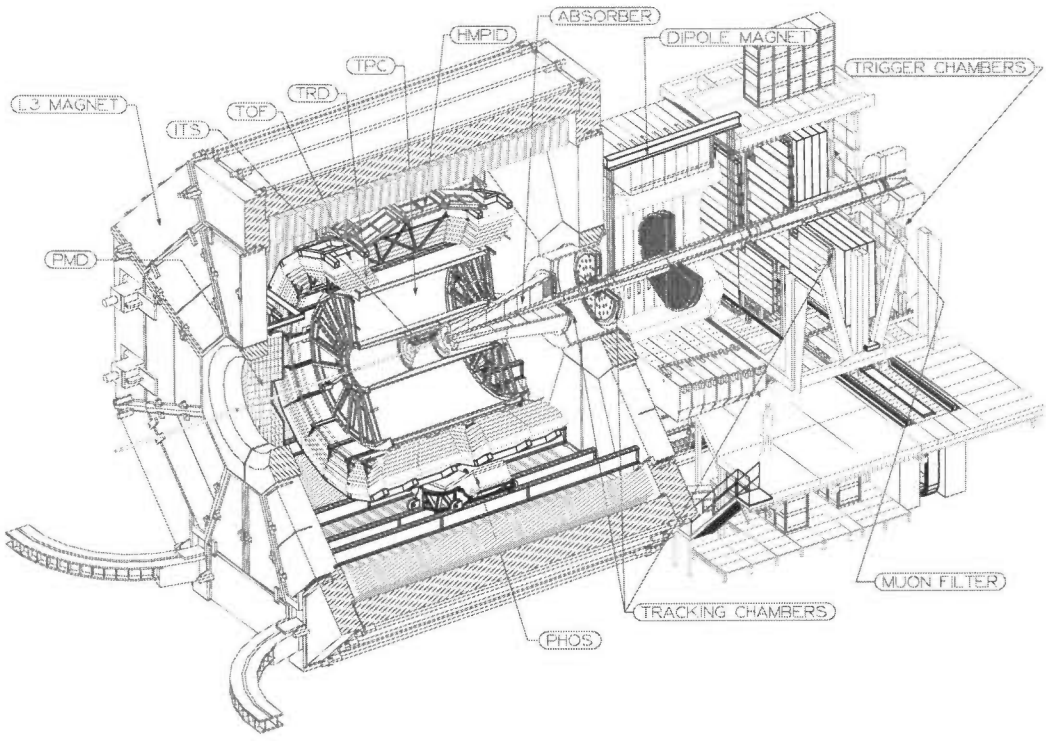

Figure 3.1: *Longitudinal view of the ALICE detector.*

It consists mainly of a central detector, covering the pseudorapidity region η<0.9 (-45^0 < ϕ <+45^0) over the full azimuth and sometimes referred as "central barrel", and the forward muon arm ([]), in the pseudorapidity region -4.0<η<-2.4 . The central detector is embedded in a large solenoidal L3 magnet, providing a weak field (B<0.5T) parallel to the beam direction z, and consists of the following sub-detectors:

- the Inner Tracking System (ITS), made up of six concentric cylindrical layers of high resolution silicon detectors;
- the Time Projection Chamber (TPC), which is the main tracking system of the experiment;
- the Transition Radiation Detector (TRD) for electron identification;
- the Time Of Flight (TOF), a particle identification array;

- the High Momentum Particle IDentifier (HMPID), which is an array of Ring Imaging CHerenkov detectors (RICH counters) optimized for high-momentum inclusive particle identification;
- the PHOton Spectrometer (PHOS), a single-arm electromagnetic calorimeter of high-density crystals.

The central detector is mainly devoted to the detection of hadrons, electrons and photons. The technical design of its sub-detectors and their distance from the colliding beam has been mainly driven by the acceptance requirements, by the multiplicity predictions for lead-lead collisions and by the low interaction rate. A coverage of about two units of rapidity over the full azimuth is required to detect the decay products of low-momentum particles, to allow event-by studies and statistically significant transverse momentum distributions, study of the Υ in the dielectron channel, HBT studies (1.3.1). The predictions for the number of charged particles per unit of rapidity were spanning over a large range (2000-8000) at the time the global geometry of the detector was designed, whereas now, lead by last RHIC results, this range has been sensibly restricted (2500-4000). The chosen detector design, based on the former predictions, will thus ensure a consistent safety margin. Also the low interaction rate plays a primary role in the detector design: at the LHC nominal luminosity of $10^{27}\ cm^2 s^{-1}$ is $\sim$8000 collisions/sec out of which only a few percent have the highest centrality; this has lead to the choice of slow but high-granularity detectors (in particular the TPC and the silicon drift detectors).

The central detector will allow a safe and robust tracking and the particle identification in the central rapidity region (performed by combining the information on energy loss in the tracking detectors, on transition radiation in the TRD, time of flight in the TOF and Cherenkov radiation in the HMPID).

In the forward region the ALICE detector includes the muon spectrometer, a Photon Multiplicity Detector (PMD, $2.3<\eta<3.5$), an ensemble of multiplicity detectors in the region $\eta<5.1$ (FMD), a system of scintillators (V0) and quartz counters (T0), providing fast trigger signals, and the Zero-Degree Calorimeter (ZDC), which consists of neutron and hadron calorimeters placed along the beam at about $90m$ from the IP, to count the spectator nucleons and thus provide a selection over the event centrality (i.e. the impact parameter). The muon spectrometer main aim is the characterization in the $\mu^+\mu^-$ decay channel of the heavy quark vector mesons (J/Ψ, Ψ', Υ, Υ', Υ") spectrum.

The magnetic field strength is a compromise between momentum resolution, acceptance at low-momentum and tracking and trigger efficiency. Momentum resolution increases with the magnetic bending power, whereas

tracking and trigger efficiency decrease with it, in particular for low momentum particles, whose cutoff must be as low as possible (p_t <$100MeV$) in order to detect the products of low-p_t hyperons and to reject the soft conversion and Dalitz pair background from the lepton pair background. For hadronic signals reconstruction the ideal choice would be a 0.2T field; for high-p_t observables the highest available field strength (0.5 T) is the best choice. Since the latter observables are more limited by statistics, ALICE will probably run most of the time at the highest field strength.

The beam pipe is a 0.8 *mm* thick beryllium tube of 59.6 *mm* radius in the region around the interaction point (IP), whereas out of this region it is made of copper or stainless steel.

The data-acquisition (DAQ) system will face the challenge of managing an unprecedented data rate, one order of magnitude bigger than that resulting from the other experiments at the LHC, mainly resulting from the high granularity of its tracking detectors. The final throughput will depend on the online data reduction capability and trigger selectivity, but has been estimated to be around 1.2 GB/s.

3.1.1 The Inner Tracking System

The Inner Tracking System consists of six cylindrical layers of high granularity silicon detectors (Figure 3.2), whose number and position optimizes track finding efficiency and momentum resolution; indeed the main tasks for the ITS are:

1. the reconstruction of primary and secondary vertices with as good a resolution (at least <$100\mu m$) as to allow the efficient detection of hyperons and open charm and open beauty decays;

2. tracking and identification of particles with momentum below 100 MeV/c, which, being strongly bent by the magnetic field, do not reach the TPC;

3. improvement of the momentum resolution for the higher-p_t particles which arrive to or traverse the TPC.

The high particle density expected in heavy ion collisions and the optimization of the spatial resolution have lead to the choice of silicon detectors with the highest granularity and true two-dimensional readout for the four innermost layers.

Layers one and two, at radii 4 and 7 *cm* respectively, are made up of Silicon Pixel Detectors (SPD) having a cell size of $50(r\phi) \times 425(z)$ μm^2 and allowing excellent position resolution in an environment where the track

density may exceed 50 tracks/cm^2. The two intermediate cylindrical layers, with radius 14 and 24 *cm*, are made up of Silicon Drift Detectors (SDD); this choice has been made since they couple a very good multi-track capability to the information on the specific energy loss (with the two-dimensional analog readout).

At larger radii the requirements in terms of granularity are less strict (track densities below one particle per cm^2), therefore double sided Silicon Strip Detectors (SSD) have been selected to build up the outermost couple of layers; the correlation of the pulse height from the two sides will help to resolve the ambiguities resulting from the use of detectors with one dimensional readout. This is a key requirement for an efficient prolongation of the tracks from the TPC to the ITS; indeed the improvement of the momentum measurement of tracks reconstructed in the TPC by means of the ITS is one of the main issues for the whole ALICE tracking capability and one of the main reasons for ALICE to require a vertex detector. The radius of the outermost layer has also been driven by the necessity to efficiently match the tracks with those reconstructed inside the TPC.

The pseudorapidity coverage of the ITS is $|\eta| < 0.9$ for collisions with vertex located within the length of the interaction diamond, i.e. $5.3 < z < 5.3$ cm along the beam direction. The first layer of pixel detectors has a more extended coverage ($|\eta| < 1.98$) to provide, together with the forward multiplicity detectors, a continuous coverage in rapidity for the measurement of charged multiplicity.

Since track momentum and position resolutions for particles with small transverse momenta are dominated by multiple scattering effects, the minimization of the material thickness is an absolute priority in the ITS (as it is for the beam pipe), being the first detector crossed by the particles produced in the collision. In the two innermost layers the pixel sensors and their chips are 200 μm thick, for a total silicon budget of 400 μm per layer. Including also the carbon-fiber supports and the cooling system, the average material per layer traversed by a straight track perpendicular to the beam line corresponds to 1.2% of X_0 . Also the drift and strip layers have a similar material budget, so that the total thickness of the ITS corresponds to $\approx$ 6% of X_0 .

3.1.2 The Time Projection Chamber

The Time Projection Chamber (TPC) is the main tracking detector in ALICE: it provides track finding, charged-particle momentum measurement and particle identification via $\mathrm{d}E/\mathrm{d}x$. A schematic picture of its design layout is given in Fig. 3.3.

The TPC is shaped as a 500 cm long cylinder, with an inner radius of

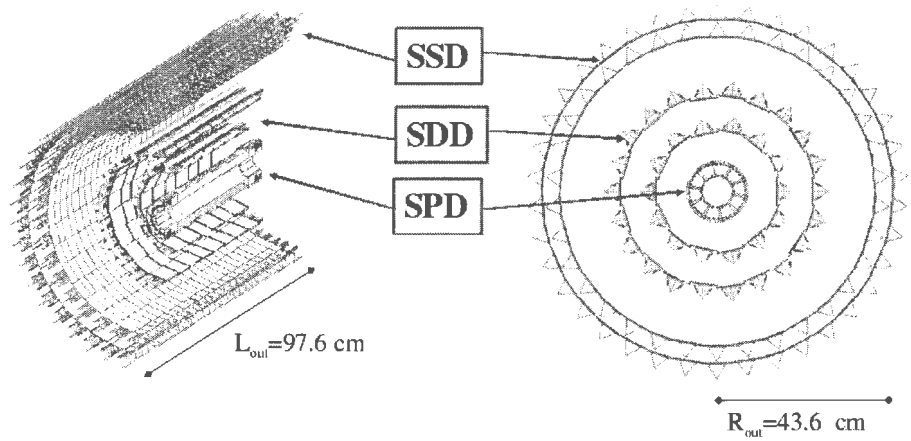

Figure 3.2: *Its layout; from the beam pipe outwards the cylindrical layers are made up by silicon pixel, silicon drift and silicon strip detectors.*

Parameter		Silicon Pixel	Silicon Drift	Silicon Strip
Radius (inner layer)	[cm]	4	14	39
Radius (outer layer)	[cm]	7	24	44
Layer thickness	[% of X_0]	1.24	0.95	0.90
Avg. occup. (inner layer)	[%]	2.1	2.5	4.0
Avg. occup. (outer layer)	[%]	0.6	1.0	3.3
Cell size ($r\phi \times z$)	[$\mu m \times \mu m$]	50 × 425	150 × 300	95 × 40000
Spatial precision ($r\phi \times z$)	[$\mu m \times \mu m$]	12 × 120	38 × 28	20 × 830
Readout channels/module		40960	512	1536
Number of modules		240	260	1698

Table 3.1: *Parameters characterizing the three silicon detector types of the ITS. The occupancy is given w.r.t. the maximum expected particle density in Pb-Pb collisions at the LHC ($dN_{ch}/dy = 8000$).*

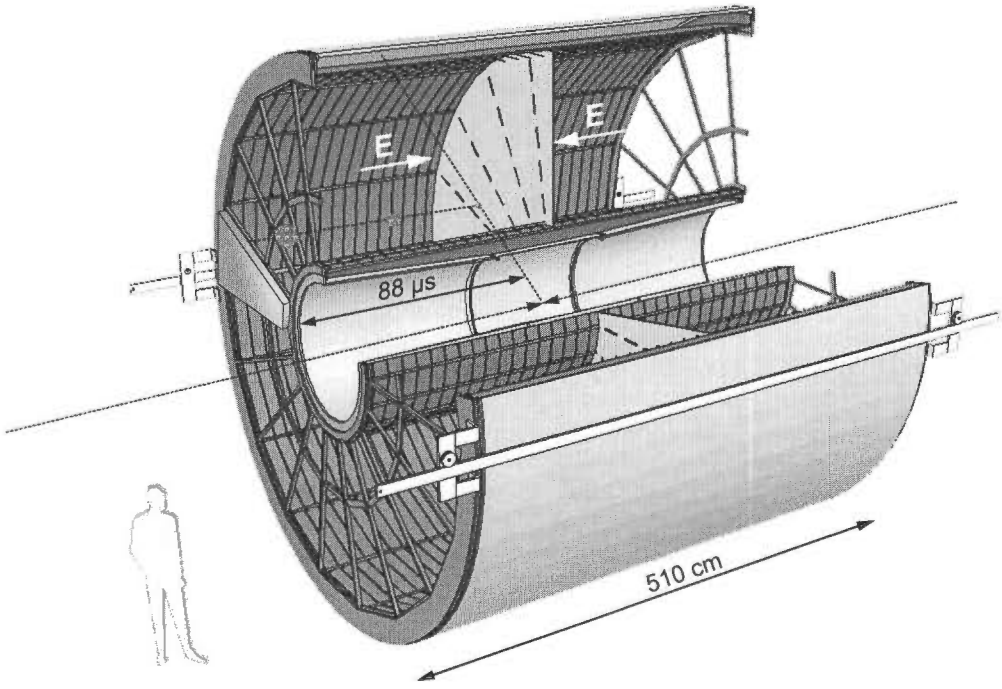

Figure 3.3: *TPC schematic layout.*

84.5 cm, given by the maximum acceptable hit density (0.1 cm^2), and an outer radius of 247 cm, determined by the minimum track length required for a dE/dx resolution better than 10%, necessary for particle identification. The total active length of 500 cm allows the acceptance in the pseudorapidity range η<0.9. The gas mixture Ne/CO_2 (90%Ne, 10%CO_2) is optimized for drift velocity, low electron diffusion and low radiation length. The TPC readout chambers are multi-wire proportional chambers with cathode-pad readout. The readout planes at the two ends of the large drift volume (88 m^3) are azimuthally segmented in 18 sectors, each covering an angle of 20^0 . The non-active region between two adjacent sectors is 2.7 cm wide, implying an azimuthal acceptance of ≈90% for straight tracks originating from the interaction point. The radial thickness of the detector is of 3.5% of X_0 at central rapidity and grows to ≈40% towards the acceptance edges. The final occupancy (fraction of readout pads and time bins above threshold) for the highest predicted multiplicity in lead-lead collisions turned out to range from 40% at the innermost radius to 10% at the outermost radius; this is a critical environment which requires optimal tracking algorithms, whose strategy and performance, tuned for the different collision systems in ALICE, are described later (Section 3.2.3).

3.1.3 Particle Identification

Particle identification (PID) in ALICE will be achieved by combining the information from the two PID-dedicated detectors - the Time Of Flight (TOF) array and the small-area ring imaging Cherenkov detector (HMPID) - with the information from all the detectors of the central barrel.

Charged hadron identification is provided over the full barrel acceptance ($|\eta|$ <0.9) by the combination of $\mathrm{d}E/\mathrm{d}x$ measurement in the four outer layers of the ITS and in the TPC, for momenta up to $\simeq$ 0.5 GeV/c, with a barrel Time of Flight at r = 370 cm, in the range 0.5 < p < 2.5 GeV/c. Electrons are separated from pions for p_t > 1 GeV/c by means of a dedicated Transition Radiation Detector and by exploiting the relativistic rise of the specific energy loss measured in the TPC. A smaller-area ring imaging Cherenkov detector (HMPID), covering about 15% of the acceptance of the ALICE central detectors, allows the separation of hadrons up to higher momenta (π/K up to 3 GeV/c and K/p up to 5 GeV/c). Photons and neutral pions are identified in the small-acceptance electromagnetic calorimeter PHOS. We describe here in detail only the TOF detector, whose parameterized response has entered the simulation work presented in this thesis; its performance and how it has been included for an efficient D^0 reconstruction in p-Pb are presented in Sec. (5.4).

Time of Flight detector

The TOF is shaped as a barrel, with internal and external radii of 370 cm and 399 cm respectively, covering a cylindrical surface of polar acceptance $|\theta - 90^0| < 45^0$; it has a modular structure, 18 modules in $r\phi$ plane × 5 modules along z (for a total active area of $\approx 140m^2$), designed to match the geometry of the TRD detector, inserted between the inner TPC and the TOF itself.

Its task is to provide hadron separation in the momentum range from 0.5 GeV/c, where the $\mathrm{d}E/\mathrm{d}x$ technique is no longer effective, to about 2.5 GeV/c. PID in this momentum range allows the study of the kinematical distributions of the different particle types on an event-by-event basis in heavy ion collisions. Moreover, given the large mass of the charm quark, the decay products of D mesons have typical momenta of the order of 1-2 GeV/c; therefore, the Time of Flight, with K/π separation up to 2.5 GeV/c, is very effective for the reconstruction of exclusive decays of D mesons in hadronic channels.

The time-of-flight is measured using the technology of the Multi-gap Resistive Plate Chambers (MRPC). The RPC is a gaseous detector with resistive electrodes, which quench the streamers so that they do not initiate a

spark break-down. The TOF MRPC design has adopted double stack MRPCs, of size 3.5×2.5 cm^2, aligned in strips, positioned inside modules. The MRPC resolution has been measured to reach 40 ps, with efficiency above 99%. Including the other sources of timing errors, the overall resolution is estimated to be $\approx$ 120 ps. Since it is fundamental to minimize the transversal path of the incident particle through the strip chambers, a special positioning of the strips has been envisaged: their angle with respect to the axis of the cylinder progressively increases from 0^0 (at θ=90^0) up to 45^0 (at θ=45^0). This arrangement makes the median zone of a strip perpendicular to a radius coming from the interaction point. Thanks to an appropriate moulding of the modules' walls, modules can be overlapped in the z direction thus eliminating dead regions along z and reducing from 10% to 5% the dead area fraction over the total barrel area.

3.2 The AliRoot off-line framework

The bulk of the offline activity of the ALICE experiment takes place inside the AliRoot framework ([27], chapter 4). The essential parts of the ALICE off-line activity, as of any other HEP experiment, are the simulation and reconstruction processes which operate in opposite direction extracting the relevant information from the physical collision event to stored data and re-expanding it (upper and lower points in Fig. 3.4). The aim of the simulation is to produce virtual collision events, according to some model, and reproduce the consequent detector response; thus the simulation process comprises the event generation, which passes the particles to some toolkit simulating their propagation in and interaction with the surrounding space and detector materials (transport), in particular the energy released in the detector itself (hits); this information is passed to the algorithms which produce the detector response (digits) and eventually rewrite it in the peculiar format of the magnetic support (raw data). The simulation process is essential for optimizing detector design, trigger issues, beam scheduling, detector components alignment; Furthermore the production of simulated detector response is the basis from which to build up reconstruction algorithms on *a priori*-known events, thus being able to compute their efficiencies and resolutions (processing proceeds counterclockwise on the circle in Fig 3.4; the starting and ending point on the circle can be directly compared when the first half of the circle is not replaced by real data).

The reconstruction chain processes the digital signal sent from the detectors to the storage media (magnetic or optical supports) to rebuild the physical event (or better its relevant parts): it mainly operates to rebuild

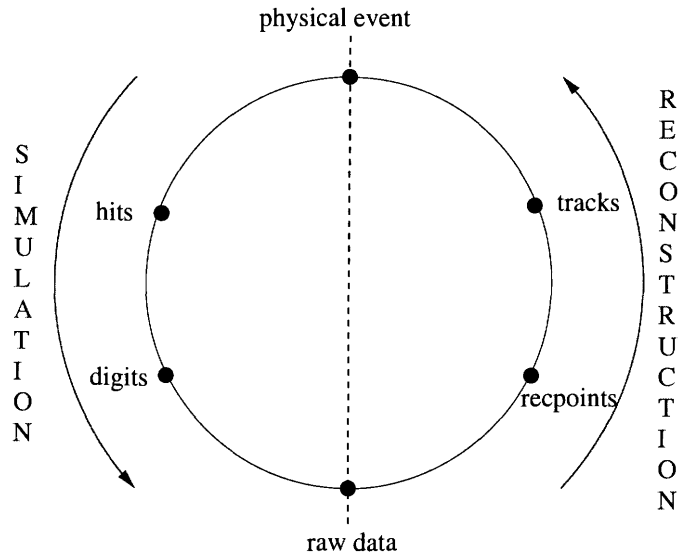

Figure 3.4: *Pictorial representation of the off-line simulation-reconstruction interplay (full explanation in the text).*

the hits (points in the space with associated released energy), identify hits belonging to the same track (tracking), identify their primary and secondary vertices, and analyze this event to extract the information with the highest significance.

3.2.1 Event generators

A handful of event generators exist for simulating heavy-ion collisions at LHC energies. The AliRoot framework provides an interface to several established external generators and embeds a simple event generator based on parameterized η and p_t distributions which can provide a signal-free event with multiplicity as a parameter; this is obtained through the `AliGenerator` base class, which contains some setters (for vertex position, collision parameters, kinematic cuts) for directly producing particles or to tune an external generator through the `TGenerator` abstract ROOT class. The framework provides also tools to assemble events from different event generators (event cocktails), to combine underlying events and signal events both at particle level and at digits level (merging tools) and to introduce particle correlations on top of events (afterburner).

In the following we briefly present the two external event generators used in the present work: HIJING for the generation of background minimum-bias p-Pb events and PYTHIA for signal events, i.e. D^0 hadronic decays at

the energies of LHC p-Pb collisions tuned to reproduce the p_t distributions predicted by NLO perturbative QCD calculations. The details peculiar to this study are described in Section 5.2. Heavy-flavour production is based on the concept of factorization between two distinct phases: the perturbative description of hard production and the hadronization phase, which in PYTHIA is based on the Lund string model []. The hard-production model used in well-established event generators such as PYTHIA and HERVIG is exact only at leading-order (LO), which includes only the pair production processes ($qq \rightarrow Q\bar{Q}$ and $gg \rightarrow Q\bar{Q}$). Heavy-flavour total and differential cross-sections can instead be calculated exactly to next-to-leading order in perturbative QCD. Since these calculations are not suited for being included in event generators, higher-order contributions are instead included in this generators in the parton-shower approach []. This model is not exact at next-to-leading order but it catches some aspects of the multiple-parton-emission phenomenon [].

HIJING

HIJING (Heavy Ion Jet INteraction Generator, [44]) was developed to simulate multiple jets and particle production in pp, pA or AA collisions, combining a QCD-inspired model of jet production with the Lund string model [45] for jet fragmentation. It allows the user to switch on and off parton energy loss ("jet quenching") as well as shadowing; as reviewed in chapter 2, the first effect is responsible for an increase of the particle multiplicity at central rapidities: it is doubled by the use of this option in HIJING. The second effect results in a decrease of the multiplicity at transverse momenta corresponding to low momentum fractions x_{Bj}. In particular the use of HIJING with the jet quenching flag on leads to a charged particle rapidity density at mid-rapidity in Pb-Pb collisions ($dN_{ch}/dy = 6200$) close to the most pessimistic predictions ($dN_{ch}/dy = 8000$), which have already been ruled out by latest extrapolations from recent RHIC observations.

HIJING also includes all sources of background, as decay products from strange particles, apart from secondary interactions. This is an important request for the background generation in order to perform a non-biased analysis, as will be better discussed in Section 5.2.

PYTHIA

In PYTHIA, the processes giving rise to contributions above leading order, see Subsection 2.2.1, like flavour excitation ($qQ \rightarrow qQ$ and $gQ \rightarrow gQ$) and gluon splitting ($g \rightarrow Q\bar{Q}$), are calculated using a massless matrix element. As

a consequence the cross sections for these processes diverge as p_t^{hard} vanishes. These divergences are regularized by putting a lower cut-off on p_t^{hard}. The value of the minimum p_t^{hard} cut has a large influence on the heavy flavour cross section at low p_t, a region of prime interest for ALICE physics and covered by the ALICE acceptance. Our approach has been to tune PYTHIA to reproduce as well as possible the next-to-leading order predictions, obtained with the NLO pQCD code HVQMNR; in particular, activating the MSEL option, a few processes and parameters become tunable, among which the lower p_t^{hard} is the one mostly affecting the final distributions. The details of this tuning are explained in [32], where also the resulting p_t and rapidity distributions are shown, demonstrating that a reasonable agreement has been achieved between the two calculations, despite the fundamental differences between them. Significant discrepancies are present only in the $\Delta\phi$ distribution, i.e. in the angle between the two quarks of the $c\bar{c}$ pairs in the transverse plane.

The PYTHIA event generator was used for the production of $c\bar{c}$ and $b\bar{b}$ pairs in p-Pb collisions at $\sqrt{s_{NN}} = 8.8$ TeV and tuned to reproduce at best the kinematic distributions of the quark pairs. The CTEQ 4L set of parton distribution functions was used, without the modification for nuclear shadowing. Results are shown in Figs. 3.9 and 3.10. The largest difference with the results obtained for the Pb-Pb case is a worse description of the rapidity distribution of charm quarks. This is due to a feature of the parameterizations of the parton distribution functions: most of them, including CTEQ 4, are valid only down to $x = 10^{-5}$; below this value the behaviour depends on the implementation of the specific parameterization but has no physical meaning (e.g. for the CTEQ 4 the gluon density $g(x)$ is kept constant at $g(10^{-5})$). The rapidity range in which the evolution of the parton distribution functions is reliable depends on the c.m.s. energy; for charm production at $\sqrt{s} = 5.5$ TeV (14 TeV) this range is found to be $|y| < 4.3$ ($|y| < 3.4$), using equation (1.8) with $x_1 > 10^{-5}$ and $x_2 > 10^{-5}$. The values of the PYTHIA parameters obtained from the tuning are reported in Appendix B.

3.2.2 Transport and detector response

After particles have been generated close to the interaction point, they are transported outwards subject to the magnetic field and to interactions with the beam-pipe and the detector material (and in case with some gas occupying the beam-pipe). Transport is performed in AliRoot via the interface to GEANT (version 3.21, see [46]), which loads up a detailed geometric description of all the ALICE detector components and propagates particles according to their probabilities of being subject to various physical processes (es-

pecially Coulomb scattering of charged particles on atomic nuclei). GEANT thus produces *hits*, lumps of energy released in points inside the detector, which are then converted in electric signal according to the response properties of the various detector types. This signal is eventually converted into digital signal and formatted according to the front-end electronics output and the Data Acquisition (DAQ) system.

3.2.3 Event reconstruction

Track finding in heavy-ion collisions at the LHC presents a big challenge, due to the extremely high track density foreseen to characterize Pb-Pb collisions. The main step of the reconstruction process are:

- cluster finding;
- tracking;
- vertex reconstruction;

The second and third items are correlated, since a good knowledge of the primary vertex position is a good guide for track finding algorithms and, conversely, tracks can be used to extract the spatial position of the primary vertex.

Cluster finding

During cluster finding, the information given by the detector electronics (digits) is converted to space points, interpreted as (a) the crossing points between the tracks and the centers of the pad rows in the readout chambers, in the case of the TPC, and (b) the crossing points between the tracks and the silicon sensitive volumes, in the case of the ITS. Another important piece of information provided by the cluster finder, is the estimate of the errors of the reconstructed space points. At present, a procedure for parallel clustering and tracking in the TPC is being tested. In the high-multiplicity scenario of Pb-Pb collisions clusters from different tracks may overlap and a preliminary knowledge of the track parameters is very helpful in the cluster deconvolution. The possibility to use a fast simulation of the detector response is implemented for many sub-systems of ALICE. The clusters are obtained directly from the hits via a parameterization of the response, in terms of efficiency and spatial resolution. The dramatic reduction in computing time (e.g. a factor $\simeq 25$ in the case of the ITS) allows the use of very

high statistics in simulation studies. The clusters obtained via the fast simulation are called *fast points*, while those obtained from the detailed detector response are called *slow points*.

Tracking

Due to the expected charged particle multiplicity, track finding in ALICE is a very challenging task. In the most pessimistic case, the occupancy (defined as the ratio of the number of read-out channels over threshold to the total number of channels) in the inner part of the TPC may reach 40%. The track finding procedure developed for the barrel (ITS, TPC, TRD, TOF) is based on the Kalman filtering algorithm [81], widely used in high-energy physics experiments. The Kalman filter is a method for simultaneous track recognition and reconstruction (or, in other words, track finding and fitting) and its main property is that, being a local method, at any given point along the track it provides the optimal estimate of the track geometrical parameters at that point. For this reason it is a natural way to find the extrapolation of a track from a detector to another (for example from the TPC to the ITS or TRD). As we will explain, in the Kalman filter energy loss and multiple scattering are accounted for in a direct and simple way. The complete chain of track reconstruction in the ALICE barrel foresees the following steps: (a) track finding in the TPC, inward (i.e. from the outer to the inner part); (b) matching to the ITS outer layer and track finding inward down to the innermost pixel layer; (c) back-propagation and refit of the track outward in ITS and TPC, up to the outer radius of the TPC; (d) matching to the TRD and track finding (outward) in the TRD; (e) matching to the TOF detector, for PID. Here we describe only steps (a) and (b), since this is the part of the chain which was employed in the studies performed for this work. In the Kalman filter procedure, as implemented in ALICE, a track in the magnetic field of the barrel is locally (i.e. at a certain radial position in the barrel) parameterized as an helix, identified by a state vector of 5 parameters. Two parameters describe the track geometry in the beam direction (z) and three in the plane transverse to the beam (also referred to as bending plane). The description of the track state is completed by the 5×5 covariance matrix of the parameters, which, at any given point, contains the best estimate of the errors on the parameters and of their correlations. In the TPC tracking, the procedure starts from the searching of track seeds in the outermost pad rows of the detector, where the occupancy is lower. All pairs of points, the first on the outermost pad row and the second on the pad row which is n rows closer to the interaction point, are considered. For each pair, using the two points and the primary vertex position, a first estimate of the state vector

at the outermost pad row is obtained. Then, track points in the next n rows are searched, and, if at least n/2 points are found, the candidate is saved as a track seed. Subsequently, a second seed-finding step is performed using another pair of rows. At this point the Kalman filter through the TPC starts, beginning with the tracks with lower curvature (i.e. higher p_t) that are found more easily, because the effect of multiple scattering is inversely proportional to the track momentum. The algorithm proceeds with an iteration of three steps:

1. Prediction: given the state j 1 of the track at a certain layer, a prediction of the state j is obtained by propagating the track-helix to the next layer. In this prolongation the track curvature is modified to take into account the energy loss and the covariance matrix is updated according to the multiple scattering in the material encountered by the track.

2. Filtering: after the extrapolation to the state j, all clusters whose coordinates are inside a suitable 'road' are considered, the road being defined by the track covariance matrix and by the spatial resolution of the present detector layer. For each cluster the state vector is updated and a χ^2 -increment is calculated. Then, all the possible prolongations are 'filtered' and the cluster that gives the minimum χ^2 -increment is assigned to the track, provided that the increment is lower than a given χ^2 max .

3. Update: finally the state j of the track is updated using the information of the assigned cluster.

In the ITS implementation, the Kalman procedure was modified toward a more global approach. The tracks found in the TPC are used as seeds, again beginning with higher-p_t tracks. In order to find the prolongation of a TPC track inside the ITS, for each seed all clusters on the outer ITS layer which are located in the fiducial road are considered. For each of them a new candidate track is defined and propagated to the next layer, without applying any filtering. In this way, a track-tree with many candidates is built from a single TPC track, and only when the inner pixel layer is reached the filtering is applied and the candidate with the lowest χ^2 per assigned cluster is selected. The assigned clusters are 'removed' and the next TPC track is considered. In this way the finding of the low-p t tracks is facilitated, since all the clusters from the previously found tracks are not considered. Two track finding steps are used in the ITS: the first with a constraint on the position of the primary vertex, measured by the pixel layers (see Chapter 5), to increase the efficiency for the tracks originating from the primary vertex (primary

tracks); in the second step this constraint is removed in order to allow the finding of tracks coming from displaced vertices (secondary tracks, e.g. decay products of strange particles). Decay products of charm (and beauty) mesons can be considered as primary, from the point of view of track finding, since their displacement is usually lower than 1 mm. Afterwords, all found tracks are re-fitted without vertex constraint, in order to get an unbiased estimate of the distance from the interaction point. In the next sections we shall present the relevant performance parameters of the track reconstruction in the TPC and in TPCITS. The two extremes of the multiplicity scale are considered: central PbPb (dN_{ch}/dy = 6000, HIJING) and pp collisions (dN_{ch}/dy = 6, PYTHIA). The value of the magnetic field is 0.4 Tesla.

Tracking efficiency and momentum resolution in p-Pb

Only a fraction of the primary tracks, originated close to the interaction point, reaches the ITS and the TPC detectors, whose inner radius is ≈90 cm; only a sub-fraction of them will be reconstructed, due to several reason explained later. We are now interested in the overall efficiency of primary particles tracking of the TPC and the ITS, defined as the fraction of primary tracks generated in the barrel acceptance, $|\eta|<0.9$, reconstructed by the detector under consideration. The pseudorapidity cut must be applied not only to the generated tracks (denominator) but also to the reconstructed tracks (numerator), since a fraction of them has been generated outside this pseudorapidity window but has later entered the barrel acceptance after Coulomb scatterings. Tracking efficiency for kaons and pions for the TPC sub-detector alone (figure 3.2.3, left) and for the TPC+ITS detector subsystem (figure 3.2.3, right) are presented. This figures show also separately the efficiencies for kaons and pions; the large difference between their efficiencies at low momenta is due to their mean decay lengths, which for kaons is 7.5 m $\cdot p$(GeV/c), much lower than for pions (55.7 m $\cdot p$(GeV/c)). At high transverse momenta (p_t>10 GeV/c) the tracks are straight and the inefficiency of ∼10% is almost due only to the non-active regions of the TPC (separation between different sectors) which indeed cover ∼10% of the barrel angular acceptance. The ITS efficiency is considerably affected by the required minimum number of clusters assigned in it; 6 clusters where required in the ITS (one per ITS layer). The resulting average ITS+TPC efficiency is higher for signal pions and kaons(0.70 and 0.52) than for background pions and kaons (0.54 and 0.38), due to the fact that the PYTHIA p_t-distributions for the signal are harder then the HIJING p_t-distributions for the background, as shown in figure 5.4.

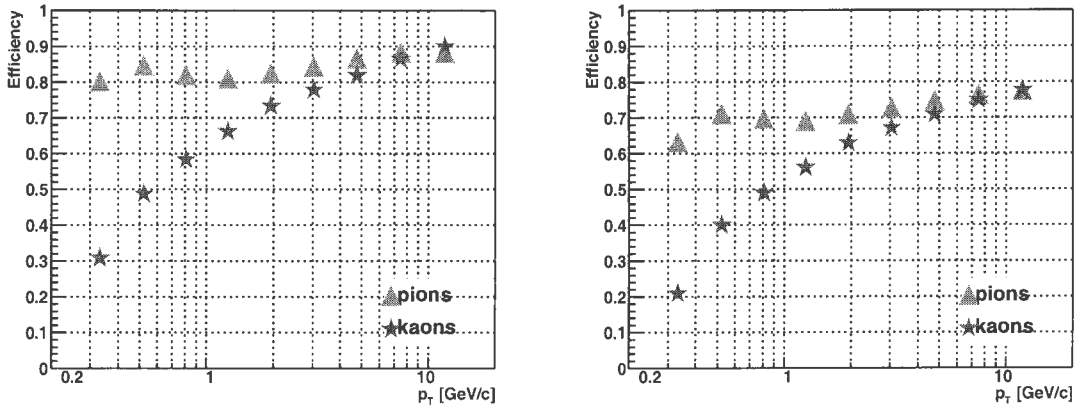

Figure 3.5: *Tracking efficiency in the TPC (left) and TPC+ITS subsystem (right).*

Momentum resolution in p-Pb

3.3 LHC beam parameters

The characteristics of the particle beams at the ALICE intersection point (IP) are a key experimental issue on which depends also the feasibility study presented in Chapter 5; we will show in the following subsection how the beam parameters determine the luminosity and thus the dimensions of the interaction region, the region in space that contains all the possible collision vertices. Depending on the beam parameters it will be possible to have a priori knowledge of the primary vertex position. We will then consider the specific case of p-Pb (Section 3.3.1) running.

3.3.1 Luminosity, beam size, interaction region in p-Pb collisions

The event rate $\mathcal{R}$ in a collider is proportional to the interaction cross-section σ_{int} and the factor of proportionality is called luminosity ($\mathcal{L}$):

$$\mathcal{R} = \mathcal{L}\sigma_{int}$$

In order to have a high event rate one would want a high luminosity; on the other hand the accelerator and the upper limit for the detector occupancy constrain the maximum allowed luminosity. For ALICE, in the case of Pb-Pb

events the limitations of the detector and of the machine coincide, while in the case of pp events the maximum event rate is determined by the detector and the machine parameters have to be tuned in order not to exceed this limit.

Let us consider two intersecting bunches, labeled 1 and 2. To a good approximation, the particles in each of them will be distributed according to Gaussians in the three perpendicular directions:

$$N_i(x,y,z) = N_i G(x,\bar{x}_i;\sigma_{x,i})G(y,\bar{y}_i,\sigma_{y,i})G(z,\bar{z}_i,\sigma_{z,i}) \qquad i=1,2$$

where N_i is the total number of particles in the bunch i and $G(q,\bar{q},\sigma_q)$ is the Gaussian centered in $\bar{q}$ with variance σ_q: $G(q,\bar{q},\sigma_q) = \frac{1}{\sqrt{2\pi}\sigma_q}\exp -\frac{(q-\bar{q})^2}{2\sigma_q^2}$ for $q = x,y,z$. If f is the revolution frequency and N_b is the number of bunches, the luminosity is obtained as:

$$\mathcal{L} = fN_b \times \int dxdydzN_1(x,y,z)N_2(x,y,z)$$

Here, the integration along the beam direction, z, gives 1, since the two particle bunches cross each other and, therefore, their distributions along z are equivalent to delta functions from the point of view of the interaction probability. At the LHC the bunches in the two beams have the same number of particles (N) and the same dispersions; moreover the dispersion is the same for the two directions transverse to the beam axis ($\sigma_x = \sigma_y = \sigma_{x,y}$). Thus:

$$\mathcal{L} = fN_b\frac{N^2}{4\pi\sigma_{x,y}^2}\exp\frac{d^2}{4\sigma_{x,y}^2}$$

where $d^2 = (\Delta\bar{x})^2 + (\Delta\bar{y})^2$ is the square of the distance between the centers of the two beams. Normally, the two beams are centered and $d = 0$. On the other hand, the interaction region is defined as the convolution of the two particle distributions in the two intersecting bunches: the interaction vertex lies in a 'diamond' with 'dimensions'

$$\sigma_q^{vertex} = \sigma_q/\sqrt{2} \qquad q = x,y,z$$

that do not depend on the value of d, if the distributions are Gaussians. The size of the bunches at the IP depends on the transverse emittance (a beam quality parameter) and on the value of the amplitude function β at the IP, indicated as β^*, which is determined by the accelerator magnets configuration. We have:

$$\sigma_q = \sqrt{\frac{\epsilon_q\beta^*}{\pi}} \qquad q = x,y,z$$

From the last three equations we see that the luminosity can be decreased locally (i.e. only at the ALICE IP) by increasing β^*, but this increases the transverse size of the interaction region. In Table 4.3 we report the LHC machine nominal parameters at the ALICE IP for pp and Pb-Pb runs [33]. We will discuss them in the next sections.

Optimization of luminosity and life-time leads to high-intensity proton beams and low-intensity lead beams with a life-time of $\approx$10 hours.
$\mathcal{L}_{max} = 5.8 \times 10^{29}$ at 200 kHz interaction rate

Proton-lead collisions at the LHC are possible because there are two independent RF systems for accelerating the two opposite beams.

Along the z direction, the interaction point is distributed according to a Gaussian with a dispersion of 5.3 cm and the ALICE interaction trigger selects the events with vertex located in the fiducial region $5.3 < z < 5.3$ cm. Clearly, the position of the vertex in z has to be reconstructed on an event-by-event basis. This task is achieved exploiting the correlation between clusters in the two silicon pixel layers of the ITS ([47], [48]); this method will be briefly described in SubSection 5.3.1.

Chapter 4

Tests on a farm for ALICE

In this section we present the farm of PCs installed in Trieste and its aspects relevant for this thesis work and for applications inside the ALICE collaboration. Indeed it has allowed not only to run locally the jobs needed in the whole simulation process described in the previous section, but also to conduct some test at hardware and software level.

We discuss here the choices made to optimize the performances of the farm (Sec. 4.1), a few software solutions of interest for the use of the AliRoot software in a distributed environment and in view of a future participation of this farm as a TIER element of the AliEn grid (Sec. 4.2); finally (Sec: 4.3) some benchmarking results are presented.

4.1 General features

The ALICE experiment will require a huge amount of computing and storing resources which need to be distributed over a wide grid area around the world. This unprecedented requirements have raised the need for an environment of shared disk space and shared processing power, the GRID. There are at present some working implementations, which are leading the state-of-the-art in this field, among which the LCG project ([49]), coordinating the efforts of the various experiments based at the LHC accelerator, and AliEn, the GRID prototype created by the Alice Offline Group. These are hierarchical structures coordinating the resources shared by scientific computing centers into a single virtual computing organization.

The employment of the farm ([50]) in the AliEn [51] environment requires a high uptime which, in turn, demands strong security and a "graceful degradation" ability, i.e. fault of a part should not cause fault of other parts. Solutions like the channel bonding technique and the packet filtering (4.2.3)

have been studied in this perspective.

In order to ensure a highly performing farm, the following criteria have been adopted: use of state-of-the-art computer components and latest software releases (4.1.1); the network architecture implementing the channel bonding, where each computer is equipped with two network cards (4.1.2).

A "Beowulf philosophy" [52] has been adopted, which employs off-the-shelf components, e.g. low-cost Ethernet cards instead of expensive Gigabit cards, and open-source software, e.g. Linux as operating system. Special care has been taken to study innovative solutions for the ALICE community, which can enhance the computing performances while keeping low the overall cost of the farm. The channel bonding technique (4.1.3), which improves the bandwidth within the farm, goes in this direction. In addition, the Mosix kernel extension and the distributed file system MFS (4.2.1), which favour the distribution of the jobs in the farm, have been studied.

In the following we describe the general features of the farm, discuss software-related choices and finally show the results of the performance tests and draw the conclusions.

4.1.1 Hardware and software choices

The farm ([53]) consists of 19 assembled dual-processor PCs and of a disk server. Fourteen PCs are equipped with two Intel Pentium III processors at 1000 MHz and a 512 MB ECC-registered memory chip[1].

EIDE disks of 40 GBytes each add to the farm 500 GBytes of mass storage when a distributed file system is implemented. One of the PCs acts as the server and provides access to/from the external world, using the *iptables* directives to filter outgoing and incoming packets. The server contains some additional accessories such as a DVD burner for backup purposes.

The disk server is a dual-processor PC with 20 EIDE hard disks of 80 GBytes, for a total amount of mass storage of 1.6 TBytes. The disk server has a proprietary firmware and works in a RAID 5 configuration, which provides parity check and data striping, i.e. spreads out blocks of each file across multiple disks.

All PCs have operated under RedHat Linux, kernel 2.4.19; an official

[1]ECC and "registered" memory are both features geared toward stability rather than performance. ECC (Error Checking & Control), created after Parity RAM was the norm, not only checks the bytes, but adds an extra bit to correct most errors, where Parity RAM would generally halt the system before further errors could occur.

Registered RAM contains a "register" to aid in ensuring the data is being handled correctly, delaying all data from being transferred to the module for one clock cycle.

CERN distribution has recently been developed[2] in order to avoid any distribution-dependent issue; it is therefore our intention to switch to it in the nearest future. The RedHat kernel has been patched with the Mosix extension to allow the dynamic migration of jobs. ROOT [54] and AliRoot [55] have been installed on the disk server and exported via NFS to all the nodes of the farm. They run both ROOT and AliRoot via the network. Both ROOT and the C-programs linked with the ROOT libraries can be dynamically migrated by Mosix, which however fails to migrate AliRoot. This failure does not hamper the possibility of using Mosix as workload manager in a farm for the ALICE's computing: in fact, each job can still be migrated manually invoking the proper Mosix command (`mosrun`), but defeats the main feature (automigration) of Mosix.

Five dual-processor PCs configured with AMD Athlon XP 2400+ processors at 2000 MHz have been used to build an independent farm, with the same architecture but without the channel bonding technique[3]. For them, Gentoo Linux, kernel 2.4.20, replaced RedHat Linux while leaving the Mosix patch unchanged. The goal was threefold: 1. testing the features of Gentoo; 2. installing and running ROOT and AliRoot under Gentoo Linux; 3. checking if the AliRoot migration failure was due to the network or to the operating system or to the processors. It turned out that none of these elements are responsible for the incompatibility between Mosix and AliRoot. Details of this study are reported later in this article.

4.1.2 Network architecture

The overall architecture of the farm is shown in Figure 1. In order to implement the channel bonding technique, each computer has been configured with two network cards, each connected to an independent switch. The disk server is connected to the farm via Gigabit connections. This was done to provide an higher bandwidth from/to the disk server which is the main mass storage element in the farm.

The server has a third network card for connecting to the external world and is responsible for filtering incoming and outgoing packets. Packet Filtering is the type of firewall built in the Linux kernel. A filtering firewall works at the network level, allowing data to leave the system only if they are in accordance with the firewall's rules. As packets arrive they are filtered by

[2]Scientific Linux CERN 3 is a Linux distribution build within the framework of Scientific Linux which in turn is rebuilt from freely available Red Hat Enterprise Linux 3 product sources

[3]The farm was installed in year 2001; the additional five nodes were added in year 2003.

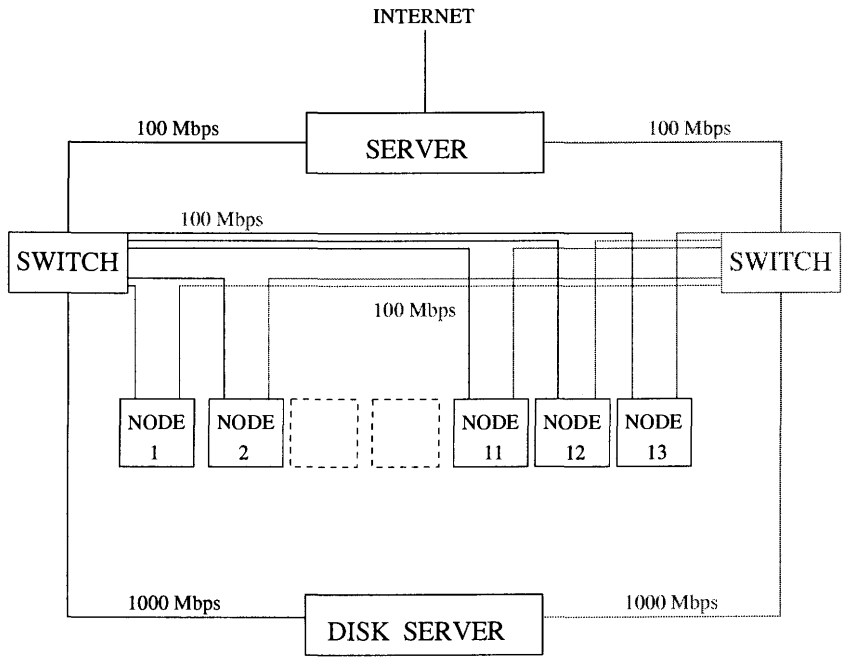

Figure 4.1: *Farm network architecture.*

their type, connection state, source address, destination address, and port information contained in each packet.

The server serves also as the interface to Grid, the world-wide framework for distributing computing and mass storage. For this purpose, the AliEn package [51] has been installed. AliEn is used by the ALICE collaboration as the interface to Grid.

The choice of the software packages relies on the idea of leaving the computers as light as possible, freeing the CPU and the memory resources for calculation tasks. Standard packages, like the X server, which provides the graphical interface to the user, have not been installed on the computers. The Gentoo Linux distribution is useful in this regard since it provides a minimal configuration of the operating system.

4.1.3 The channel bonding technique

The channel bonding [56] requires the installation of a second network card on all the computers of the farm. The second card is connected to a separate switch, providing high availability within the farm, i.e. low risk of loss of connection due to a failure of a card or a breakdown of a switch. Adding a second network card improves also the bandwidth within the farm. The

only recommendation when implementing the channel bonding is that all the computers must use both cards. Communication between a channel-bonded PC and a non-channel-bonded PC is very slow if not impossible.

The channel bonding requires a patched kernel in order to have the adequate software support. The most recent kernels can be compiled with the channel bonding support setting a flag during the compilation stage. In order to configure the network interface, the `ifenslave` command replaces the usual Linux command (`ifconfig`).

4.2 Software solutions

In order to use all the disks for the mass storage, a distributed file system can be used. Out of the several choices available on the market, NFS, MFS and PVFS have been considered (4.2.1).
In view of using the farm within the Grid environment, an efficient workload manager must be provided. It serves for balancing job execution between all the computers in the farm. In place of the common choices, like OpenPBS, Mosix has been implemented and studied (4.2.2).
Finally, security and maintenance issues have been addressed in order to improve the uptime of the farm (4.2.3).

4.2.1 NFS, MFS and other file systems

A local file system is not the best choice for a Mosix farm designed for distributing computing. In fact a migrated job requesting an I/O operation is more likely to do it on the machine where it is currently running, instead of migrating back to the machine where it was run first. Hence network and distributed file systems, like NFS, MFS and PVFS, become very useful, providing a more transparent and efficient management of files and directories across the farm. For them, network overhead, disk I/O bandwidth, farm scalability and availability are the main problems to be faced.

The Network File System (NFS) [57] has been developed to allow machines to mount a disk partition of a remote machine as if it were on a local hard drive. It allows all the computers in the farm to mount the disks of the disk server. The disadvantage is that the local disk on each computer is left unused since it cannot be mounted on all the computers. Moreover, a network overhead is generated once a heavy I/O demand is produced by many jobs distributed across the farm. Another problem is that many jobs requiring writing access to the EIDE disks on the disk server can saturate the disk I/O bandwidth (~60 MBps), which would become the bottleneck

for data transfer if compared with the Gigabit throughput to the disk server. This limits also the scalability of the farm, i.e. the possibility of adding nodes to the farm without decreasing the performances.

The Mosix File System (MFS) [58] has been designed to meet the needs of the Mosix users, especially in case of high I/O demand. MFS is fast because it operates at a lower level within the kernel than do other network file systems. Benchmarks completed by the Mosix development team suggest data transfer rates for MFS to be ~150% of the transfer rates for NFS.

Both NFS and MFS have been implemented, giving encouraging results. Presently, NFS is the file system in use since Mosix has been disabled due to its incompatibility with AliRoot. Future improvements foresee the implementation of the Parallel Virtual File System (PVFS) [59]. PVFS allows a physical distribution of the data across the disks on different nodes of the farm. It can be mounted on all the nodes in the same directory, allowing all the nodes to access files through the same directory scheme. In order to provide high-performance access to the data, PVFS spreads the data out across multiple nodes in the farm. By spreading the data across multiple I/O nodes, the applications have multiple paths to the data through the network and multiple disks on which the data is stored. This eliminates single bottlenecks in the I/O path, thus increasing the total potential bandwidth for multiple clients. The drawback, in this case, is the absence of redundancy, that is, if an I/O node fails, PVFS accesses requiring that node will also fail, causing a decrease in the availability of the farm. However, PVFS runs on top of RAID file systems, which can provide at least some measure of redundancy at the disk level. In our case, the use of PVFS has been complicated by the simultaneous presence of a distributed mass storage and the disk server. Furthermore the scalability is limited by the network overhead which arises from the management of a distributed file system.

4.2.2 Mosix as an alternative workload manager

Most of the analysis of the ALICE events will be performed across the many PC farms used by the ALICE community. Therefore, it is of primary interest to test the ability of different workload managers to optimize the farm performances. For this reason the Mosix package has been evaluated and compared to the long-established load-balancing programs, like OpenPBS [60] and Condor.

Mosix [58] is a Linux kernel extension (and a related set of user programs) that performs process migration within the farm. The migration is transparent and automatic and follows adaptive algorithms to load-balance across uneven available resources, continuously migrating processes to faster or less

busy nodes.

Although Mosix is very efficient for handling CPU-bound processes, it is not so good when handling I/O demanding jobs. The reason is that I/O occurs on the home node, i.e. the computer where the job was launched, and therefore a migrated process must "phone home" to perform I/O, eventually slowing down considerably its execution. In order to improve Mosix performances the Direct File-System Access (DFSA) has been designed: it allows migrated jobs to perform most of their I/O and file system operations directly on the remote node, where the process is currently running. DFSA has been implemented to work with the MFS file system.
Running at kernel level, Mosix turns out to be more efficient as workload manager than other packages, like OpenPBS or Condor, but requires a queue manager running on top of it, to decide which jobs are to be run on the farm at a given time.

4.2.3 Security and maintenance concerns

A few peculiar choices have been made to keep the farm as secure as possible. Among these the most important is the packet filtering. Based on `netfilter/iptables` [61], the latest Linux firewall code, it allows only certain types of traffic, restricting the access to the farm and checking if an exception occurs. Only the server is connected to the Internet and has an IP address. All the other computers in the farm have a private IP address recognized only within the farm. In order for them to be connected to/from the Internet, `netfilter/iptables` provides a feature called *Source and Destination Network Address Translation* (SNAT and DNAT). With SNAT, all the private addresses are aliased to a collective IP address which is used to connect to the Internet. With DNAT, a remote computer, using the collective address to connect to the farm, is randomly redirected to a computer within the farm.

In order to make maintenance tasks easier, Gentoo Linux ([62]) has replaced RedHat Linux. This new Linux distribution can be easily customized and updated. Installing and optimizing the latest software packages is straightforward thanks to the Portage distribution system.

4.3 Performance tests

`NetPIPE` (Subsection 4.3.1) has been used to test the network solutions. It proves the improvement to the bandwidth due to the channel bonding technique. `Memperf` (4.3.2) has been employed to test the rate at which a data

block transfer from/to memory is performed.

Concerning Mosix, several unsuccessful attempts have been made to run AliRoot with both a Mosix-enhanced RedHat- and a Mosix-enhanced Gentoo kernel (Subsection 4.3.3). A low-level debugging has been carried out to understand the incompatibility between Mosix and AliRoot. This debug however could not help to solve the problem. Finally, a comparison between RedHat and Gentoo has been done with regard to the AliRoot execution rate (Subsection 4.3.4).

4.3.1 Network

Significant parameters to evaluate the network performances are the following: 1. the *throughput*, i.e. the network bandwidth as a function of the transmitted packet size; 2. the *saturation level*, i.e. the block-size that maximizes the bandwidth; 3. the *latency*, i.e. the time it takes for the smallest packet to arrive. It must be noted that AliRoot copies its buffer to disk at time intervals varying from one tenth of a second to a few seconds. The I/O buffer size spans more than three orders of magnitude, ranging from about 0.1 KB to 0.5 MB. Therefore, the throughput turns out to be an important parameter to evaluate how AliRoot behaves when run in a distributed way. The results are displayed in Figure 4.2. They have been obtained by means of

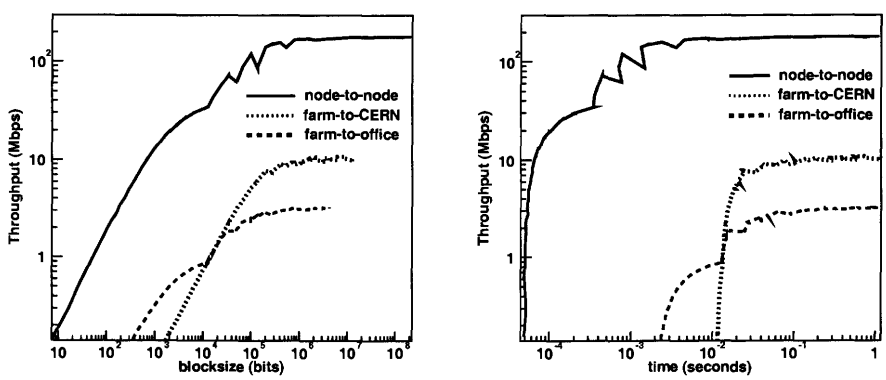

Figure 4.2: *Throughput (left) and signature (right) graphs.*

the NetPIPE (Network Protocol Independent Performance Evaluator) tool [63], which is based on the most common TCP/IP network performance evaluator tools, `ttcp` and `netperf`. The left part of Figure 4.2 shows the measured throughput (in MB per second) versus the transfer block size (in bits) for a node-to-node connection within the farm (solid curve) and for

a farm-to-CERN connection (dotted curve). The dashed curve is given for comparison and refers to the connection between the farm and the author's workplace, located in a separate building. The lower throughput obtained for smaller block size transfers is related to the time spent in establishing the connection. From the graph one can also deduce the maximum bandwidth and the saturation level, e.g. 10 Mbps and $\sim 2 \cdot 10^5$ bits, respectively, for the connection to CERN. The right graph in Figure 4.2 plots the so called signature, i.e. the throughput as a function of the elapsed time. The latency is the intercept of the curves with the x-axis, e.g. $\sim 10^{-2}$ seconds for the connection to CERN. The irregular behaviour of the curves is due to normal, although not desirable, effects of the network parameter settings, like socket buffer sizes and thresholds, and of the network driver tunings [63].
The bandwidth enhancement obtained with the channel bonding is shown in Figure 4.3. With respect to an Ethernet connection, the channel bonding doubles the throughput within the farm, hence representing an optimal solution to improve network performances at a smaller cost than that of the more expensive Gigabit connections.

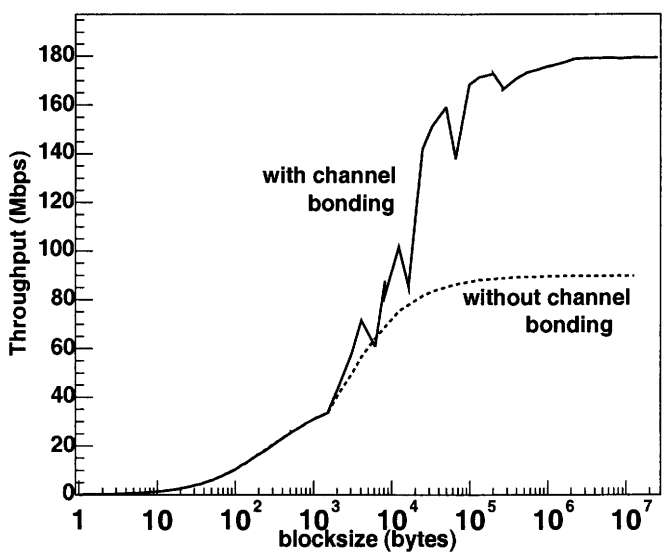

Figure 4.3: Channel bonding throughput enhancement.

4.3.2 Memory

Depending on the requirements of the CPU usage and data transfer from/to memory of an AliRoot job, execution and memory transfer times can become comparable and memory bandwidth obtainable by user codes could become a limiting factor in the performance of the farm. As a benchmark for testing the memory bandwidth, `memperf` [64] has been used. It provides a measurement of the memory bandwidth as a function of the block size. The resulting graph is shown in Figure 4.4. Clearly evident is the drop at a packet size of 128 KB. The two curves in the figure correspond to two different tests performed by `memperf` [64].

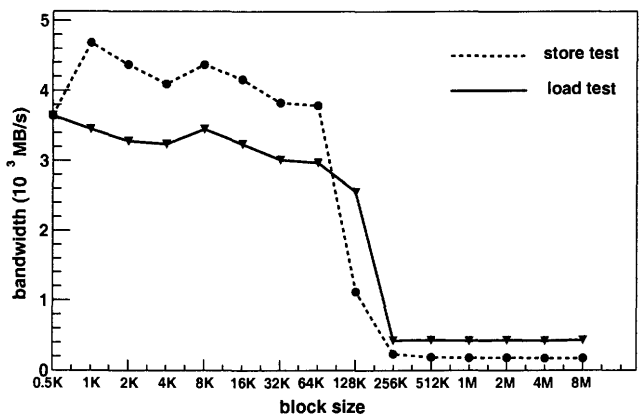

Figure 4.4: *`Memperf` gives a measurement of the memory bandwidth as a function of the block size.*

4.3.3 Mosix

Mosix and its open-source version OpenMosix [65] have been tested by running time consuming jobs, with and without I/O, inside and outside the ROOT and AliRoot framework. While programs compiled with the ROOT libraries succeeded to be migrated by Mosix even if they did I/O operations, Mosix failed to migrate AliRoot. In the latter case, a loss of connection was observed between the home node, i.e. the computer in the farm where AliRoot was launched, and the host node, i.e. the computer where AliRoot migrated. It turned out that the job's PID was no longer accessible by the home node, causing `ps` (the unix command which provides the list of processes and their PID's) to give no output and `top` (the unix command which

lists in real time the most CPU-intensive jobs) to freeze out the whole node. Same behaviour showed `mtop`, the analogous command provided by Mosix. MFS could not be unmounted.
In order to solve this problem, several attempts have been made:

1. ROOT and AliRoot have been recompiled without thread support, so that `libpthread` did no longer appear in the list of linked libraries. This attempt followed a private communication with the Mosix authors, suggesting to remove all threads, disliked by all versions of Mosix prior to Mosix 1.6.0;

2. low-level debugging, guided by the supervision of some Mosix developers ([53]);

3. a Linux kernel with the OpenMosix extension has been compiled as User-Mode. This provided a virtual machine, where in principle OpenMosix and AliRoot could be debugged at lower level. Unfortunately, the process migration failed to work on the virtual machine, hampering the possibility to use this tool;

4. OpenMosix and AliRoot have been tested on a separate farm with different computer hardware, network and Linux distribution.

All these attempts failed to solve the problem.

4.3.4 Gentoo

In order to compare Gentoo with RedHat, the two distributions have been installed on two identical computers and an AliRoot event simulation has been launched with 3000 particles (default PPR Config.C file). After setting the same disk parameters using the `hdparm` Linux command, the two distributions gave the same timing results.

4.3.5 Storage and processing requests

We report here the computing time and storage required by running the whole simulation and reconstruction chain described in Chapter 5. As is the general case, the ultimate limiting factor for the production was the farm storage capability, unless deciding to free the memory by deleting the events and retaining only the final analysis objects. As far as the time requirements are concerned, the values reported in Table 4.1 refer to the running of the jobs without the overhead of failures of jobs due to accidental crashing of nodes or to errors in the setup of the configuration files, leading to the need

	generation		reconstruction		total running
	memory	running time	memory	running time	time on the farm
S/ev	165 kB	20 s	110 kB	2 s	
S	165 GB	5000 h	110 GB	500 h	12 days
B/ev	300 kB	10 s	110 kB	1.5 s	
B	600 GB	5000 h	220 GB	750 h	12 days

Table 4.1: *Summary of computing requirements (storage and processing time) for the simulation-reconstruction chain applied to* 10^6 *signal events and* 2×10^6 *background events.*

of rerunning the whole simulation or reconstruction chain; this time is of the same order of magnitude of the net time. The reported values don't take into account the human intervention either, which consisted mainly in writing *perl* scripts for distributing the jobs on the different nodes, due to the failure of mosix migrating AliRoot jobs; this time has been one order of magnitude smaller of the net time.

Chapter 5

$D^0 \to K^-\pi^+$ reconstruction in proton-lead collisions

In this chapter the feasibility study of the exclusive reconstruction of charm mesons in p-Pb (Pb-p) collisions in ALICE is described and the obtained results are presented. In Section 5.1 we outline the physical aspects concerning the hadronic decay $D^0 \to K^-\pi^+$; in Section 5.2 the choices for the generation for the background and the signal are presented and motivated; Section 5.3 presents the aspects related to the reconstruction of the primary vertex and of the tracks with their resolutions. In Section 5.5 the selection cuts applied to extract signal D^0 candidates from the combinatorial background are illustrated together with the statistical results. In Section 5.6 the statistical relative error is compared with an estimate of the various sources of systematic errors for the determination of the D^0 production cross section. During the exposition the computing requirements will be indicated since they were necessarily taken into account, in particular when choosing the simulation strategy, in order to gain a good statistical significance with limited mass storage and run time availability.

5.1 Decay topology and detection strategy

The investigation of medium-induced effects for charm quarks in the QGP requires a good sensitivity on the momentum distribution of the quarks. Clearly, a direct measurement of the momentum of D mesons would be more effective to this purpose than the indirect measurement via single electrons from the decay D→ e+X. The exclusive reconstruction of hadronic decays of D mesons is the only way to directly obtain their p_t distribution. The mesons D^0 and D^+ (and antiparticles) decay through weak processes and have decay

lengths of the order of few tenths of a millimeter, namely $c\tau$=(123.0 ±0.5) μm for the D^0 and $c\tau$=(311.8 ±2.1) μm for the D^+ [66]. Therefore, the distance between the interaction point (primary vertex) and their decay point (secondary vertex) is measurable. The selection of a suitable decay channel, which involves only charged-particle products, allows the direct identification of the charm states by computing the invariant mass of fully-reconstructed topologies originating from secondary vertices. We consider as a benchmark the process $D^0 \to K^-\pi^+$ (and $\bar{D}^0 \to K^+\pi^-$); the fraction of D^0 mesons which decay in this channel (branching ratio, BR) is 3.80±0.09%[66]. A sketch of the decay is shown in Fig. 5.1 (the charged tracks are drawn bent by a magnetic field). The main feature of this topology is the presence of two tracks displaced from the primary vertex. The variable that allows to evaluate the displacement of a track is the impact parameter, defined as the distance of closest approach of the track to the primary vertex. Here, we assume the presence of the ALICE solenoidal magnetic field and we indicate as d 0 the projection of the impact parameter on the bending plane, normal to the field direction.

It can be shown that, in the relativistic limit, the impact parameters of the decay products of a particle with mean proper decay length $c\tau$ have mean value of order $c\tau$. Therefore, the decay products of a D^0 particle have typical impact parameters of order 100 μm.

In order to extract the signal out of the background the candidate decay tracks are required to satisfy the following criteria for the secondary vertex:

1. they are well separated from the interaction vertex, i.e. their impact parameters are of order 100-500 μm; this is mandatory to reject the huge amount of primary tracks produced in a heavy ion collision;

2. the sum of their momenta, which estimates the momentum of the D^0 particle, points along the reconstructed D^0 flight line; this is realized by requiring the angle $\theta_{pointing}$ between the sum of the momenta and the primary-secondary vertex direction to be small (see sketch in Fig. 5.1).

This strategy requires:

- precise measurement of the momenta to have a good resolution on the invariant mass and, thus, reduce the background in the D^0 mass region

- measurement of the impact parameters with resolution of the order of 50 μm for the decay products of the D^0;

- particle identification to tag the two decay products and reject $\pi^{\mp}\pi^{\pm}$ pairs, which are a large part of the combinatorial background.

The ALICE central barrel, described in Chapter 3, was designed to fulfill these requirements, providing tracking and precise impact parameter measurement, with a Time Projection Chamber and a silicon Inner Tracking System, and K/π separation, with a Time-of-Flight detector, over the pseudorapidity range -0.9<η<0.9. The results on the feasibility of the strategy here outlined are reported in section 5.5.

Figure 5.1 shows a schematic picture of the topology of a $D^0 \rightarrow K^-\pi^+$ decay: a D^0 ($\bar{D}^0$) meson is originated in the primary vertex. After a mean life τ=410·10^{-15}s, corresponding to a decay length $c\tau$=123 μm, it decays in the secondary vertex into a $K^-\pi^+$ ($K^+\pi^-$) pair. The angle between the line of flight of the D^0 (the line connecting primary and secondary vertices) and the reconstructed d0 momentum (sum of the momenta of the reconstructed kaon and pion) is called *pointing angle* and indicated as θ_{point}. The minimum distances between the kaon and pion track prolongations and the primary vertex are called *track impact parameters* and indicated as d_0^K and d_0^π respectively.

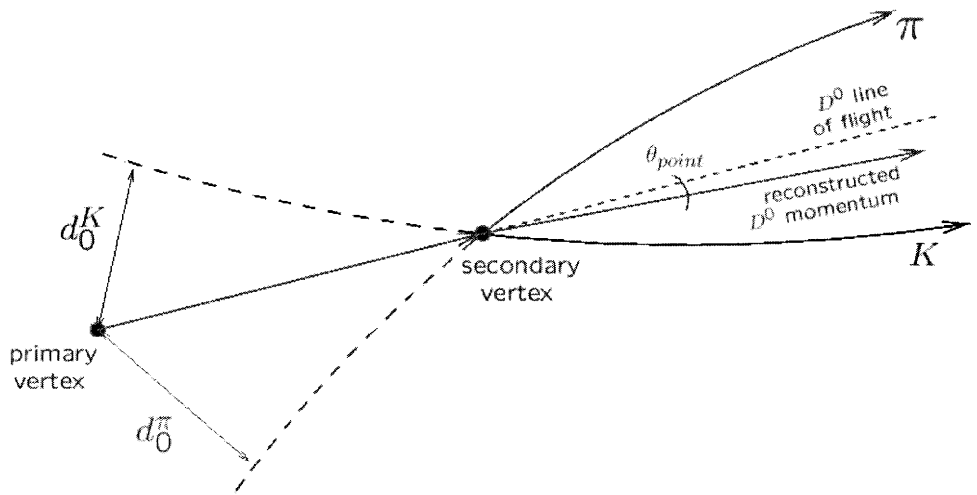

Figure 5.1: *Sketch of the decay topology (full explanation in the text).*

5.2 Background and signal generation

In the analysis stage of the present feasibility study we will deal with couples of tracks and select them in order to maximize the number of those really belonging to the same $D^0 \rightarrow K^-\pi^+$ decay. The remaining of the event (i.e. other tracks produced in the same p-Pb collision) is relevant w.r.t.

these tracks only for what concerns the detector and software capability to reconstruct them, which can be considered as dependent to the multiplicity alone. This consideration allows in particular to separately generate and treat background and signal events, while the alternative would be to select signal events as those p-Pb events containing a D^0 hadronic decay. Our choice offers two advantages w.r.t. the second approach:

1. it allows a much faster generation of the signal, since a single "signal event" corresponds to many hundreds background events;

2. it allows to generate the signal according to the transverse momentum distributions obtained by NLO calculations, because of the possibility to tune the PYTHIA event generator.

This issues are discussed in detail in the following of this section.

5.2.1 Background generation

The background events are p-Pb minimum bias events generated by means of the HIJING [44] event generator which includes the following background sources[1]:

- primary tracks (the originating vertex is the interaction region) which acquire an impact parameter through scattering with the beam pipe material;

- tracks from hyperons' decays;

- pions from antiprotons and antineutrons annihilating in the beam pipe or in the innermost pixel layer ($p\bar{p} \to \pi^-\pi^+$ or $n\bar{n} \to \pi^-\pi^+$).

The background sample consists of $2{\cdot}10^6$ p-Pb events.

The distribution of the pseudorapidity density of charged tracks in the barrel acceptance, $(dN_{ch}/d\eta)_{|\eta|<0.9}$, w.r.t. the collision impact parameter is shown in figure 5.2. The resulting averages for the whole sample of background events and for the subsample of background events with charm are 12.1 and 18.3 respectively. Events with charm, which result to be $\approx$13% of the whole sample[2], are distributed at lower impact parameters (i.e. more

[1]Some generators, e.g. parameterized generators, produce a background formed only by pion and kaon tracks in a fixed ratio and according to a multiplicity value tuned by the user.

[2]Cross section predictions for charm production at LHC energies span a wide range; however the value for p-Pb collisions at $\sqrt{s_{NN}}$=8.8 TeV resulting from the HIJING event generator turns out to be much lower of almost all current estimates.

central collisions, which favour hard scatterings) and their average multiplicity is higher since the high mass of $Q\bar{Q}$ pairs can originate more particles in the fragmentation process than light quarks or gluons do.

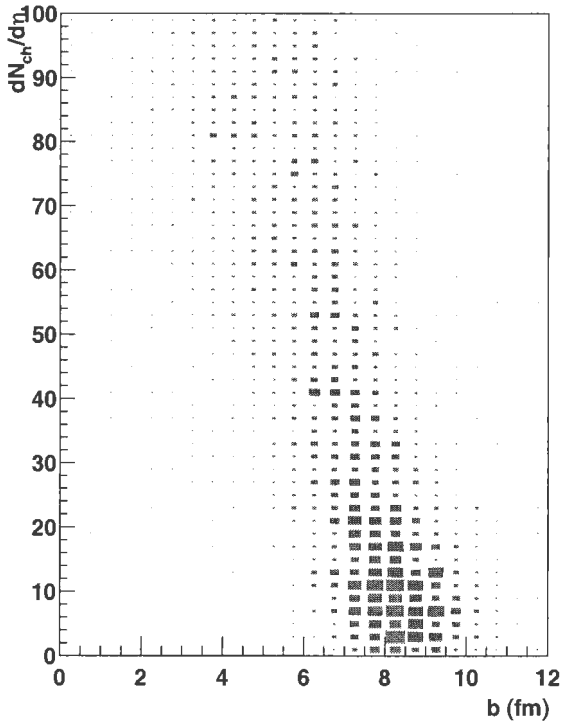

Figure 5.2: Scatter-plot of the multiplicity in the barrel acceptance w.r.t. the impact parameter of the collision in HIJING minimum-bias p-Pb events.

The p_t-distribution for kaons (left) and pions (right) in background events is shown in Figure 5.4 by the dashed black lines.

5.2.2 Signal generation

The "signal events", as anticipated, are not physical events; instead they are given by the superposition of D^0 decay tracks generated by means of the PYTHIA ([67], [68]) event generator. The version 6.150 of the program was used with the CTEQ 4L set of PDF and with the parameters tuned in order to reproduce the multiplicity of all available collider data [69]. As detailed in [69], the main parameter tuned is the low-p_t cut-off, p_t^{min}, introduced in the model to regularize the dominant 2→2 QCD cross sections, which diverge

as $p_t \to 0$ and drop rapidly at high p_t. In order to reproduce the data, a monotonic increase of p_t^{min} has to be introduced.

The number of decays in the same event has been fixed to 25 in order to get the same multiplicity in the barrel acceptance as the average charged multiplicity in background events with charm ($dN_{ch}/d\eta$=18.3); this will allow to reconstruct signal decay tracks with the same reconstruction resolution and efficiency as for the background.

A rapidity window for the generation of the D^0 mesons has been chosen; this will allow for computing requirements saving. In order not to bias the final sample of detectable D^0s, one has to avoid to exclude those D^0 mesons whose decay products fall both in the barrel acceptance; on the other hand if one or both of them have a pseudorapidity η>0.9, the original D^0 meson is not detectable. The rapidity distribution of the mother particle D^0 for the three samples (both, one or no decay product in the barrel acceptance) is shown in Fig. 5.3. It turns out that the rapidity window -1<y_{D^0}<+1 is

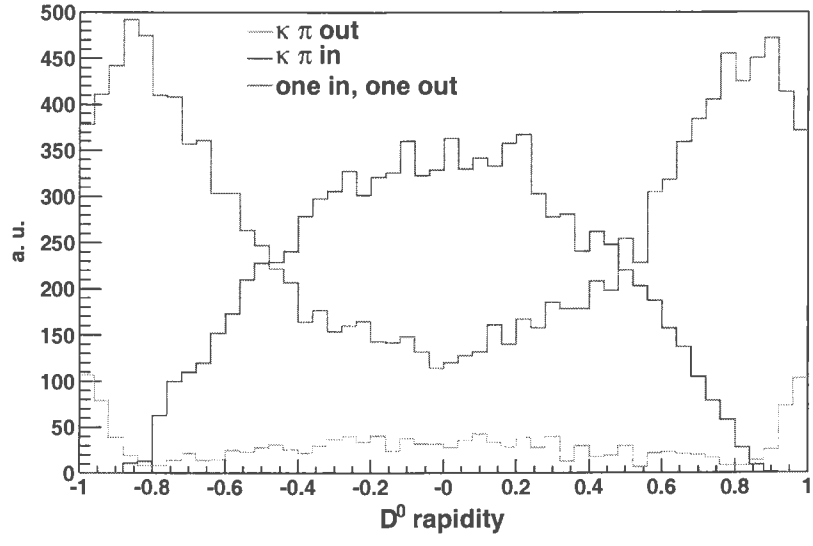

Figure 5.3: *Rapidity distribution (in the laboratory frame of reference) for D^0 mesons whose hadronic decay products fall both in the barrel acceptance (blue), both outside (green) or one in and one out (red).*

a good choice; inside this window, 39% of the D^0s produced are detectable while the remaining 61% of D^0s send at least one of the two decay products outside the barrel acceptance.

The p_t-distribution for kaons (left) and pions (right) in signal events is shown in Figure 5.4 by the solid blue lines and compared to the same distri-

butions for kaons and pions produced in the background (dashed black lines). As expected signal distributions are harder.

D^0 mesons can result from primary charm quark decays ($c \to D^0$) or from secondary B quark decays ($b \to B \to D^0$). The ratio of D^0 mesons from b quarks to D^0 mesons from c quarks is given by:

$$\frac{dN(b \to B \to D^0)/dy}{dN(c \to D^0)/dy} = \frac{dN(b \to B^0, B^+)/dy \cdot BR(B^0, B^+ \to D^0)}{dN(c \to D^0)/dy}$$

The average rapidity densities for D^0, B^0 and B^+ production are $<dN/dy>_{y_{lab}}$= 0.096, 0.003 and 0.003 respectively , in the laboratory rapidity range [-1,1] in p-Pb collisions at $\sqrt{s_{NN}}$=8.8 TeV. This values are extracted from [32], Table 3.8, where they are obtained by tuning the PYTHIA event generator to reproduce the most relevant heavy quark kinematic distributions derived by NLO calculations; furthermore PYTHIA has been normalized in order to reproduce the cross section including shadowing obtained with the same calculations.

Making also use of the branching ratio $BR(B^0, B^+ \to D^0)$=63.9%, we get:

$$\frac{dN(b \to B \to D^0)/dy}{dN(c \to D^0)/dy} = 0.040 = 4.0\%$$

This ratio is small but not negligible; furthermore it is expected to increase after applying selection cuts which are more effective at high-p_t, favouring the D^0 mesons from beauty. The presence of secondary D^0 mesons has to be accounted by subtracting them from the total number of D^0 mesons in order to get only those from c quarks; this leads to one of the main contributions to the final systematic error, as estimated in [32].

The statistical results presented later in Section 5.5 are obtained from the background and signal events produced as described in the present Section and scaled to 10^8 p-Pb events, which are expected to be collected in the period scheduled at LHC for proton-lead running. This choice will not affect the results concerning the estimate of the signal-to-background ratios shown later in Section 5.5, but only the statistical significance $\mathcal{S} = S/\sqrt{S+B}$.

5.3 Reconstruction

The D^0 mesons form in a region not distinguishable from the primary vertex, where the collision has taken place; before decaying via hadronic decay they then cover distances of order 100 μm. The identification of secondary vertices, displaced from the primary one is the most effective criterion to select D^0

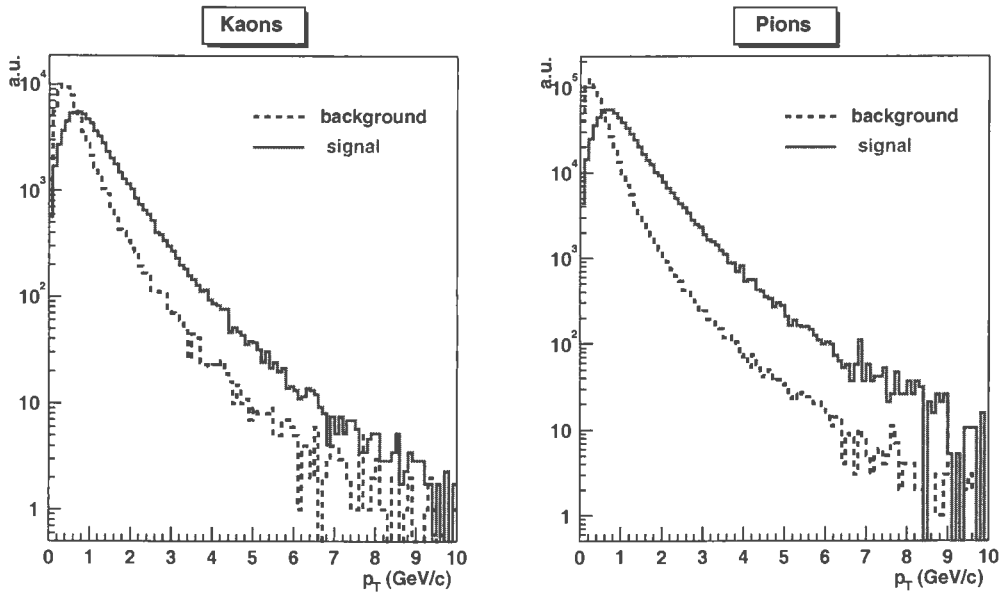

Figure 5.4: *p_t-distributions for kaons and pions in the signal (solid blue) and in the background (dashed black), normalized to the same integral.*

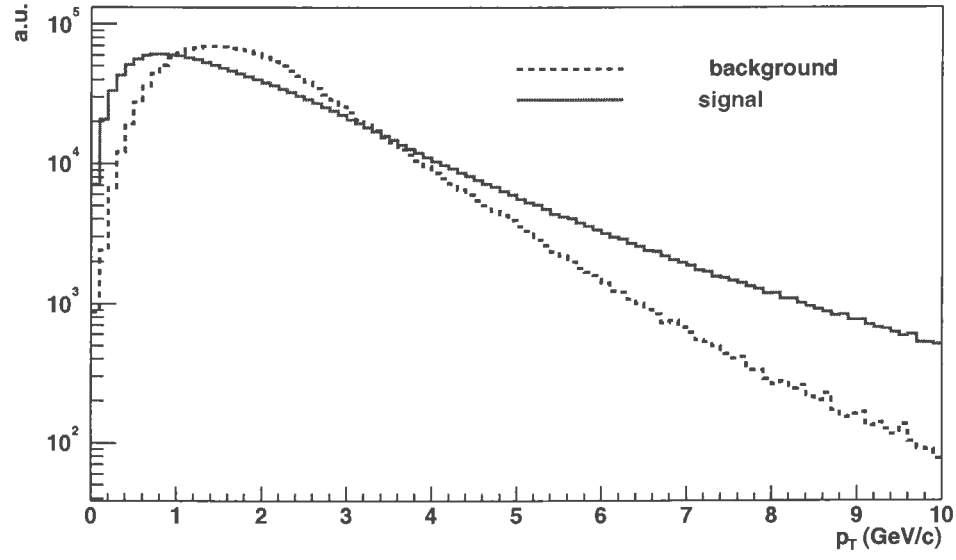

Figure 5.5: *p_t-distributions for D^0-candidates in the signal (solid blue) and in the background (dashed black), normalized to the same integral.*

decay particles from strange, charm or beauty mesons, which are generally characterized by mean proper decay lengths of order 100 μm (e.g. $c\tau = 123$ μm for the D^0, $c\tau = 312$ μm for the D^+). A good resolution, of order few tenths of μm, is then required for both track reconstruction and primary vertex reconstruction in order to extract signal tracks, i.e. true decay tracks, out of the background of particles from the primary vertex. As outlined in Chapter 3, the ALICE detector has been designed to be able to achieve such resolutions. In this section we focus on the resolutions achieved on the track impact parameter, which is the variable evaluating the displacement of a track from the primary vertex. The track impact parameter is defined through its two components along the transverse plane ($r\phi$-plane in polar coordinates, xy-plane in Cartesian coordinates) and the beam direction z. Charged tracks are bended by the magnetic field to form helices with axes parallel to the beam-axis and those with circular projection in the transverse plane ; thus 3 components of the 5-dimensional state vector of the track identifies in the transverse plane a circle, say of radius R and center (x_C, y_C); if the vertex has coordinates (x_V,y_V,z_V), the impact parameter projection in the transverse plane is given by:

$$d_0(r\phi) \equiv q \cdot \left(R - \sqrt{(x_V - x_C)^2 + (y_V - y_C)^2}\right)$$

where q is the sign of the particle charge. Note that this definition assigns a sign to the impact parameter, which, as we will show in Section 5.5 turns out to be very effective at the analysis stage, since it allows the track impact parameter to carry also the information on the sign of the track. Along the beam direction the impact parameter projection is simply given by:

$$d_0(z) \equiv z_{track} - z_V$$

where z_{track} is the z-coordinate of the track at the distance of closest approach in the bending plane, i.e. when $\sqrt{(x_V - x_{track})^2 + (y_V - y_{track})^2}$ reaches its minimum value. From this two definitions it turns out that both the resolution on the vertex position and on the track position give a contribution to the impact parameter resolution, for both the z and $r\phi$ projections.

As shown in Section 3.3, we can assume for p-Pb collisions an apriori knowledge (from the beam parameters) of the primary vertex position with an uncertainty of $\approx$10–15 μm in the transverse plane, while in the beam direction the knowledge of the primary vertex position must be improved by an event-by-event reconstruction to achieve the resolution requirements needed for the identification of secondary vertices.

The resolution on the vertex has finally to be combined with that on the track position to obtain the impact parameter resolution in p-Pb events.

Finally, we describe the reconstruction of the secondary vertex position in the case of the two-body decay $D^0 \to \kappa^-\pi^+$. We show the achieved spatial resolution, which is important for the precise determination of the D^0 flight line and, consequently, of the pointing angle, the other key variable for the identification of displaced vertex topologies.

5.3.1 Primary vertex reconstruction

In all collision systems (p-p, p-Pb and Pb-Pb) the interaction points are spread along the z-direction according to a Gaussian with σ=5.3 cm; even in the low multiplicity collision systems, a first estimate of the z-coordinate of the primary vertex can be obtained before any knowledge on the tracks to help track reconstruction itself. This estimate is achieved using the correlation of clusters in the innermost ITS layers, the pixel layers having radius 5 cm and 8 cm respectively. The method, described in [48] and in [70] for the high- and low-multiplicity environments respectively, consists in obtaining the primary vertex z-component V_z from the *tracklets*, that is from the line segments joining pairs of pixel clusters from each of the two pixel layers; this segments are prolonged to the beam axis and the resulting V_z distribution is plotted. The combinatorial background can be partially removed by discarding those tracklets from pixel clusters not close enough in the azimuthal angle. "True tracklets", i.e. tracklets from pixel clusters belonging to the same track, point to the primary vertex and allow to identify V_z with a resolution which has been parametrized as:

$$\sigma_z(dN_{ch}/dy) = \left(2 + \frac{292}{dN_{ch}/dy}\right) \mu m$$

in [48] for Pb-Pb collisions and as:

$$\sigma_z(dN_{ch}/dy) = \left(42 + \frac{290}{dN_{ch}/dy}\right) \mu m$$

in [70] for p-p collisions. The p-Pb collision system gives rise to a similarly low multiplicity environment; for minimum bias p-Pb events containing charm the average charged track density at midrapidity is dN_{ch}/dy=18.2 and thus this parameterization leads to estimate $\sigma_z = 42 + 290/\sqrt{dN_{ch}/dy} \simeq 110\mu$m. This first estimate of the primary vertex z-coordinate does not met the requirements mentioned above for the identification of secondary vertexes; however it allows a significant improvement in the efficiency of the ITS tracking. After the tracking has been performed as described in 3.2.3 using the combined information from the TPC and ITS sub-detectors, the tracks are used

to trace back the spatial position of the primary vertex using the algorithm described in [70]. Tracks (helices) are approximated to their tangent at the bending plane intersection; the primary vertex coordinates are then given as the average of the coordinates of the median points of the minimum distance segments for all the track pairs. This estimate is then improved by minimizing the χ^2 as defined in [70] and [71] and by rejecting the tracks giving a too large contribution to the total χ^2.

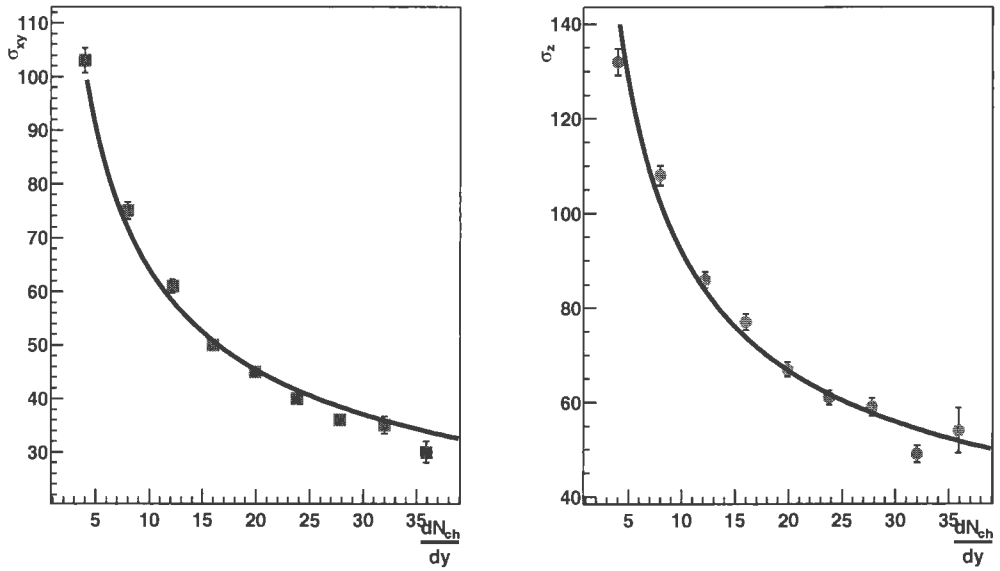

Figure 5.6: *Resolutions in the transverse plane ($\sigma_{x,y}$, left) and in the longitudinal direction (σ_z, right) for the primary vertex position reconstructed from the tracks, as described in the text.*

The use of this algorithm has allowed to estimate the primary vertex position with the resolutions shown in Fig. 5.6 as a function of the event multiplicity. Extracting the resolution values corresponding to the average multiplicity of minimum bias p-Pb events ($\approx$45 μm and $\approx$65 μm respectively for $\sigma_{x,y}$ and σ_z), we conclude that the best knowledge on the primary vertex position is expected to be $\approx$15 μm, expected from the beam parameters, in the transverse plane, and $\approx$65 μm along the z-direction, from the primary vertex reconstructed by means of the algorithm described above.

5.4 Particle identification

Most of the D^0 candidates have a transverse momentum between 0.5 and 3 GeV, as can be seen from Figure 5.5; in this region Particle IDentification (PID) is mainly performed by the TOF detector, described in Section 3.1.3. The PID analysis described here is based on a parameterization of the TOF response[3] obtained for the pp collision system[4]. A possible future improvement of this simulation could include the "combined particle identification", i.e. an AliRoot tool to combine the PID information from all the barrel detectors; at the time of the present simulation this tool was still under development.

The performance of a TOF system for particle identification depends on the intrinsic timing resolution of the detectors as well as the system's resolution. For a particle with momentum p (assigned from TPC and ITS) traveling a distance l in a time interval t,the following expression for the mass of the particle m holds:

$$m = p \cdot \sqrt{\frac{t^2}{l^2} - 1}$$

It follows that the are mainly three contributions to the mass resolution $\frac{\partial m}{m}$: $\frac{\partial p}{p}$, $\frac{E^2}{m}\frac{\partial t}{t}$ and $\frac{E^2}{m}\frac{\partial l}{l}$. At relatively high momenta it is predominantly affected by the intrinsic TOF error resolution on the time-of-flight t ($90ps$) and track length l ($30ps$) measurements; the other timing error contributions arise from the momentum determination ($20ps$), from the treatment of the signal – digitization, amplification, ... ($50ps$) – and from shifts between online and offline calibrations and corrections ($80ps$), where the numbers in parenthesis are the different error contributions as estimated in the TOF TDR. The resulting overall resolution is $\approx 150ps$.

The association of the particle type to a track (tagging) is determined by applying cuts on the momentum-versus-mass plane. The values of these cuts determine the identification efficiency and the contamination of the sample. The identification efficiency for a particle type i is defined as the ratio of the number of tracks of type i correctly tagged as i to the total number of tracks of type i; the contamination is defined as the ratio of the number of

[3] A real simulation of the TOF response would have forced as to abandon the strategy adopted for the event simulation, consisting, as described in Section 5.2, in stopping the transport at the entrance of the TPC detector to considerably minimize computing time and storage requirements.

[4] The average charged particle density at central rapidities in pp collisions is ~6, while in p-Pb collisions is 12, compared with expected values of ~3000 for Pb-Pb collisions. In the first two cases we are far from the allowed detector occupancies, thus it's reasonable to expect similar efficiencies.

tracks incorrectly tagged as i to the total number of tracks tagged as i. The optimal level of contamination and efficiency depends on the specific physics case under study.

The reconstructed tracks are assigned PID weights, ranging from 0 to 1, according to the probability to be identified as pions (π_{tag}), as kaons (K_{tag}), as protons (p_{tag}) or to be non-identified ($?_{tag}$). A $D^0 \rightarrow K^-\pi^+$ decay for which both the pion and the kaon tracks are reconstructed corresponds to a pair of tracks of opposite charge (-,+). According to the PID weights of the single tracks, the pair is given a weight for each of the following samples:

- Sample A (K_{tag}, π_{tag}) + (K_{tag}, $?_{tag}$): the kaon is identified while the other track can be identified as pion or non-identified;
- Sample B ($?_{tag}$, π_{tag}): only the positive track is identified as a pion;
- Sample C ($?_{tag}$, $?_{tag}$): both tracks are not identified. In this sample each pair is counted twice: once as a D^0-candidate and once as a $\bar{D}^0$-candidate;
- Sample D: all the remaining combinations.

If the pion from a D^0 decay is correctly identified, but the kaon is misidentified as a pion, the candidate is lost. Therefore, for open charm detection, the PID strategy has to be optimized in order to minimize the number of kaons tagged as pions, while tagging correctly a large fraction of the pions. On the basis of this guideline the PID tags have been defined in the following way:

- any track not matched with a single-fired TOF pad is tagged as $?_{tag}$;
- tracks matched with a single-fired TOF pad are tagged according to the graphical cuts applied in the momentum versus mass TOF plot (see [32]); if a track falls outside all graphical cuts it is tagged as $?_{tag}$.

The graphical cuts were optimized in order to minimize the probability to tag a kaon as a pion, i.e. to minimize the loss of signal.

In this way, for every particle type, we can compute the probabilities to be tagged as pion, kaon, proton or non-identified. These probabilities are shown in Fig. 5.7 as a function of the total momentum. We give an example of how these figures should be read: for a reconstructed track (in TPC and ITS), known from the simulation to be a kaon, with p = 1 GeV/c, the probability to be tagged as kaon is 45%, the probability to tagged as pion is 8% and the probability to be tagged as non-identified is the remaining 47% (see central panel).

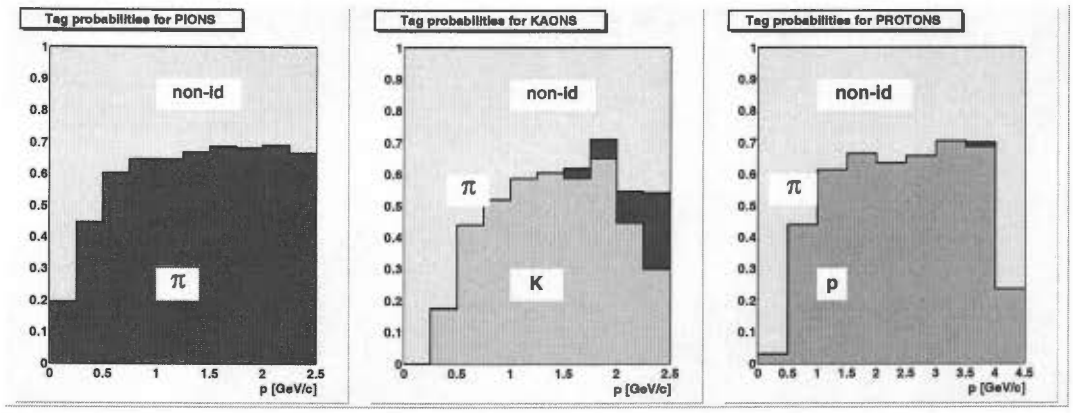

Figure 5.7: *Plot of PID identification capabilities for pions, kaons and protons: for each particle species the plot shows the probability of correctly identifying the particle or of misidentifying it, in function of its transverse momentum.*

In our study the TOF detector was not included in the simulation of all the events and the three samples A, B and C were populated with D^0 candidates according to the tabulated probabilities from the figure, both for the signal and for the background. The PID information was used for p $<$ 2 GeV/c for pions and kaons and for p $<$ 4 GeV/c for protons; for larger momenta all tracks were tagged as $?_{tag}$ (non-id). The fraction of signal lost because the kaon is tagged as a pion is 10%.

5.5 Analysis

Signal track pairs (K^-, π^+) from D^0 hadronic decays and background combinatorial opposite charge track pairs build up the signal (S) and the background (B) samples of D^0 candidates.

We applied several selection cuts in order to increase the S/B ratio or, preferably, in order to increase the statistical significance $\mathcal{S}$ of the whole (S,B) sample. The preliminary selection is made on the basis of the invariant mass of the track pairs; for each of them the position of the secondary vertex is given by the middle-point of the minimum distance between the two helicoidal tracks; at this point the D^0 momentum is given by the sum of the momenta, $(E_1, \vec{p}_1)$ and $(E_2, \vec{p}_2)$, of the two decay tracks: $\vec{p}_1 + \vec{p}_2$. The invariant mass of the track pair at the position of closest approach is given by $M_{inv} = \sqrt{(E_1 + E_2)^2 + (\vec{p}_1 + \vec{p}_2)^2}$. The average resolution is 13 MeV; it increases with the transverse momentum of the D^0 due to the analogous

trend of the momentum resolution. In this section we show the effect on the signal and background D^0 candidates samples of the application of the PID cut and of the kinematic cuts.

Table 5.1 compares the initial statistics for the two samples with that obtained after the application of the PID cuts to select PID-samples A, B, C and ABC (explained in Section 5.4) in the invariant mass range $|M_{inv} - M_{D_0}| < 3\sigma$.

	S/event	B/event	S/B
no PID	3.94×10^{-4}	6.32×10^{-1}	6.24×10^{-4}
sample A	2.29×10^{-4}	2.29×10^{-2}	1.00×10^{-2}
sample B	1.67×10^{-4}	1.40×10^{-1}	1.19×10^{-3}
sample C	9.47×10^{-5}	1.15×10^{-1}	8.23×10^{-4}
sample ABC	2.20×10^{-4}	2.78×10^{-1}	7.91×10^{-4}

Table 5.1: *Initial p_t-integrated statistics and statistics after the selection of the various PID samples.*

It can be seen that the highest increase in the S/B ratio is given by selecting the PID-sample A; however the effect of the PID strongly depends on the momentum of the tracks on which it is applied. In general this dependence affects the kinematic cuts too; thus we divided the signal and background D^0 candidates samples into five bins according to the transverse momentum of the D^0 candidate. Table 5.2 shows how the choice of the different PID samples affects the S/B ratio and the significance in the different ranges of $p_t^{D^0}$; at low $p_t^{D^0}$ the PID is more efficient and the selection of $(K,?)$ pairs alone (sample A) significantly enhances the statistics; at high transverse momenta the PID is not effective and is better to release the PID cuts.

Furthermore the effect of the selection of a particular PID sample is not independent of the application of the other selection cuts (namely kinematic cuts) and thus applying it before of after them leads to different results. For this reason we did not apply cuts separately (i.e. on the S and B subsamples selected by some previously applied cut); instead we applied PID and kinematic cuts at the same time to select the complete set of cuts (PID and kinematic) optimizing the statistical significance; this search in the space of the cut values has been performed subdividing the signal and background samples on the basis of the transverse momentum of the D^0 candidate, since the PID and kinematic cuts strongly depend on it. An explanation of the kinematic cuts relative to the decay topology is given in the remaining of this section.

PID sample	statistics	$p_t^{D^0} < 1$	$1 < p_t^{D^0} < 2$	$2 < p_t^{D^0} < 3$	$3 < p_t^{D^0} < 5$	$p_t^{D^0} > 5$	p_t-integrated
no PID	S/ev	$3.01 \cdot 10^{-4}$	$3.28 \cdot 10^{-4}$	$1.98 \cdot 10^{-4}$	$1.56 \cdot 10^{-4}$	$7.65 \cdot 10^{-5}$	$1.06 \cdot 10^{-3}$
	B/ev	$9.92 \cdot 10^{-2}$	$2.55 \cdot 10^{-1}$	$1.65 \cdot 10^{-1}$	$9.16 \cdot 10^{-2}$	$2.12 \cdot 10^{-2}$	$6.32 \cdot 10^{-1}$
	S/B	$3.03 \cdot 10^{-3}$	$1.29 \cdot 10^{-3}$	$1.20 \cdot 10^{-3}$	$1.70 \cdot 10^{-3}$	$3.61 \cdot 10^{-3}$	$1.67 \cdot 10^{-3}$
	$S/\sqrt{S+B}$	9.53	6.49	4.87	5.15	5.25	13.3
A	S/ev	$1.61 \cdot 10^{-4}$	$1.69 \cdot 10^{-4}$	$7.71 \cdot 10^{-5}$	$4.06 \cdot 10^{-5}$	$9.68 \cdot 10^{-6}$	$4.58 \cdot 10^{-4}$
	B/ev	$5.30 \cdot 10^{-3}$	$1.14 \cdot 10^{-2}$	$4.52 \cdot 10^{-3}$	$1.38 \cdot 10^{-3}$	$3.19 \cdot 10^{-4}$	$2.29 \cdot 10^{-2}$
	S/B	$3.04 \cdot 10^{-2}$	$1.49 \cdot 10^{-2}$	$1.71 \cdot 10^{-2}$	$2.94 \cdot 10^{-2}$	$3.03 \cdot 10^{-2}$	$2.00 \cdot 10^{-2}$
	$S/\sqrt{S+B}$	21.8	15.8	11.4	10.7	5.34	30.0
B	S/ev	$8.84 \cdot 10^{-5}$	$9.16 \cdot 10^{-5}$	$6.10 \cdot 10^{-5}$	$6.07 \cdot 10^{-5}$	$3.32 \cdot 10^{-5}$	$3.35 \cdot 10^{-4}$
	B/ev	$2.37 \cdot 10^{-2}$	$5.60 \cdot 10^{-2}$	$3.61 \cdot 10^{-2}$	$1.95 \cdot 10^{-2}$	$4.79 \cdot 10^{-3}$	$1.40 \cdot 10^{-1}$
	S/B	$3.74 \cdot 10^{-3}$	$1.64 \cdot 10^{-3}$	$1.69 \cdot 10^{-3}$	$3.11 \cdot 10^{-3}$	$6.92 \cdot 10^{-3}$	$2.39 \cdot 10^{-3}$
	$S/\sqrt{S+B}$	5.74	3.87	3.21	4.34	4.77	8.94
C	S/ev	$4.99 \cdot 10^{-5}$	$5.40 \cdot 10^{-5}$	$3.85 \cdot 10^{-5}$	$3.81 \cdot 10^{-5}$	$2.91 \cdot 10^{-5}$	$2.10 \cdot 10^{-4}$
	B/ev	$1.73 \cdot 10^{-2}$	$4.12 \cdot 10^{-2}$	$3.08 \cdot 10^{-2}$	$2.44 \cdot 10^{-2}$	$7.95 \cdot 10^{-3}$	$1.22 \cdot 10^{-1}$
	S/B	$2.89 \cdot 10^{-3}$	$1.31 \cdot 10^{-3}$	$1.25 \cdot 10^{-3}$	$1.56 \cdot 10^{-3}$	$3.66 \cdot 10^{-3}$	$1.72 \cdot 10^{-3}$
	$S/\sqrt{S+B}$	3.79	2.66	2.19	2.44	3.26	6.0
AB	S/ev	$2.49 \cdot 10^{-4}$	$2.61 \cdot 10^{-4}$	$1.38 \cdot 2.10^{-4}$	$1.01 \cdot 10^{-4}$	$4.28 \cdot 10^{-5}$	$7.93 \cdot 10^{-4}$
	B/ev	$2.90 \cdot 10^{-2}$	$6.74 \cdot 10^{-2}$	$4.06 \cdot 2.10^{-2}$	$2.09 \cdot 10^{-2}$	$5.11 \cdot 10^{-3}$	$1.63 \cdot 10^{-1}$
	S/B	$8.61 \cdot 10^{-3}$	$3.88 \cdot 10^{-3}$	$3.40 \cdot 2.10^{-3}$	$4.85 \cdot 10^{-3}$	$8.39 \cdot 10^{-3}$	$4.87 \cdot 10^{-3}$
	$S/\sqrt{S+B}$	14.6	10.0	6.84	6.99	5.97	19.6
ABC	S/ev	$2.99 \cdot 10^{-4}$	$3.15 \cdot 10^{-4}$	$1.77 \cdot 10^{-4}$	$1.39 \cdot 10^{-4}$	$7.19 \cdot 10^{-5}$	$1.00 \cdot 10^{-3}$
	B/ev	$4.62 \cdot 10^{-2}$	$1.08 \cdot 10^{-1}$	$7.14 \cdot 10^{-2}$	$4.53 \cdot 10^{-2}$	$1.31 \cdot 10^{-2}$	$2.85 \cdot 10^{-1}$
	S/B	$6.47 \cdot 10^{-3}$	$2.90 \cdot 10^{-3}$	$2.47 \cdot 10^{-3}$	$3.08 \cdot 10^{-3}$	$5.51 \cdot 10^{-3}$	$3.52 \cdot 10^{-3}$
	$S/\sqrt{S+B}$	13.9	9.55	6.60	6.54	6.28	18.8

Table 5.2: *The statistics for the various PID samples (rows) integrated over the different p_t bins (columns), before applying the kinematic cuts. The PID samples giving the highest significance for each p_t bin after the kinematic cuts are applied are highlighted. The last column shows the statistics integrated over the full range of p_t.*

Figure 5.4 shows the transverse momentum distributions for signal and background pions and kaons; since they are harder for the signal, a cut on the minimum p_t for kaons and pions has been evaluated.

Pairs for which the distance of closest approach (dca) between the tracks is larger than dca_{max} (300-400 μm, depending on the transverse momentum of the D^0 candidate) are rejected.

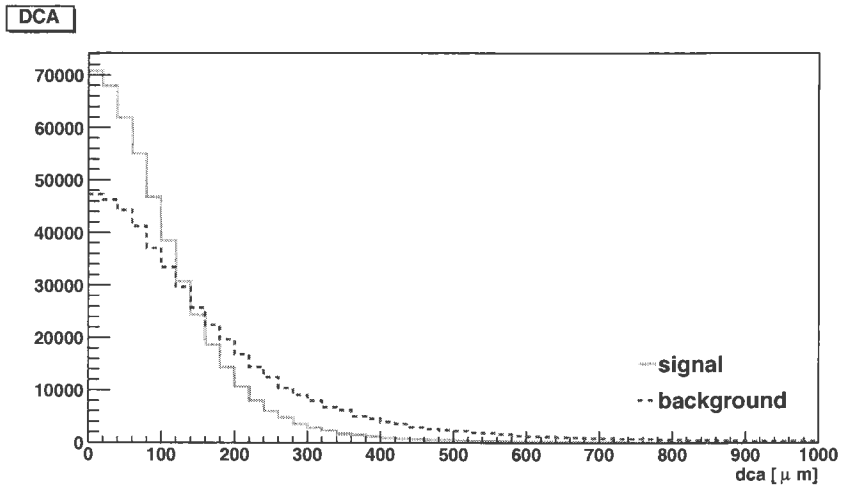

Figure 5.8: *Distribution of the distance of closest approach (as defined in the text) for two decay particles for the signal (solid green) and background (dashed blue).*

We define θ^* as the angle between the pion momentum and the D^0 flight line (see sketch in Fig. 5.1) in the reference frame of the decaying D^0. The signal distribution of θ^* is quite flat, while the background peaks around $|\theta^*|$=1; therefore an upper cut on $|\theta^*|$ turns out to be convenient.

Further improvement can be obtained on the basis of the impact parameters and by requiring the reconstructed D^0 to point back to the primary vertex (small pointing angle): this cuts are explained in the following.

We consider only the impact parameter projection on the transverse plane ($d_0(r\phi)$, simply indicated as d_0 in the following) since it is measured much more precisely than that along the z-direction. It can be seen that for large impact parameters ($|d_0|$>500 μm) the dominant background comes from the decay of hyperons and kaons. Indeed, we have found that an upper cut on d_0 gives an efficient rejection of this background contribution.

The projection of the tracks on the bending plane allows us to define a sign for the impact parameter, as explained in Section 5.3. This sign is positive or negative according to the position of the track projection with

respect to the primary vertex (the orientation is given by the direction of the track momentum). The tracks of opposite charge originating from a D^0 decaying far from the primary vertex will then have impact parameters of opposite signs and large in absolute value. As a consequence the product of the transverse projections of the impact parameters of the two tracks turns out to be a very appropriate variable for selection cuts. For true decay pairs this quantity tends to be negative and large in absolute value, while for background track pairs the distribution is much more uniform. In Fig. 5.10 we plot the distribution of the product of impact parameters for signal and background, normalized to the same integral. The cut on the product of impact parameters has a much bigger impact than the cuts on the impact parameter of each single track and makes them of little use.

The condition for the D^0 to point back to the primary vertex is imposed by a cut on the *pointing angle* $\theta_{pointing}$, i.e. the angle between the D^0 line of flight (connecting the primary and the secondary vertex) and the momentum vector of the D^0 candidate. As shown in Fig. 5.9 the cosine of $\theta_{pointing}$ peaks at $+1$ for the signal, and is almost uniformly distributed for the background. A much larger rejection factor can be obtained by combining these two cuts. In fact, if the secondary vertex is well separated from the primary one, the impact parameters are large and the pointing angle is small, since the D^0 flight direction is measured with a better resolution. Therefore, the two variables are strongly correlated in the signal, while this correlation is absent in the background. This can be seen in Fig. 5.11, which shows the two-dimensional scatter plot of $\cos(\theta_{pointing})$ versus the product of the impact parameters for the signal (left) and the background (right) samples.

The signal and background D^0 candidates samples have been subdivided in five bins of D^0 transverse momentum: $p_t^{D^0}<1$ GeV, 1 GeV$<p_t^{D^0}<2$ GeV, 2 GeV$<p_t^{D^0}<3$ GeV, 3 GeV$<p_t^{D^0}<5$ GeV, $p_t^{D^0}>5$ GeV. Inside each $p_t^{D^0}$-bin a search in the 12-dimensional[5] and on space of the cut values (PID included) was performed in order to maximize the statistical significance $\mathcal{S}=S/\sqrt{S+B}$ computed for 10^8 p-Pb minimum bias events. In table 5.4 we report the final values of the cuts and in table 5.3 the final statistics obtained with those cuts in the five p_t bins is shown.

Table 5.5 summarizes the various effects (to be ascribed to acceptance and reconstruction conditions) reducing the signal starting from the initial sample of D^0s produced in one proton-lead event to the final fraction of D^0 candidates passing all the cuts (including the $\pm 3\sigma$ cut on the invariant mass). The fraction of selected signal $D^0 \to K^-\pi^+$ is 4.38%; the fraction of recon-

[5]The search has been performed on the 8 different kinematic cuts and 4 different PID samples listed above

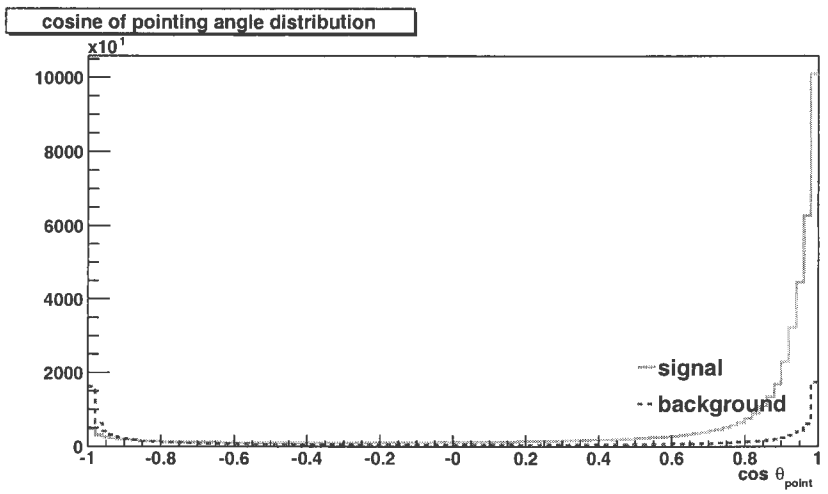

Figure 5.9: *Distribution of the cosine of the pointing angle of the two decay particles for the signal (solid green) and background (dashed blue).*

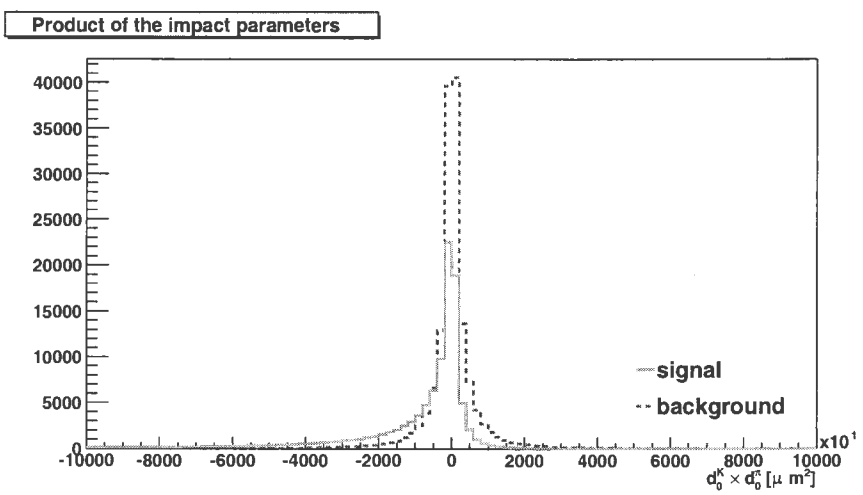

Figure 5.10: *Distribution of the product of the impact parameters of the two decay particles for the signal (solid green) and background (dashed blue).*

p_t bin	S/ev	B/ev	S/B	$\mathcal{S}$	$\epsilon_{rel}(\%)$
$p_t^{D^0}$<1	1.6×10^{-4}	5.3×10^{-3}	3.0×10^{-2}	21.8	4.6
1<$p_t^{D^0}$<2	1.5×10^{-5}	1.6×10^{-5}	2.2×10^{-1}	26.3	3.8
2<$p_t^{D^0}$<3	1.8×10^{-5}	1.4×10^{-5}	1.3	32.2	3.1
3<$p_t^{D^0}$<5	2.8×10^{-5}	2.6×10^{-5}	1.1	38.5	2.6
$p_t^{D^0}$>5	2.3×10^{-5}	2.9×10^{-5}	8.2×10^{-1}	32.5	3.1

Table 5.3: *Final statistics in the five p_t-bins obtained with the set of PID and kinematic cuts listed in Table 5.4. The relative statistical error is given in percentage in the last column as the inverse of the statistical significance, thus as $\sqrt{S+B}/S$.*

p_t bin cut	PID	DCA	$\cos\theta^*$	p_t^K	p_t^π	d_0^K	d_0^π	$d_0^K \times d_0^\pi$	$\cos\theta_{point}$
$p_t^{D^0}$<1	A	∞	1.1	0	0	∞	∞	∞	-1.1
1<$p_t^{D^0}$<2	A	300	1.1	0.6	0.6	800	800	-20000	0.7
2<$p_t^{D^0}$<3	ABC	200	0.8	0.8	0.7	800	800	-20000	0.7
3<$p_t^{D^0}$<5	ABC	200	0.8	0.8	0.7	800	800	-10000	0.7
$p_t^{D^0}$>5	ABC	200	0.9	0.8	0.7	1000	1000	-5000	0.8

Table 5.4: *The final PID samples and kinematic cuts applied in the different bins of transverse momentum in order to maximize the significance for each bin. The statistical parameters of the final sample selected with this cuts are shown in table 5.3.*

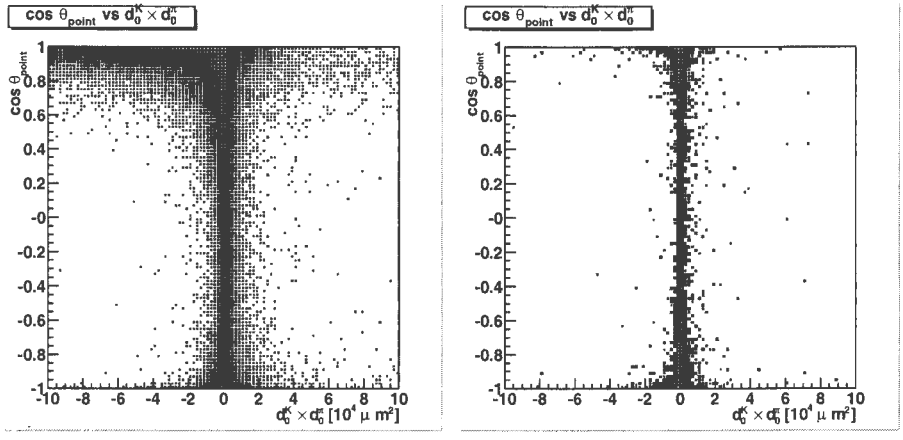

Figure 5.11: *Scatter-plot of the cosine of the pointing angle vs. the product of the impact parameters of the two decay particles for the signal (left) and the background (right).*

structed detectable $D^0 \to K^-\pi^+$ is 11%, if we consider as detectable those D^0 hadronic decays whose decay products fall both in the barrel acceptance.

	S/ev (p-Pb)
Total D^0+$\bar{D}^0$	0.926
+ $\|y^{D^0}\|$<1	0.192
+ decaying to $K\pi$	7.3×10^{-3}
+ K and π both in $\|\eta\|$<0.9	2.9×10^{-3}
+ reconstructed	1.1×10^{-3}
+ PID	3.5×10^{-4}
+ selection cuts	3.2×10^{-4}

Table 5.5: *Number of signal D^0s per event from their production, through decays, acceptance cuts, tracking, PID selection and kinematic cuts.*

After the kinematic cuts have been applied, and thus subregions in the phase space have been selected, the significance obtained in the different PID samples varies in favour of the samples accepting more D^0 candidates, thus sample AB and ABC.

5.6 Performances

In the previous Section we have presented the set of cuts, both related to the particle identification and to the decay topology, used to extract the signal from the signal D^0 candidates from the background ones. Here we show as the results of this feasibility study, given in terms of signal-to-background ratio and statistical significance, can be directly interpreted in terms of statistical error to estimate the sensitivity of the ALICE detector for the measurement of the D^0 production cross sections and of the transverse momentum distributions in p-Pb collisions. This error is then compared to an estimate of the main sources of systematic uncertainties.

The relative statistical error, σ_S/s, on the number of reconstructed D^0 candidates, in a given p_t-bin and for a given number of events, is equal to the inverse $\sqrt{S+B}/S$ of the statistical significance. The signal S is obtained as S = T-B, where T is the total number (T=S + B) of candidates in an invariant mass window entirely containing the D^0 peak and B is the number of background candidates in the same window, estimated using, for example, a fit on the side-bands of the invariant mass distribution. The error on S is, therefore:

$$\sigma_S = \sqrt{\sigma_T^2 + \sigma_B^2} \approx \sigma_T = \sqrt{T} = \sqrt{S+B} \tag{5.1}$$

The error on B, σ_B, can be neglected; it is, in fact, much lower than the error on T , σ_T, since B is estimated on a larger invariant mass range and, thus, with better precision. From Eq. 5.1 we derive trivially $\sigma_S/S = 1/\mathcal{S}$, where $\mathcal{S}$ is the significance.

The final estimation of the number of signal D^0 candidates extracted from the background is the result of applying correction factors to account for efficiency and acceptance windows; each of this corrections contributes with a systematic error, whose estimates are summarized in Figure 5.12 and compared with the statistical error as a function of the transverse momentum of the D^0 meson. Errors due to the Monte Carlo simulation of tracking and PID efficiency and acceptance have been estimated as a 10% $p_t^{D^0}$-independent contribution; this estimate is a conservative one and the experience from other experiments rises the expectation that this error will lower as data will be gathered. The use of the combined particle identification is also expected to lower the estimate of this source of error.

As an application of the results obtained for the sensitivity of ALICE to the p_t-differential D^0 production cross section, we show the predicted effect of different shadowing models on the nuclear modification of the gluon PDF (Figure 5.13) on the nuclear modification factor R_{pA} (Figure 5.14). The comparison with the errors represented as a green band gives an estimation

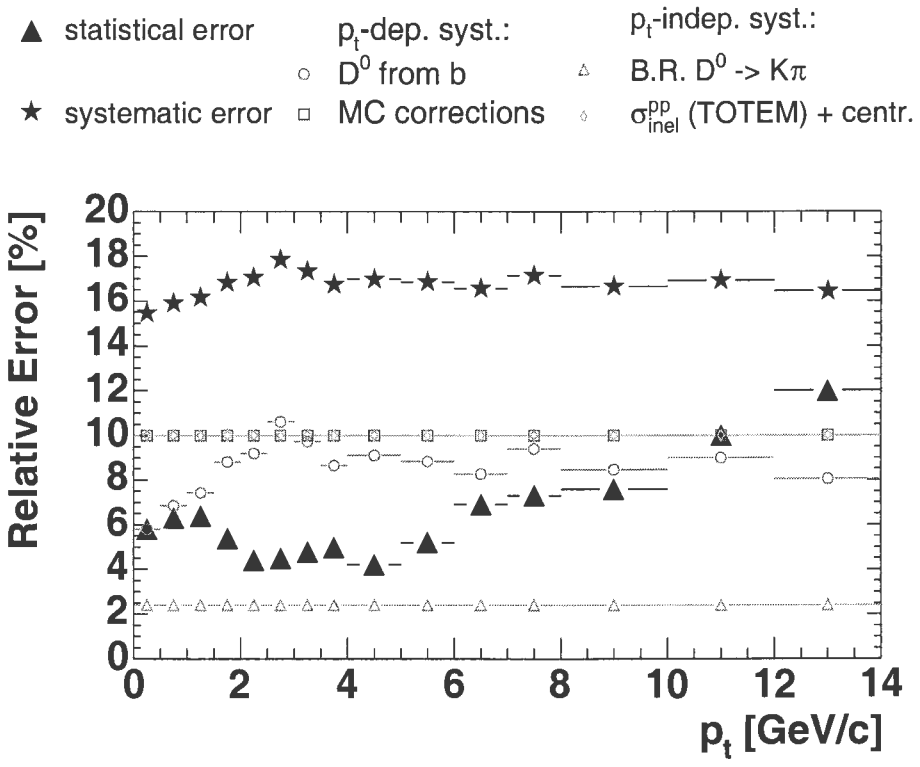

Figure 5.12: Statistical error compared with all the sources of systematic error for the p_t-differential D^0 production cross section in the range 0-14 GeV/c.

of the ALICE sensitivity to these possible shadowing scenarios.

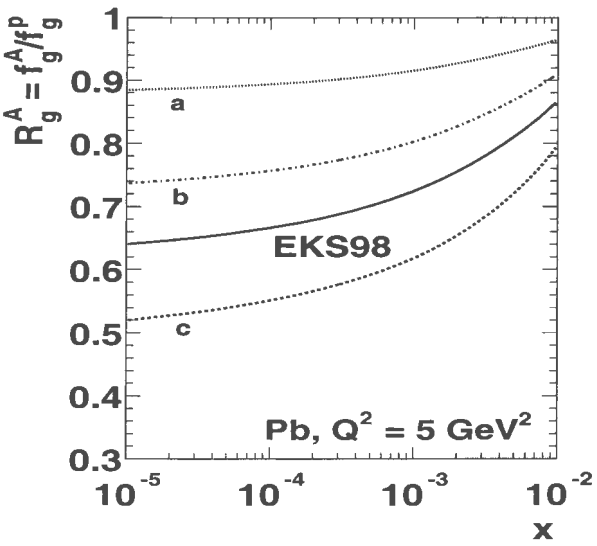

Figure 5.13: Comparison of the shadowing effect as predicted by different models.

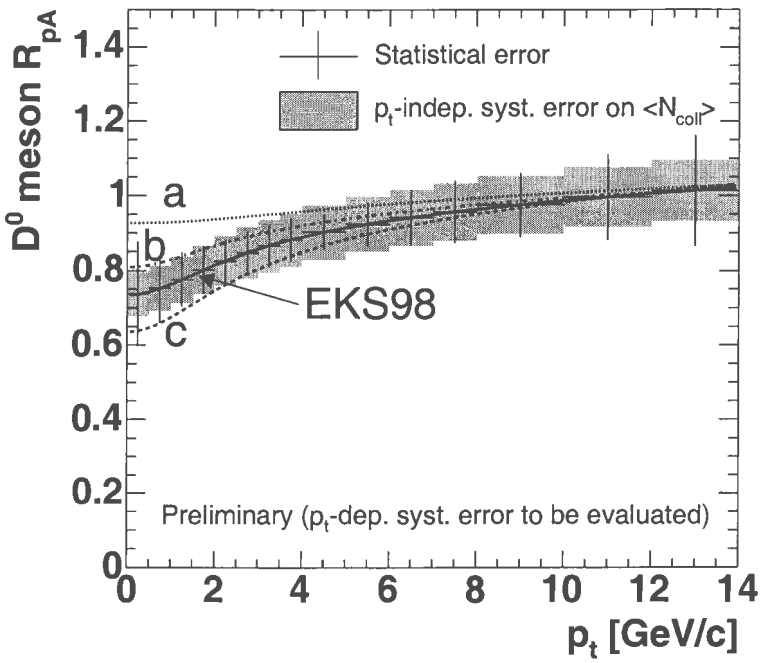

Figure 5.14: Nuclear modification factor R_{pPb} with rough estimate of systematic errors (green) independent of p_t. The p_t-dependent statistical errors are expected to vary similarly in the pp and p-Pb collision systems and thus to approximately cancel out.

Conclusions

Heavy quarks (charm and beauty) will be a key observable at LHC energies, in particular for ALICE which will detect them in different collision systems to use them as a probe of the deconfined medium in central nucleus-nucleus collisions.

This work was based on the simulation and exclusive reconstruction of the D^0 hadronic decay $D^0 \rightarrow K^-\pi^+$ in proton-lead collisions at $\sqrt{s}$=8.8 TeV at ALICE through an invariant mass analysis of the topology of the $K^-\pi^+$ decay pair produced at displaced secondary vertexes. The aim was to obtain an estimate of the sensitivity of the ALICE detector and simulation framework to open charm production in proton-lead collisions, fully exploiting the excellent tracking and vertexing capabilities of the ALICE vertex detector.

The achieved results, obtained as a function of the D^0 transverse momentum, are needed as a comparison to the analogue results in p-p and Pb-Pb collision systems and are also the basis for an estimate of the possibility to detect double-parton collisions at ALICE, which is favoured in the collision system studied in the present work. The p_t-differential D^0 production cross section can be measured in the range 0-14 GeV/c with statistical uncertainty better than 10% and systematic uncertainty better than 15-20%.

Where the AliRoot reconstruction tools were to be tuned, the p-Pb collision system showed to be much closer to the p-p one, due to the similar low charged particle multiplicity, compared to the ALICE central barrel detector granularity.

Innovative software and hardware solutions for a dedicated farm of PCs have also been tested, in view of the intensive computational requests which will arise at the start of the online ALICE activity:

- the channel bonding technique has proved to be a cheap solution to enhance the internal bandwidth, an especially important parameter to optimize the farm performances when distributed jobs are to be run on the farm.

- tests on the mosix and OpenMosix workload managers, while verify-

ing their effectiveness for the management of multiple jobs in a farm environment, have shown its failure to migrate AliRoot jobs.

Future activities which could exploit this work or aim it at further conclusions could be in particular:

- to update it in order to include the new software tools developped in the AliRoot framework, such as the combined PID and the new AliRoot IO, which would let this study approach the analysis tools which will be applied to real data;
- to estimate the capability of ALICE to measure double-parton collision cross section via the coupling of the D^0 in $K\pi$ decay channel with the trigger selection of the B meson semi-leptonic decay. This would most likely improve considerably the ALICE sensitivity to double parton collisions and would allow a promising future study in order to take advantage of the unprecedented multiparton cross section predicted for p-Pb collisions at LHC energies.

Appendix A

Useful variables in heavy-ion physics

In this appendix we want to recall the definition of the most important heavy-ion variables appeared in the text and briefly explain their importance in the context in which they usually appear. For an in-depth treatment of heavy-ion variables and their properties see e.g. [10] and [72].

The frame in which this variables are used are heavy-ion collisions; at high energyies the degrees of freedom involved in the collision lose in it only a small fraction of their longitudinal momentum. In this collisions one needs to take advantage of kinematical variables which transform simply under boosts along the beam axis. We call it longitudinal direction and label it as z-axis; we call *transverse plane* the plane transverse to it, i.e. the xy-plane.

A.1 Feynman's and Bjorken's x

Given a particle of four-momentum $p = (p_0, p_x, p_y, p_z) = (p_0, \vec{p}_T, p_z)$, two combinations of its components transform simply under longitudinal boosts: the forward and backward light-cone momentum variables, p^+ and p^-, are given by:

$$p^+ = p_0 + p_z \qquad \text{and} \qquad p^- = p_0 - p_z$$

The four d.o.f. of the four-momentum can thus also be given by (p^+, p_T, p^-). When the particle is on the mass-shell, we can write $p^2 = p^\mu p_\mu = E^2 - p^2 = m^2$, with m the rest mass of the particle, and therefore:

$$p^+ p^- = E^2 - p_z^2 = m^2 + p_T^2 \equiv m_T^2$$

The forward (backward) light-cone momentum variable is large (small) for a ultrarelativistic particle moving towards increasing z and viceversa. Under

a boost of velocity β along positive z, the forward light-cone momentum transforms according to:

$$p^{+'} = \gamma(1-\beta)p^{+}$$

where $\gamma = 1/\sqrt{1-\beta^2}$.

Often a particle, say c, can be considered a daughter of onother perticle, say a, e.g. after a collision. In this cases it is useful to introduce the *light-cone variable*[1]:

$$x^{+} = \frac{c^{+}}{a^{+}}$$

x^{+} (and the similarly defined x^{-}) are also called *positive (negative) light-cone momentum fraction* and is invariant under longitudinal boosts. In fact it can be seen as the boost-invariant generalization of the *Feynman's x*, i.e. the fraction of the longitudinal momentum of c, c_z^*, to its maximum momentum, c_{zmax}^*, since $x_F \to x^{\pm}$ for high center of mass energies $\sqrt{s}$. When c is one doughter of $a = c + X$, c is not a free particle since it still interacts with X and thus is off the shell. Still its light-cone momentum fraction, x^{+} or x^{-}, is useful and is called *Bjorken's x*: x_{Bj}.

A.2 Rapidity

The rapidity variable y is commonly used to describe the kinematics of a particle in HI collisions. For a particle of four-momentum $p^{\mu} = (E, \boldsymbol{p}) = (E, p_x, p_y, p_z)$ it is defined as:

$$y = \frac{1}{2}\ln\frac{E+p_z}{E-p_z}$$

or, equivalently, since $E = \gamma m$ and $p = \gamma\beta m$:

$$y = \frac{1}{2}\ln\frac{1+\beta}{1-\beta} = \tanh^{-1}\beta$$

The rapidity region around the rapidity of the center-of-mass in the laboratory frame (*mid-rapidity*) is called *central rapidity region.* The importance of the rapidity variable is that it can be seen as a generalization of the velocity in units of the light-speed c, β, because of two properties:

- β is the non-relativistic limit of the rapidity;

[1]For simplicity of notation we use the same letters indicating the particles, c and a, for their four-momenta, c and a, and their light-cone momenta, c^{+} and a^{+}

- composition of rapidities is like composition of velocities in the non-relativistic limit, i.e. under a Lorentz transformation along z with a velocity β we get: $y \to y' = y - y(\beta)$. Therefore rapidity distributions are invariant for boosts along z (e.g. $dN/dy' = dN/dy$).

The most useful relations are

- $$p_0 = m_T \cosh y \qquad \text{and} \qquad p_z = m_T \sinh y \tag{A.1}$$

- given a projectile particle a with mass m_a and longitudinal momentum a_z and a target particle b with mass m_b and longitudinal momentum b_z, their rapidities are:

$$\begin{cases} y_a &= sinh^{-1} \frac{a_z}{m_a} \\ y_b &= sinh^{-1} \frac{b_z}{m_b} \end{cases}$$

in the laboratory frame and, if $m_a = m_b$:

$$\begin{cases} y_a^* &= \frac{y_a - y_b}{2} \\ y_b^* &= \frac{y_b - y_a}{2} \end{cases}$$

in the center-of-mass frame of reference;

- in the limit $|\boldsymbol{p}| \simeq p_0$ it is equal to the pseudorapidity variable $\eta = -\ln \tan \theta/2$, thus it is directly related to the polar angle θ between the trajectory and the beam axis.

Eq.A.1 leads also to an important relation between rapidity and the two-dimensional space-time coordinates of a particle, indeed: Eq.A.1 $\Rightarrow z/t = v_z = p_z/p_0 = \tanh y$. Since the proper time is defined by $\tau = \sqrt{t^2 - z^2}$, one can write:

$$z = \tau \sinh y \qquad \text{and} \qquad t = \tau \cosh y$$

Thus, at a fixed proper time, e.g. the formation time τ_0, small rapidities are associated to small values of z.

A.3 Transverse momentum and transverse mass

The transverse momentum p_T is defined by $p_T = \sqrt{p_x^2 + p_y^2}$.
The transverse mass m_T is defined by $m_T = \sqrt{m^2 + p_T^2}$.

A particle produced in the collision obeys the *mass-shell condition*

$$p^2 = p^\mu p_\mu = E^2 - \vec{p}^2 = m^2 \tag{A.2}$$

if it is free; in this case it is said to be *on the mass shell* and then $m_T^2 = E^2 - p_z^2$. If the particle is not free, it will not obey the mass shell condition (A.2) and it is said to be *off the shell.*
Transverse momentum and transverse mass are not only useful for easily expressing the relations between momentum components and rapidity, as seen in the previous section, but they also enter in the expression A.3 for the invariant cross-section $E\frac{d^3\sigma}{d^3p}$ which allows to pinpoint a common behaviour for different types of particles (*m_T-scaling*, see next section).

Both variables are Lorentz-invariant under a boost along the longitudinal direction; in the ultrarelativistic limit, since $m_t \to p_T$ and $y \to \eta$, the relations (A.1) become:

$$p_0 = p_T \cosh\eta \text{ and } p_z = p_T \sinh\eta$$

A.4 Invariant cross-sections

The differential cross-section for particle production $\frac{d^3\sigma}{dp_x dp_y dp_z}$ is not Lorentz invariant under a boost along the z-direction as dp_z is not. From A.1 one gets $dp_z/E = dy$, which implies that dp_z/E is Lorentz invariant and leads us to turn to the following invariant differential cross-section:

$$E\frac{d^3\sigma}{dp^3} = \frac{d^3\sigma}{dp_x dp_y dy} = \frac{d^3\sigma}{p_t dp_t d\phi dy}$$

where the last equality derives from the variable substitution: $(p_x, p_y) \to (p_t = \sqrt{p_x^2 + p_y^2}, \phi = \tanh^{-1}(p_y/p_x))$. When the distribution does not depend on the polar angle ϕ it is usual to integrate over it and to use the following expression for the differrential cross-section for particle production:

$$\frac{1}{2\pi p_t}\frac{d^2\sigma}{dp_t dy} = \frac{1}{\pi}\frac{d^2\sigma}{d(p_t^2)dy} = \frac{1}{\pi}\frac{d^2\sigma}{d(m_T^2)dy} = \frac{1}{2\pi m_T}\frac{d^2\sigma}{dm_T dy}$$

A.5 Transverse distributions

The *transverse momentum distribution* $\frac{dN}{d^2p_T} = \frac{dN}{2\pi p_T d_{p_T}}$ is found experimentally to have a roughly exponential shape up to about 1 GeV and to decrease as an inverse power above a few GeV; the first region is called *soft region* and the second *hard region* (and *soft* and *hard particles* are called the particles falling in the two regions respectively).
Hard particles production is explained by QCD as the result of parton-parton

scattering and successive hadronization of the partons. An important experimental finding is that the transverse particle spectrum is approximately indipendent of the particle species, for kaons, pions and protons in particular, when plotted as a function of the transverse mass. Indeed the expression:

$$E\frac{dN}{dp_z d^2p_T} = \frac{dN}{dy d^2p_T} \approx A\frac{e^{-m_T/T}}{(m_T)^\lambda} \tag{A.3}$$

fits the experimental points whit approximately the same value for the *inverse slope* T. The general validity of eq. A.3 at almost fixed T is called m_T*-scaling.*

Bibliography

[1] O. Benhar, Is the equation of state of strongly interacting matter observable?, in *Quark-Gluon Plasma and Heavy Ion Collisions*, edited by M.-P. L. W. M. Alberico, M. Nardi, 2002.

[2] R. Hagedorn, Nuovo Cimento **35**, 395 (1965).

[3] N. Cabibbo and G. Parisi, Phys. Lett. **B59**, 67 (1975).

[4] A. Chodos, R. L. Jaffe, K. Jhonson, C. B. Thorn and V. F. Weisskopf, Phys. Rev. **D9**, 3471 (1974).

[5] F. Csikor *et al.*, Prog. Theor. Phys. Suppl. **153**, 93 (2004), [hep-lat/0401022].

[6] Z. Fodor and S. D. Katz, JHEP **04**, 050 (2004), [hep-lat/0402006].

[7] U. Heinz, hep-ph/0109006.

[8] J. D. Bjorken, Phys. Rev. **D27**, 140 (1983).

[9] U. W. Heinz, Nucl. Phys. **A685**, 414 (2001), [hep-ph/0009170].

[10] C.-Y. Wong, *Introduction to High-Energy Heeavy-Ion Collisions* (World Scientific, 1994).

[11] BRAHMS Collaboration, M. Gyulassy, Phys. Rev. Lett. **91** (2004), [nucl-th/0403032].

[12] J. Rafelski and B. M. et al., Phys. Rev. Lett. **48**, 1066 (1982).

[13] NA57 Collaboration, K. Fanebust *et al.*, J. Phys. **G28**, 1607 (2002).

[14] NA50 Collaboration, P. Cortese *et al.*, Nucl. Phys. **A715**, 679 (2003).

[15] T. Matsui and H. Satz, Phys. Lett. **B178**, 416 (1986).

[16] M. Gyulassy and M. Plumer, Nucl. Phys. **A527**, 641 (1991).

[17] M. Gyulassy, M. Plumer, M. Thoma and X. N. Wang, Nucl. Phys. **A538**, 37c (1992).

[18] X.-N. Wang and M. Gyulassy, Phys. Rev. Lett. **68**, 1480 (1992).

[19] J. D. Bjorken, FERMILAB-PUB-82-59-THY.

[20] M. Gyulassy and X.-n. Wang, Nucl. Phys. **B420**, 583 (1994), [nucl-th/9306003].

[21] A.Accardi, hep-ph/0212148.

[22] BRAHMS Collaboration, I. Arsene *et al.*, Phys. Rev. Lett. **91**, 072305 (2003), [nucl-ex/0307003].

[23] STAR Collaboration, J. Adams *et al.*, Phys. Rev. Lett. **91**, 072304 (2003), [nucl-ex/0306024].

[24] Y. Schutz, Phases of nuclear matter, in *NuPECC Long Range Plan 2004*, 2004, Chapter 5.

[25] N. S. Amelin, N. Armesto, C. Pajares and D. Sousa, Eur. Phys. J. **C22**, 149 (2001), [hep-ph/0103060].

[26] K. J. Eskola, P. V. Ruuskanen, S. S. Rasanen and K. Tuominen, Nucl. Phys. **A696**, 715 (2001), [hep-ph/0104010].

[27] ALICE Collaboration, F. Carminati *et al.*, J. Phys. G: Nucl. Part. Phys. **30**, 1517 (2004).

[28] CERN Yellow Report 2000-004: Heavy flavour physics, hep-ph/0311048.

[29] M. L. Mangano, P. Nason and G. Ridolfi, Nucl. Phys. **B373**, 295 (1992).

[30] A. D. Martin, R. G. Roberts, W. J. Stirling and R. S. Thorne, Eur. Phys. J. **C4**, 463 (1998), [hep-ph/9803445].

[31] CTEQ, H. L. Lai *et al.*, Eur. Phys. J. **C12**, 375 (2000), [hep-ph/9903282].

[32] A. Dainese, *Charm production and in-medium energy loss in nucleus-nucleus collisions with ALICE. A performance study.*, PhD thesis, Università degli studi di Padova, 2003.

[33] A. Morsch and I. Pshenichnov, ALICE internal note, ALICE-INT-2002-034.

[34] K. J. Eskola, V. J. Kolhinen and C. A. Salgado, Eur. Phys. J. **C9**, 61 (1999), [hep-ph/9807297].

[35] A. Accardi *et al.*, hep-ph/0308248.

[36] N. Paver and D. Treleani, Nuovo Cim. **A70**, 215 (1982).

[37] A. D. Fabbro, *Double parton scatterings in high energy hadronic interactions*, PhD thesis, Università degli studi di Trieste, 2003.

[38] M. Strikman and D. Treleani, Phys. Rev. Lett. **88**, 031801 (2002), [hep-ph/0111468].

[39] CDF, F. Abe *et al.*, Phys. Rev. Lett. **79**, 584 (1997).

[40] CDF, F. Abe *et al.*, Phys. Rev. **D56**, 3811 (1997).

[41] G. Calucci and D. Treleani, Phys. Rev. **D57**, 503 (1998), [hep-ph/9707389].

[42] G. Calucci and D. Treleani, Phys. Rev. **D60**, 054023 (1999), [hep-ph/9902479].

[43] E. Cattaruzza, A. Del Fabbro and D. Treleani, Phys. Rev. **D70**, 034022 (2004), [hep-ph/0404177].

[44] X.-N. Wang and M. Gyulassy, Phys. Rev. **D44**, 3501 (1991), The code can be found at `http://www-nsdth.lbl.gov/~xnwang/hijing/`.

[45] E. Norrbin and T. Sjostrand, Eur. Phys. J. **C17**, 137 (2000), [hep-ph/0005110].

[46] R. Brun, F. Bruyant, M. Maire, A. C. McPherson and P. Zanarini, Geant user's guide, 1986, `http://wwwasdoc.web.cern.ch/wwwasdoc/geantold/GEANTMAIN.html`.

[47] A. Dainese and N. Carrer, ALICE internal note, ALICE-INT-2003-011.

[48] A. Badalà *et al.*, ALICE internal note, ALICE-INT-2001-011.

[49] `http://lcg.web.cern.ch/LCG/`.

[50] La farm di Alice Trieste, website, `http://www.ts.infn.it/experiments/alice/aliroot/farm`.

[51] http://alien.cern.ch.

[52] The Beowulf Project, http://www.beowulf.org.

[53] E. Fragiacomo, R. Grosso, S. Piano and R. Rui, ALICE internal note, ALICE-INT-2003-026; the note can be found at http://www.ts.infn.it/experiments/alice/aliroot/publications/welcome.h%tml.

[54] http://root.cern.ch.

[55] http://aliweb.cern.ch/offline/.

[56] The Beowulf Howto, http://www.beowulf.org/software/bonding.html.

[57] The Linux NFS Howto, available e.g. from http://www.tldp.org/docs.html\#howto.

[58] Mosix, http://www.mosix.org/.

[59] The Parallel Virtual File System Project, http://parlweb.parl.clemson.edu/pvfs/index.html.

[60] Portable Batch System, http://www.openpbs.org/.

[61] http://www.netfilter.org/.

[62] Gentoo, http://www.gentoo.org/.

[63] Netpipe (Network Protocol Independent Performance Evaluator), http://www.scl.ameslab.gov/netpipe/.

[64] http://www.cs.inf.ethz.ch/CoPs/ECT/.

[65] OpenMosix, http://openmosix.sourceforge.net.

[66] Particle Data Group, S. Eidelman *et al.*, Phys. Lett. **B592**, 1 (2004).

[67] H.-U. Bengtsson and T. Sjostrand, Comput. Phys. Commun. **46**, 43 (1987).

[68] T. Sjostrand, Comput. Phys. Commun. **82**, 74 (1994).

[69] CERN Yellow Report 2000-004, http://preprints.cern.ch/cgi-bin/setlink?base=cernrep&categ=Yellow_Report&id=2000-004.

[70] A. Dainese and M. Masera, ALICE internal note, ALICE-INT-2003-027.

[71] V. Karimäki, CMS Note 1997/051.

[72] F.Antinori, A.Billmaier and J.Zaranek, Introduction to Ultrarelativistic Heavy-Ion Physics at the CERN-SPS.

rgrosso

thnocoloured.ps

Printed: Fri Feb 25 17:10:28 CET 2005

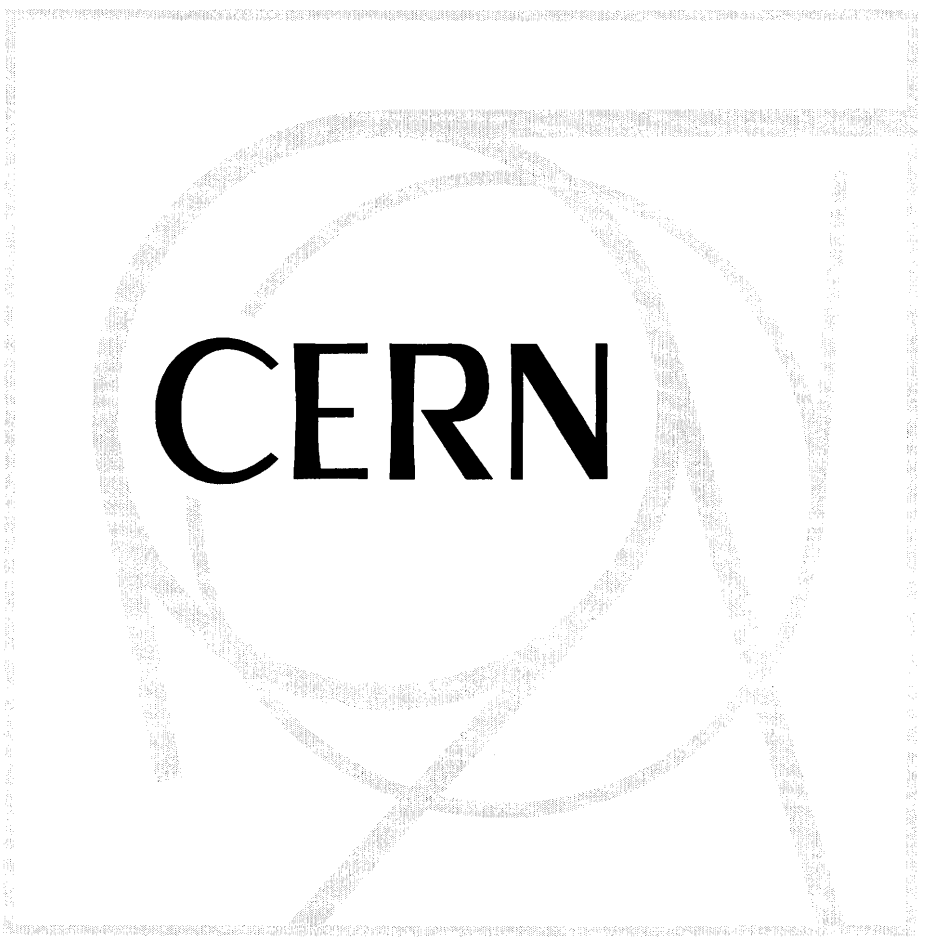

Printed on: 13-2-cor
Userid: rgrosso
Node: pcepaip16.cern.ch

Contents